Lawrence Berkeley National Laboratory
Recent Work

Title

SPINODAL DECOMPOSITION AND COARSENING IN Cu-Ni-Fe ALLOYS

Permalink

https://escholarship.org/uc/item/8v4999t2

Author

Livak, Ronald John.

Publication Date

1972-09-01

SPINODAL DECOMPOSITION AND COARSENING IN
Cu-Ni-Fe ALLOYS

Ronald John Livak
(Ph. D. thesis)

September 1972

DISCLAIMER

SPINODAL DECOMPOSITION AND COARSENING
IN Cu-Ni-Fe ALLOYS

Contents

SPINODAL DECOMPOSITION AND COARSENING
IN Cu-Ni-Fe ALLOYS

Ronald John Livak

Inorganic Materials Research Division, Lawrence Berkeley Laboratory and
Department of Materials Science and Engineering, College of Engineering;
University of California, Berkeley, California

ABSTRACT

Coarsening of the spinodal microstructure in copper-nickel-iron alloys has been studied in detail using transmission electron microscopy. A dislocation multiplication process is proposed to explain the observations on loss of coherency of the platelets. Mechanical testing of aged specimens indicated that the interfacial dislocations contribute to the strengthening and that large coherent platelets enhance the initial work hardening rate. The intergranular fracture of these decomposed alloys seems to result from microstructural differences between the grain boundary regions and the matrix.

Loss of coherency in this lamellar microstructure occurs by the capture of slip dislocations at the interphase interfaces. It is proposed that the subsequent formation of misfit-accommodating dislocation loops proceeds by the spiraling of these captured dislocations around the platelets similar to the formation of helical dislocations. Because the Burgers vector of the captured dislocation is inclined at $45°$ to the $\{100\}$ interface, rotation of the initial $\{100\}$ coherent interface toward the $\{110\}$ plane containing $\bar{b}$ occurs in order to lower the interfacial energy.

Strengthening of the semi-coherent microstructure arises from the interfacial dislocations and the difference in shear moduli between the two phases, whereas prior to the loss of coherency, the flow stress is

determined by the differences in lattice parameters and shear moduli
across the coherent interfaces. The observations suggest that the
capture of slip dislocations at large coherent platelets increases the
initial work hardening rate. Transmission electron microscopy has shown
that the coherent particles are sheared during deformation.

Preferential grain boundary precipitation in these decomposed Cu-Ni-Fe
alloys seems to be responsible for the observed intergranular failure.
Because the grain boundary regions are softer than the matrix, plastic
constraint in such regions produces a triaxial stress state that leads
to premature failure along the grain boundaries. After long aging times
at high temperatures, the fracture mode becomes transgranular as the
matrix coarsens and the mechanical behavior of the matrix and the grain
boundary regions becomes similar.

I. INTRODUCTION

A. Theory of Spinodal Decomposition

The concept of the spinodal was formulated at the same time as nucleation theory, and both concepts were discussed in the same paper by Willard Gibbs[1] in 1877. The thermodynamic criterion for the spinodal is that the second derivative of the free energy with respect to composition is zero ($d^2f/dc^2 = 0$). Inside the spinodal where $d^2f/dc^2 < 0$ no activation barrier for nucleation exists as in a metastable solid solution, and consequently the unstable solid solution spontaneously decomposes. Thus, Gibbs referred to the spinodal as the limit of metastability. Spinodal decomposition is characterized by small composition fluctuations over large distances, whereas, a classical nucleation process is characterized by large composition variations over small distances. Because the new phases form by a continuous diffusional process with a gradual change in composition across the interface, they must have similar crystal structures as the original solid solution and are coherent. The resulting microstructure consists of a uniform dispersion of small, coherent particles. Experimental observations have shown that spinodal decomposition occurs in metallic, ceramic and glass systems. Several recent review articles[2-4] have described the theoretical and experimental studies pertaining to spinodal decomposition.

A diffusion theory to describe spinodal decomposition was first proposed by Hillert[5] in which he considered the effect of a one dimensional composition fluctuation on the thermodynamic driving force for chemical diffusion and numerically calculated, using a nearest neighbor

model, the changes in solution free energy as the composition evolved.
By treating the crystal as a continuum and making certain simplifying
assumptions, Cahn[6,7] developed an analytical expression for the
phenomenological diffusion equation that describes spinodal decomposition.
The solution to the derived diffusion equation can be mathematically
expressed as the superposition of periodic composition waves in the
solid solution with an exponential time dependence. Included in the
diffusion equation are terms for the coherency strain energy and the
concentration gradient energy. The microstructure predicted by Cahn's
theory is a periodic distribution of small, coherent particles or regions
of the two phases throughout the entire volume of the anisotropic crystal.

Some of the assumptions and mathematical procedures used by Cahn
and Hilliard[8,9] to derive the diffusion equation for an inhomogeneous
solid solution were questioned in recent articles by Hirth, Tiller and
Pound[10] and Tiller, Pound and Hirth.[11] However, in a subsequent paper
by Morris[12] the validity of the diffusion equation derived by Cahn
and Hilliard was substantiated. Also, Cahn and Hilliard[13] have written
a rebuttal to the criticisms raised by Hirth, et al.

By combining the approaches taken by Hillert and Cahn, Cook,
deFontaine and Hilliard[14] developed a discrete lattice model for dif-
fusion that describes both continuous ordering transformations and
spinodal decomposition. However, little advantage is to be realized
in using the discrete lattice model for spinodal decomposition because
in most cases the composition fluctuation receiving maximum applification
should usually be large enough for the continuum approximation to be
valid. A further development of this theory by Cook and deFontaine[15,16]

has taken into account the effect of elastic free energy of solid
solutions.

In the initial papers by Cahn on spinodal decomposition, only the
linear, or first order, terms in the diffusion equation were considered
in order to give an analytical expression that could easily be treated
in closed form. However, this linearized diffusion equation is only
valid for the early stages of spinodal decomposition when the ammplitudes
of the composition fluctuations are small and the nonlinear terms in the
diffusion equation are not important. In a subsequent paper on the
later stages of spinodal decomposition and the beginnings of particle
coarsening, Cahn[17] considered the effects of these nonlinear terms on
the phase separation by using a series approximation to represent the
composition dependence of the diffusion coefficient and by then solving
the resulting nonlinear equation by successive approximations. From
this analysis, it was shown that harmonic distortions are produced
that interact with the initial symmetrical composition waves in such
a way to approach the equilibrium structure. In alloys of asymmetrical
compositions, the even harmonics distort the initial composition waves
to give a minor phase far from the average composition and a major
matrix phase consistent with the lever rule. The odd harmonics convert
the fundamental sine wave into a square wave, i.e. a composition profile
more characteristic of a two phase structure, by flattening the peaks
of the fundamental and sharpening the gradient between the extremes
in composition.

Cahn[17] treated the beginnings of particle coarsening by considering
a range of wavelengths present in the solid. His analysis predicts a

gradual broadening of the fundamental spectrum with longer aging time. For alloys of asymmetrical compositions, regions of lesser and greater amplification will alternate as a result of a narrow range of wavelengths that beat against each other. When the nonlinear terms become significant in altering the composition waves to satisfy the lever rule, the phase that will eventually become the minor phase is more developed in the regions of greater amplification. These minor phase particles remain larger and the lever rule requirement that there be less of the minor phase is carried out predominantly at the expense of the minor phase in the less developed regions. Thus, large wavelengths which are multiples, or harmonics, of the initial wavelength develop.

B. Literature Review of Experimental Studies

One difficulty in studying the spinodal reaction in solids is a working definition of spinodal decomposition that is amenable to experimental verification. The thermodynamic criterion given by Gibbs and then modified for solids by Cahn is an exact criterion for spinodal decomposition. However, it is very difficult to verify experimentally when this thermodynamic criterion is satisfied. In addition, other decomposition processes can occur that will supersede or obliterate the spinodal reaction. From an experimental viewpoint, the defining characteristics of spinodal decomposition are a gradual change in composition between the two decomposing regions (i.e. change in amplitude of the composition wave) and a diffuse interface between the two regions.

The most sensitive technique for following the change in amplitude of the composition waves in alloys containing iron seems to be Mössbauer

spectroscopy; and the decomposition of Cu-Ni-Fe alloys[18,19] and Fe-Cu alloys[20,21] has been studied using this technique. Small angle x-ray scattering has proved to be very useful in experimentally verifying Cahn's model for spinodal decomposition.[22] Furthermore, small angle scattering can be used to observe the change in the concentration gradient at the interface using a form of Porod's equation for the scattering intensity.[23] Less sensitive techniques for following the change in amplitude of the composition waves are measurements of electrical or magnetic properties that depend on the compositions of the decomposing regions. Transmission electron microscopy has been very useful in characterizing the micro-structure of spinodal alloys,[24,25] but it is necessary to use special techniques, such as a velocity analyzer, to follow quantitatively the change in amplitude of the composition waves. The most direct method of studying the spinodal structure is to use field ion microscopy (e.g. Au-Pt alloys can be studied using FIM).[26]

In elastically anisotropic materials, spinodal decomposition occurs along the elastically "soft" directions which are the cube directions in Cu-Ni-Fe alloys. The resulting periodic structure pro-duces sidebands in diffraction patterns, and this effect has been studied extensively by investigators using x-ray diffraction. The first observation of such sidebands was reported by Bradley[27] for a Cu-Ni-Fe alloy that had been quenched and then aged inside the mis-cibility gap. Daniel and Lipson[28,29] made further observations on the same alloy; and using a model based on a periodic, modulated structure, they derived a formula relating the sideband spacing to the structural periodicity which has been confirmed by transmission

electron microscopy.[24,25] The physical origin of these sidebands in some Cu-Ni-Fe alloys was considered in further detail in a subsequent article by Hargreaves.[30] Another model consisting of a complex array of GP zones surrounded by regions of depleted matrix has been proposed by Guinier to explain the formation of the sidebands.[31] More recently deFontaine has developed a general theory of diffraction from one-dimensional modulated structures.[32]

In a recent article, Cook[33] described the effect of thermal fluctuations due to Brownian motion on spinodal decomposition and concluded that, in an operational sense, the spinodal is a diffuse boundary during the initial stages of the decompositional process. That is, there is no distinct difference in transformation kinetics inside and outside the spinodal region during the early stages. In his review article on spinodal decomposition, Cahn[2] noted that for dilute solid solutions the composition profile predicted by his theory is similar to the model for GP zones that Guinier proposed to explain the sideband phenomenon.[31] These theoretical considerations indicate that, from a mechanistic viewpoint, no clear cut distinction can be made between spinodal decomposition and homogeneous nucleation of clusters or GP zones but rather that a gradual and continuous change in the mechanism of phase separation occurs as the alloy composition varies from the center of the miscibility gap towards the solvus curve. The experimental observations of Phillips[34] and Dorfeld and Phillips[35] using transmission electron microscopy and x-ray diffraction methods to study the decomposition of a Cu-Ni-Co alloy containing 10% volume fraction of the magnetic phase support such an interpretation for the mechanism of

phase separation. Dorfeld and Phillips concluded that the Cu-Ni-Co alloy studied decomposed by classical nucleation and growth. However, as discussed by Butler and Thomas,[24] an alloy will contain ~20% volume fraction or more of the minor phase if its composition lies inside the chemical spinodal. Therefore, the Cu-Ni-Co alloy studied by Dorfeld and Phillips was probably outside the spinodal and would be expected to decompose by homogeneous nucleation of Ni-Co rich clusters.

Spinodal decomposition during continuous cooling is of technological interest since continuous cooling will afford a convenient method of developing spinodal structures in commercial heat treating practice. Huston, Cahn and Hilliard[36] have extended Cahn's theory to the case of continuous cooling by treating certain of the coefficients in the linearized diffusion equation as time dependent because of their strong temperature dependence. Decomposition, at least during the initial stages, still proceeds by the growth of composition fluctuations. The only difference comes in describing the amplitude as a function of time.

Badia, Kirby and Mihalisin[37] have studied the strengthening during continuous cooling of Cu-Ni-Cr alloys containing 20 to 45% Ni with up to 4% Cr. Because of the small amount of Cr in the alloys studied, it is uncertain if any of the alloy compositions were inside the spinodal region for this ternary system. However, their experimental observations showed many points of similarity with the theoretical calculations of Huston, et al. for spinodal decomposition during continuous cooling. A commercial Cu -30% Ni -2.8% Cr alloy is now available from International Nickel which is hardened by decomposition during cooling. Complete

decomposition requires less than 10 seconds, and 1/16 inch sections

air cool slowly enough to get the full hardening effect. The reaction

cannot be fully suppressed even by liquid quenching thin sections, and

heavy sections are insensitive to the cooling medium.

In extending the theory of spinodal decomposition to ternary

systems, Morral and Cahn[38] demonstrated the possibility of both spinodal

decomposition and continuous ordering occurring in some ternary alloys

under certain conditions. Recent transmission electron microscopy

observations of Bouchard and Thomas[39] indicate that in some Cu-Mn-Al

alloys for certain aging conditions both phase separation and ordering

occur simultaneously. Russian investigators[40,41] have presented evidence

showing the decomposition of Fe-Be alloys into a periodic, modulated

structure containing Fe-Be particles with the ordered CsCl structure.

As an aid in selecting possible ternary systems that contain a

spinodal region, Gaye and Lupis[42] have discussed the restrictivity of

the thermodynamic conditions for spinodal decomposition in a multi-

component system. Also, Cahn[2] has outlined the procedure to follow

in developing a spinodal alloy. One would begin with a system in which

one has observed coherent precipitates of the same or related crystal

structures or has reason to suspect that they might occur. When such

precipitates do occur, one knows that it is possible in this system to

cross the coherent phase boundary and thus have enough chemical driving

force to overcome coherency strains. The spinodal is then usually

attainable through a small change in composition or a greater under-

cooling. By suitable additional alloying elements, the coherency strain

can be altered to affect the accessability of the spinodal.

Several alloy systems have been studied that show evidence of spinodal decomposition. Many decomposed alloys exhibit the sideband phenomenon,[31] but such an observation is not sufficient evidence to conclude that the alloy has decomposed spinodally. Although a periodic microstructure is characteristic of a spinodal alloy that is elastically anisotropic, such microstructures can also develop by selective growth due to elastic alignment as observed in Cu-Co[43] and Ni-Al[44,45] alloys.

The first spinodal system to be studied extensively was Cu-Ni-Fe in which the first observations of sidebands were made.[27-30] A later study by Hillert, Cohen and Averbach[46] using x-ray diffraction confirmed that Cu-Ni-Fe alloys in a certain range of compositions decompose by a spinodal mechanism, the kinetics of which had been studied by Hillert.[5] More recent studies using transmission electron microscopy[24,25] have provided direct metallographic evidence showing that the decomposition of these Cu-Ni-Fe alloys exhibits characteristics associated with the spinodal transformation.

Some other alloy systems for which there is evidence to suggest decomposition by a spinodal mechanism are Au-Pt, Al-Zn and Au-Ni. X-ray diffraction studies of Au-Pt alloys[47-49] indicate that decomposition occurs by a spinodal mechanism or possibly homogeneous nucleation; and more recent electrical resistivity studies[50,51] provide additional evidence to support this conclusion. In the Al-Zn system, it is difficult to interpret the experimental observations because of the different phase transformations that occur. The small angle x-ray scattering measurements of Rundman and Hilliard[22] provide convincing evidence for spinodal decomposition of an Al -22% Zn alloy aged at 65°C. However,

a transmission electron microscopy study of a series of concentrated Al-Zn alloys[52] showed that the modulated structure observed in these alloys is not necessarily associated with spinodal decomposition. And a subsequent study on the decomposition of a near-eutectoid Al -50% Zn alloy[53] showed that the observed modulated, isotropic structure results from a discontinuous reaction that nucleates at grain boundaries and free surfaces rather than from spinodal decomposition. Although modulated structures of small amplitudes are observed in Au-Ni alloys, the experimental evidence[54,55] indicates that the coherent spinodal is suppressed to such low temperatures where diffusion cannot readily occur that decomposition of the solid solution is prevented.

C. Structure and Mechanical Behavior of Cu-Ni-Fe Alloys

Within a certain range of compositions in the Cu-Ni-Fe system, a modulated structure developes upon aging inside the miscibility gap. Experimental evidence indicates that some Cu-Ni-Fe alloys with this modulated structure decompose by a spinodal mechanism.[24,25,46] The high temperature solid solution and the two low temperature phases all have face centered cubic crystal structures. Although the equilibrium structure is fcc, the two low temperature phases have a transitional face centered tetragonal structure during part of the decomposition process. The microstructure during the early stages of decomposition consists of wavy, irregular particles in a pseudo-periodic array lying along the cube planes as shown in Fig. 1a and 1b. Because the cube directions are the elastically "soft" directions in these alloys, the particles develop into coherent platelets with planar interfaces along the {100} planes (see Fig. 1c). After long aging times, the large

platelets lose coherency by the development of interfacial dislocations.[24]

The pseudo-binary phase diagram for the alloys studied is given in Fig. 2 This phase diagram lies along a tie-line on the miscibility gap of the Cu-Ni-Fe system and is derived from the earlier work of Köster and Dannöhl.[56] Bradley, Cox and Goldschmidt[57] have also studied the equilibrium phase diagram for this alloy system. The Curie temperatures are for as quenched alloys of the indicated compositions and are also taken from the work of Köster and Dannöhl. The position of the chemical spinodal was estimated by Butler[58] using the "root-three rule" derived by Cook and Hilliard.[59] Because the misfit between the coherent particles is small (<1%) in these alloys, the coherent spinodal is not significantly depressed below the chemical spinodal. A subsequent study by Butler[60] on the initial stages of decomposition in an alloy of composition A supports this conclusion. The alloy composition designated A in Fig. 2 will be referred to as the symmetrical alloy because it contains approximately equal volume fractions of the two low temperature phases, whereas the two compositions marked 1 and 2 will be referred to as asymmetrical alloys since they contain about 25% volume fraction of the minor phase. The compositions of the three alloys studied, in atomic per cent, are:

    alloy 1: 32.0 Cu - 45.5 Ni - 22.5 Fe

    alloy A: 51.5 Cu - 33.5 Ni - 15.0 Fe

    alloy 2: 64 Cu - 27 Ni - 9 Fe

As these Cu-Ni-Fe alloys decompose inside the spinodal, a two- to three-fold increase in the yield stress is observed. Butler and Thomas[24] studied the symmetrical alloy of composition A and found that

as the aging temperature increased the maximum yield stress decreased.
Butler[58] has considered in detail various strengthening mechanisms
proposed for coherent precipitates and has concluded that the internal
stresses in this decomposed alloy are probably the most important factor
contributing to the strengthening. In the research done for my master's
thesis,[25,61] it was found that for alloys of compositions 1 and 2 the
maximum yield stress is independent of the volume fractions of the two
phases. Furthermore, the yield stress varies with the difference in
composition of the two decomposing phases and is independent of the
wavelength or particle spacing. Dahlgren[62] has proposed a model based
on internal coherency stresses to explain the yield stress of alloys
containing modulated structures. The results of this model are in good
agreement with the experimental results for these Cu-Ni-Fe alloys. The
observations made on the yield strength of Au-Pt alloys[49] support the
conclusion that in spinodal alloys containing a larger volume fraction
of coherent particles the internal stresses are the primary strengthening
mechanism. However, from the available data one cannot exclude other
factors such as differences in shear moduli, Burgers vectors or stacking
fault energies between the two phases or a chemical (atomic) interaction
at the interface that may contribute to the strengthening.

In the research done for my master's thesis,[61] it was observed that
after short aging times these spinodally decomposed alloys fail inter-
granularly with a corresponding decrease in the total elongation of
the tensile specimen. This change in fracture mode from transgranular
to intergranular with aging was tentatively associated with grain
boundary precipitation or possibly solute segregation at the grain
boundaries.

As a continuation of this research on Cu-Ni-Fe alloys in the

spinodal region, this thesis describes various aspects of spinodal

decomposition and coarsening in these alloys and the resulting mechanical

behavior. In the following section, loss of coherency is considered

in detail and a mechanism is proposed for the formation of many inter-

facial dislocations from a single slip dislocation adsorbed at the

interface. The mechanical behavior of these semi-coherent particles

is described in the second section and the work hardening characteristics

of the interfacial dislocations are discussed. In the last section,

the intergranular fracture of these spinodally decomposed alloys is

considered and an explanation is given for this type of failure.

II. LOSS OF COHERENCY

A. <u>Introduction</u>

After long aging at high temperatures, the coherent platelets in these spinodally decomposed Cu-Ni-Fe alloys lose coherency as interfacial dislocations form and the particle morphology also changes. Transmission electron microscopy observations have led to a consistent explanation of how the semi-coherent microstructure evolves from the initially coherent platelet morphology. The relative energies of various types of interfacial structures are considered and a dislocation mechanism is proposed to explain the generation of many interfacial dislocations from a single slip dislocation adsorbed at the interface.

In the symmetrical alloy, Butler and Thomas[24] observed that interfacial dislocations initially form when the platelet thickness is ~500Å and that loss of coherency occurs more rapidly at higher aging temperatures even though the mismatch between the two phases decreases with increasing temperature. For example, interfacial dislocations were not observed in samples aged at 625°C even after 940 hrs ($\lambda \simeq 1080Å$), whereas in samples aged at 700°C interfacial dislocations were first observed in a few areas after 40 hrs ($\lambda \simeq 800-1350Å$) and only after 17 hrs in samples aged at 775°C ($\lambda \simeq 950Å$). Contrast experiments showed that the most probable Burgers vectors of the interfacial dislocations are of the type $a/2 \langle 110 \rangle$. After long aging times, networks of interfacial dislocations develop and the interfaces tend to rotate away from the {100} habit planes towards {110} planes. Possible mechanisms for loss of coherency in this Cu-Ni-Fe alloy were discussed by Butler and Thomas.

B. Experimental Procedure

1. Materials and Heat Treatment

The preparation of the experimental alloys was the same as used in the previous research work for my master's thesis[61] and also by Butler and Thomas.[24] The alloys were prepared using 99.999% purity Cu, 99.85% purity Ni and 99.6% purity Fe with 0.5% Mn added to each melt as a deoxidizer to aid fabrication. The charges were melted in a large induction furnace under a helium atmosphere and were chill cast into copper molds to reduce segregation. X-ray fluorescent analysis verified to within ±1% the compositions given previously. The ingots were inserted into stainless steel envelopes and placed inside an Inconel tube filled with cast iron chips and a small amount of activated charcoal to prevent oxidation. Following homogenization at 1050°C for three days, the ingots were hot forged and rolled at 950°C to a thickness of 40 mils. Small pieces from each ingot were then annealed and further cold rolled to 8 mils thickness for electron microscopy specimens.

Coupons of this 8 mils thick material were encapsulated in evacuated quartz tubes, solution treated at 1050°C for two hours and then quenched in ice water. Because the later stages of coarsening were to be studied, the quenching rate was not critical to the subsequent aging treatments. To obtain samples containing semi-coherent particles, the coupons were aged in evacuated quartz tubes at 775°C and 800°C for 50, 100 and 200 hrs.

2. Electron Microscopy

The heat treated coupons were hand ground on wet polishing paper to a thickness of 3-4 mils. In some cases, the coupons were chemically thinned to the same thickness using the following solution.

20 ml acetic acid

10 ml nitric acid

4 ml hydrochloric acid

A brass cutting tool was used to spark cut 2.3 mm diameter discs from the thinned material. These discs were then polished on fine emery paper to a thickness of 2-3 mils and electropolished in a double jet polisher using the following electrolyte.

75 gm CrO_3

400 ml acetic acid

12 ml H_2O

To dissolve all the CrO_3, this solution was heated during mixing. The temperature of the electrolyte was held at ~10°C during polishing using an ice water bath. To obtain a saucer shaped profile in the disc, a low current (~15 ma) was initially used and then the current was increased to ~30 ma during the final minutes of polishing to get a good foil. This polishing procedure worked fairly well even though the Cu rich phase polished preferentially.

The polished discs were examined in a Siemens Elmiskop IA electron microscope operated at 100 kV using a double tilt goniometer stage for contrast experiments. A few foils were examined in the Hitachi 650 kV microscope to study the interfacial dislocation arrays in thicker areas of the foils. In order to obtain a better understanding of the dislocation configurations, pairs of stereo micrographs were

taken of some areas by tilting the foil 10-12° along a Kikuchi band
so as to have the same diffraction conditions for both micrographs.

C. Experimental Observations

Most of the electron microscopy observations were made on alloy
2 which contains the largest volume fraction of the Cu rich phase in
the three alloys studied. Since the Cu rich phase polishes perferen-
tially, it was easier to prepare good foils of alloy 2 than of the other
two alloys. No interfacial dislocations were observed in specimens
of the two asymmetrical alloys aged at 700°C for 10, 40 and 200 hrs.
and at 775°C for 10 hrs. In the research for my master's thesis,[61]
specimens of these same alloys were aged at 625°C for times up to
1000 hrs and no interfacial dislocations were observed (see Figs. 1
and 3). When aged at 800°C alloy 2 contains ~15% volume fraction
of the Ni-Fe rich phase. This alloy remains single phase when aged
at 825°C but the symmetrical alloy is still inside the two phase
region at this aging temperature.

As the structure coarsens in these spinodal alloys, coherent
platelets form on the cube planes because this morphology minimizes
the elastic strain energy of the structure.[63] Before coherency is
lost, splitting of diffraction spots normal to the interface indicates
that the two phases have face centered tetragonal crystal structures
with the c axes normal to the coherent interface and the two common
a axes lying in the {100} interface. The separation of the split
600 reflection shown in Fig. 3a corresponds to a lattice parameter
difference normal to the interface of $\Delta c = 1.0\%$ in this specimen aged
at 625°C for 1000 hrs. The strong contrast observed in the correspon-
ding bright field micrograph (Fig. 3b) arises from the coherency strains

at the interfaces. Also, displacement (δ) fringes are visible in this micrograph.

In many of the diffraction patterns taken of large coherent platelets, distinct streaks are observed lying along the $\langle 100 \rangle$ direction normal to the interface. The length of these streaks, as shown in Fig. 4a, corresponds to a distance of 15-20Å in the crystal. The origin of these streaks is probably the elastically strained region on either side of the coherent interface. In some cases two streaks separated by a small distance are observed passing through the same spot. It is not clear why two streaks occur, although the split streaks may be caused by magnetic deflection due to the ferromagnetic Ni-Fe rich phase.

The microstructure prior to loss of coherency consists predominantly of thin platelets about 500Å thick and 1-2μ in length with {100} habit planes (see Fig. 5a). During the initial stages, loss of coherency does not occur throughout an entire grain but rather specific variants of the platelet morphology develop interfacial dislocations preferentially as shown in Fig. 5b. Related to this observation is that different stages in the development of the dislocation arrays are often observed in adjacent particles. Another aspect of the selective nature of this process is that there appears to be no one critical particle thickness for loss of coherency but rather a range of particle thicknesses for which interfacial dislocations are observed. A good example of this observation is shown in Fig. 6 where two groups of four interfacial dislocations are seen at one platelet and all the surrounding platelets are still coherent.

As observed earlier by Butler and Thomas[24] and also in the present work, the semi-coherent interfaces develop more readily at higher temperatures for smaller platelet thicknesses and smaller mismatch. And once the interfacial dislocations form, the semi-coherent particles grow more rapidly than the coherent platelets (e.g. Fig. 5b). As to the effect of volume fraction on the loss of coherency, the symmetrical alloy containing an equal volume fraction of the two phases loses coherency sooner than the asymmetrical alloys aged at the same temperature. For example, Butler and Thomas observed some interfacial dislocations in foils of alloy A aged at 700°C for 40 hrs whereas no interfacial dislocations were observed in foils of the asymmetrical alloys aged for 200 hrs at the same temperature.

As the interfacial dislocations form, the interface changes its orientation towards a {110} plane. An example of this rotation is shown in the upper left corner of Fig. 5b where a few interfacial dislocations have formed. An even earlier stage of this process is shown in Fig. 6 where local rotation of the interface at the dislocations has occurred. As the interfacial dislocations develop further, this reorientation of the semi-coherent interface can result in a corrugated-shaped interface as shown in Fig. 7. The interfacial dislocations on the two surfaces have different Burgers vectors as demonstrated in the pair of micrographs shown in Fig. 8. Sometimes the interfaces become curved as they change orientation whereas in other cases the interfaces remain planar (see Figs. 5b and 7).

Diffraction contrast experiments have shown that the Burgers vectors of the interfacial dislocations are of the type $\bar{b} = a/2 \langle 110 \rangle$,[64]

which is a slip dislocation in fcc crystals, and in most cases lie at
45° to the {100} coherent interface (see Figs. 9 and 10). The diffrac-
tion conditions for dislocation contrast in fcc crystals are summarized
in Table I. The dislocation lines generally lie along ⟨100⟩ directions
in the interface although sometimes they are along ⟨110⟩ directions
or some intermediate orientation (see Figs. 11, 12 and 13). Most of
the observed semi-coherent interfaces contain one regular array of
parallel dislocations and in some cases a second set of dislocations
which are more irregular in appearance (see Fig. 13). Sometimes the
second set of dislocations is perpendicular to the first set and these
dislocations often appear to be situated at steps on the interface as
shown in Fig. 14.

Stereo micrographs of the interfacial dislocations have revealed
that some of the observed dislocations do not lie in the interface
but rather are extended into one of the phases. When viewed in stereo,
the arrowed dislocations in Fig. 15 are seen to be inclined to the
parallel dislocations at the interfaces and in some cases appear to
be connected to them. In addition, high voltage electron micrographs
have confirmed the observation of "stray" dislocations that do not
lie in the interface as reported earlier by Butler and Thomas (e.g. Fig.
16). Most of the micrographs show segments of interfacial dislocations
that terminate at the foil surfaces. However, as shown in Fig. 17,
these dislocations do in fact loop around the ends of the platelets.

The micrographs shown in Fig. 18 were taken of a foil with the
[011] zone axis parallel to the incident beam. Thus, the interfacial

dislocations within the areas A and B lie in or near the (001) plane. The separation of the dislocations in area A is about 225Å whereas those shown in area B have a spacing of about 300Å. This difference in dislocation spacing may be due to a slight difference in orientation of the two interfaces resulting in different projected spacings for the two sets of dislocations. These two micrographs also show examples of moiré fringes observed at these semi-coherent interfaces.

In these Cu-Ni-Fe alloys, it has been observed that enhanced particle coarsening occurs at some grain boundaries. Consequently, such large particles lose coherency sooner than the smaller particles in the matrix (e.g. Fig. 19).

D. Discussion

1. Tetragonal Structure and Related Effects

Prior to the loss of coherency, the two phases have face-centered tetragonal crystal structures (Bravais lattice: face-centered ortho-rhombic with a = b ≠ c) with the c axes normal to the coherent interface and the two common a axes lying in the {100} interface. Butler and Thomas[24] associated this tetragonal structure with the formation of the first set of interfacial dislocations. However, there is much evidence to substantiate the face-centered tetragonal structure of the fully coherent platelets. In thin foils containing large coherent platelets, splitting of the h00 reflections normal to the interfaces has been observed (see Fig. 3). Because two distinct spots are not observed, it seems likely that the two phases have constrained tetragonal structures with the c parameter varying continuously from the equilibrium values at the center of the platelets to an average

value at the interface. Then when the first set of interfacial dis-
locations are formed, partial loss of coherency occurs and the two
phases have unconstrained tetragonal structures as evidenced by the
resolvable split spots.[24]

In order to explain the diffuse sidebands observed on x-ray dif-
fraction patterns of Cu-Ni-Fe alloys, Daniel and Lipson[28] postulated
that the two coherent phases were tetragonal with the c axes normal
to the platelet interface. The resulting modulation of the lattice
parameter caused the observed sideband formation, analogous to a dif-
fraction grating. Because the atomic scattering factors for Cu, Ni
and Fe are about equal, this lattice parameter variation across the
platelets seems to be the most feasible explanation for this observed
diffraction phenomenon. Furthermore, in order to explain the contrast
in electron micrographs of Cu-Ni-Fe alloys, Cadoret and Delavignette[65]
based their calculations on the lattice parameter variation normal to
the interface which causes a relative phase displacement of the electrons
as they pass through successive platelets. Other effects that might
contribute to the contrast, such as differences between the reciprocal
lattice vectors (g) of the two phases, the deviations from the Bragg
condition (s) and the extinction thicknesses (t_e), are negligible in
these Cu-Ni-Fe alloys.

Because of the difference in crystal structures of precipitate
and matrix, fringe contrast is often observed at interphase interfaces
under various diffraction conditions. The contrast characteristics of
various types of fringes have been described by Hirsch, et al.[66] When
the matrix is oriented for a strong diffraction condition and the
precipitate is not so oriented, or vice versa, then thickness fringes

are observed at the interface. Such fringes have the same character-istics as thickness fringes in a wedged shape crystal and are analogous to thickness fringes observed at grain boundaries when one grain is strongly diffracting and the other is not. If there is a relative displacement of the crystal lattice between the matrix and the coherent precipitate, then displacement (or δ) fringes may be observed at the interface when there is a strong matrix reflection and zero or weak precipitate reflections. Such δ-fringes are a sensitive measure of small coherency strains, and Oblak and Kear[67] have explained the δ-fringe contrast at coherent precipitate interfaces in a nickel-base alloy in terms of a geometric model[68] based on a tetragonal lattice distortion at the interface.

A third type of fringe contrast observed at interphase interfaces is moiré fringes which can give useful information about the lattice mismatch between the matrix and a precipitate. For the simple parallel moiré case where the two crystals differ only in lattice parameter and have the same crystal structure and orientation, the fringe spacing (D_m) is related to the misfit $(\delta = (d_1 - d_2)/\bar{d})$ by the formula[66]

$$D_m = \frac{d_1 d_2}{d_1 - d_2} = \frac{\bar{d}}{\delta}$$

where d_1 is the interplanar spacing of the operating reflection. For the simple parallel case, the moiré fringes are normal to the reciprocal lattice vector (g). By measuring D_m from a micrograph and knowing d_1 for the operating reflection then the constrained misfit can be cal-culated. An example of a moiré pattern produced at an interphase interface by the 51$\bar{1}$ reflection is shown in Fig. 18a; and the calculated

misfit from the measured fringe spacing is $\delta = 0.7\%$ for this sample of

alloy 2 aged 200 hrs at 775°C. When the $0\bar{2}2$ reflection is operating

moiré fringes with a larger spacing are observed as shown in Fig. 18b.

In this micrograph note the parallel interfacial dislocations on the

central particle which appear to be moiré fringes. However, as discussed

by Hirsch, et al.,[66] contrast images arising from interfacial dislocations

and moiré patterns will only be coincident when the resolved edge com-

ponent of the Burgers vector equals the misfit and when the g vector

is normal to the direction of the dislocation lines. Thus, the striped

contrast on the central particle (cf. area A in Fig. 18b) cannot be

moiré fringes of the parallel type since the lines are not perpendicular

to the operating g vector.

2. Structure and Energetics of Equilibrium Semi-Coherent Interfaces

A single interphase interface in this coherent spinodal micro-

structure is similar to the interface between a thin film and the sub-

strate onto which it is evaporated. Detailed theories of dislocation

interphase boundaries in thin films have been developed by Frank and

van der Merwe,[69,70] van der Merwe[71] and Brooks.[72] A recent review

of these theories including experimental observations for thin film and

precipitate interphase boundaries has been given by Aaronson, et al.[73]

It seems appropriate to use the results of these theories in explaining

the observations made on the loss of coherency in these Cu-Ni-Fe alloys.

The equilibrium crystal structures of the two phases are face-

centered cubic with a small difference in lattice parameters. Just

prior to loss of coherency the two phases are face-centered tetragonal

with the two common a axes in the {100} interface and c axes normal to the interface. The Ni-Fe rich phase has $c_1 < \bar{a}$ whereas the Cu rich phase has $c_2 > \bar{a}$. The final semi-coherent microstructure of these spinodal alloys is expected to be spherical particles of the minor phase surrounded by a dislocation network containing three non-coplanar Burgers vectors that completely relieve the lattice mismatch along the three cube axes.

Based on geometrical considerations the most efficient misfit-accommodating dislocations are pure edge dislocations with the Burgers vector lying in the interface plane and the extra half plane of atoms extending into the phase with the smaller lattice parameter (i.e. the Ni-Fe rich phase). However, it is often possible that more than one type of misfit dislocation will satisfy the above condition; and Aaronson, et al.[73] have discussed this possibility and have concluded that for θ' platelets in Al-Cu the observed interfacial dislocations with $\bar{b} = a \langle 100 \rangle$ do not give the dislocation configuration of minimum energy based on a simple isotropic elasticity estimate of the dis-location network energy. They also discuss other examples of observed interfacial dislocation structures that are not the minimum energy configuration as expected from theoretical considerations.

The observed interfacial dislocations in these Cu-Ni-Fe alloys have Burgers vectors inclined at 45° to the interface and are thus only partly effective in accommodating the lattice mismatch. Apparently, the kinetics of formation for such dislocation arrays are more favorable than for the creation of more efficient dislocations. Similar misfit-accommodating dislocations at {100} interphase boundaries have been

observed by Matthews in gold-silver and platinum-gold evaporated thin films[74] and by Jesser and Matthews in evaporated thin films of iron on copper,[75,76] cobalt on copper[77] and chromium on nickel.[78] The work of Levine, et al.[79] on diffusion-induced defects in silicon showed that glide dislocations moved to the position in the crystal corresponding to the steepest solute concentration gradient and combined to give efficient misfit-accommodating dislocations with their Burgers vector lying in the "interface". Weatherly and Nicholson[80] have discussed in detail the capture of matrix dislocations at interphase boundaries, and their observations on the loss of coherency of γ' spheres in a Ni-base alloy, S laths in Al-Cu-Mg and needle-shaped β' in Al-Si-Mg provide convincing evidence of the general importance of this mechanism when the lattice misfit is less than ~5%. Thus, the dislocations present at a semi-coherent interface are not necessarily the most efficient ones or those of minimum energy but rather are often those dislocations that are most easily generated or most readily available to relieve the coherency strains. A recent review article by Kinsman and Aaronson[81] provides ample evidence from observations made on various interphase interfaces to substantiate this conclusion.

In explaining the loss of coherency in Cu-Ni-Fe alloys, it is useful to consider the free energy changes that occur for various interfacial structures. For this discussion the microstructure to be considered is an array of parallel platelets that are initially coherent and that subsequently become semi-coherent (see Fig. 20). The interfacial energy consists of two parts: (1) a chemical component due to the difference in atomic bonding across the interface and (2) a structural

component due to the elastic strain energy of the coherent interface

or to the interfacial dislocation energy. The total Helmholtz free

energy per unit volume is given by:

$$F_{total} = (F_1 f_1 + F_2 f_2) + 2\left(\frac{L}{\lambda}\right)\gamma + 2\left(\frac{L}{\lambda}\right)E_{struct}$$

where

F_i = chemical free energy of ith phase per unit volume

f_i = volume fraction of ith phase

γ = chemical interfacial energy per unit area

E_{struct} = structural interfacial energy per unit area

λ = modulation wavelength or distance between alternate platelets

of the same phase

L = characteristic length of unit volume (see Fig. 20)

and the subscripts 1 and 2 denote the Ni-Fe rich and Cu rich phases

respectively. It is expected that the coherent platelets have chemical

compositions corresponding to the coherent miscibility curve and thus

differ in composition from the semi-coherent platelets. Consequently,

the chemical free energy terms (F_i) and the chemical interfacial energies

(γ) will differ for the coherent and semi-coherent particles.

In order to estimate the structural interfacial energies for the

coherent and semi-coherent states, the theoretical expressions derived

by van der Merwe[82,83] for the interfacial energy of a thin film evaporated

onto a substrate have been used. The details of the calculations are

given in Appendix A where it is shown that the structural component of

the coherent interfacial energy in these Cu-Ni-Fe alloys is ~330 ergs/cm^2.

For the semi-coherent state, van der Merwe considered two simple cubic

crystals in parallel orientation with the misfit in only one direction

being accommodated by parallel edge dislocations (see Fig. 21). Using
the equations resulting from van der Merwe's analysis, it is shown in
Appendix A that the structural interfacial energy is ~250 ergs/cm^2 for
a semi-coherent interface containing one set of dislocations with the
Burgers vector inclined at 45° to the interface whereas this component
of the energy is only ~225 ergs/cm^2 for a (110) interface with $\bar{b}$ = a/2
[1$\bar{1}$0] lying in the interface. As the second set of interfacial dis-
locations is formed, the interfacial energy will be further reduced.

3. **Proposed Mechanism for the Formation
   of Interfacial Dislocations**

Four mechanisms have been suggested for the loss of coherency of
growing particles:

(a) The climb or glide of dislocations from an exterior source to
    the particle-matrix interfaces.

(b) The growth of small loops inside the particle.

(c) The punching of dislocation loops at or close to the particle-
    matrix interfaces.

(d) The accumulation of point defects from the matrix to form
    dislocation loops that subsequently grow.

The first two mechanisms have been experimentally observed.[80] The
calculations of Weatherly[84] for prismatic punching of dislocation loops
at coherent particles indicate that the conditions necessary for this
mechanism to occur are quite stringent. For example, he estimated
that the unconstrained transformation strain of a plate-shaped pre-
cipitate must be greater than 10% for loss of coherency to occur by
punching. The work of Brown, et al.[85] on the loss of coherency in a

Cu-Co alloy shows that it is important to consider both a stress criterion and an energy criterion for loss of coherency by punching.

DeFontaine[86] has derived an approximate energy criterion for the loss of coherency in modulated structures, such as in these Cu-Ni-Fe alloys. His model is based on the prismatic punching mechanism for the generation of dislocation loops. Consequently, the results of this model predict that the maximum or critical modulation wavelength (λ_o) for loss of coherency decreases as the misfit (δ) increases. However, in these Cu-Ni-Fe alloys it is observed that loss of coherency occurs for smaller wavelengths at higher aging temperatures where the misfit is less.[24] Because the strain energy density in a modulated structure is independent of the wavelength, deFontaine used a critical volume to surface ratio as the criterion for loss of coherency. Thus, his model predicts that the symmetrical alloy should lose coherency at a smaller wavelength than the asymmetrical alloys; and this effect is observed in Au-Pt alloys[49] and in Cu-Ni-Fe alloys. For example, the critical platelet thickness for loss of coherency in these Cu-Ni-Fe alloys is ~500Å even though the critical modulation wavelength is $\lambda_o \simeq 950$Å for the symmetrical alloy aged at 775°C[24] and $\lambda_o \simeq 1500$Å for the asymmetrical alloy (#2) aged at 800°C (see Fig. 5). Therefore, the energy criterion for loss of coherency in modulated structures seems to be dependent on a critical volume to surface ratio.

Based on the experimental observations described previously and the results of other studies reported in the literature, the most probable mechanism for loss of coherency in these Cu-Ni-Fe alloys is by the capture of slip dislocations from the matrix with subsequent climb of the

dislocations at the interfaces to give the observed dislocation arrays.
Because of the high density of observed interfacial dislocations, it is
necessary to explain how one slip dislocation can multiply to give many
misfit dislocations lying in the interface. It is proposed that this
multiplication process occurs by a slip dislocation forming a spiral
around the platelet. First it will be shown that there is a preferential
stress interaction between a coherent {100} interface and a slip dislocation
with its Burgers vector inclined at 45° to the interface. Then the
nucleation step in the multiplication process will be considered whereby
the dislocation becomes extended along one interface. The subsequent
spiraling of the dislocation around the platelet is in some ways analogous
to the formation of helical dislocations. Weatherly and Nicholson[80] have
observed a similar dislocation mechanism for the loss of coherency of rod
shaped precipitates, and Matthews[87] has proposed a helical dislocation
mechanism to explain the formation of misfit dislocation loops around
spherical particles.

Because the coherent platelets are relatively thin with a thickness
to length ratio of 0.05, it is reasonable that the coherency stress
normal to the (001) interface is partially relaxed so that the lattice
parameter along this direction approaches the equilibrium value in the
two phases, whereas the atomic spacings along the two cube axes parallel
to the interface are elastically constrained to some average lattice
parameter. That is, the two phases in the coherent platelet micro-
structure have face-centered tetragonal crystal structures with the two
common a axes parallel to the interface and the c axes normal to it. And
there is much evidence to support this description of the coherent

microstructure and the corresponding stress conditions at the coherent interfaces.

Based on the face-centered tetragonal structures, the corresponding components of the coherency stresses are such that the stress acting normal to the interface (σ_{zz}) is much less than the two stress components acting in the interface. Furthermore, the shear components are either zero or negligible compared to the two stress components acting in the interface. The resolution of this assumed coherency stress system onto the various slip planes and slip directions is given in Appendix B. This model for the interaction between coherent platelets and glide dislocations is based on an analysis by Dahlgren[62] for the calculated yield stress of such a microstructure.

An interesting result of the calculations given in Appendix B and summarized in Table II is that for the assumed coherency stresses there is no preferential stress interaction between a coherent interface and a dislocation with its Burgers vector parallel to the interface. Although the assumed model is an approximation to the actual physical situation, this result provides an explanation why the observed interfacial dislocations have Burgers vectors inclined at 45° to the {100} interfaces. The extra half plane of atoms associated with the edge component of the interfacial dislocation will lie in the phase with the smaller lattice parameter; and the relative orientation of this extra half plane of atoms depends on both the direction of $\bar{b}$ and the sense of the dislocation line tangent ($\hat{t}$). That is, the preferential attraction between a dislocation with a given $\bar{b}$ and a specific variant of the {100} interface depends on the relative orientation of the extra half plane of atoms

with respect to the phase with the smaller lattice parameter.

In an article describing interfacial dislocations in evaporated thin films, Jesser and Matthews[75] have proposed a mechanism whereby a slip dislocation extending through both layers of the evaporated film becomes extended along the interface as the film grows in thickness. Because the coherent interface between a metal film evaporated onto a metal substrate is similar to the coherent platelet interfaces in these Cu-Ni-Fe alloys, it seems likely that the same mechanism is operative in alloys with modulated structures where a captured slip dislocation can become extended at the interface due to the coherency stresses. The physical situation is shown in Fig. 22a where a coherent platelet interface is intersected by a slip dislocation with its Burgers vector inclined at 45° to the interface. The elastic strain due to the coherent interface causes the dislocation line to bow out in opposite directions in the two phases. As the platelet thickness increases, the bowed out segments become approximately as shown in Fig. 22b at which point the glide force acting on the dislocation becomes equal to the line tension of the misfit dislocation. With a further increase in the platelet thickness, the dislocation will extend by glide along the intersection of the slip plane with the interface as shown in Fig. 22c. Jesser and Matthews[75] have given expressions for the resolved shear stress, the glide force acting on the dislocation and the critical film thickness at which extension of the dislocation occurs.

Since electron microscopy observations have shown that such a mechanism does occur at the coherent platelet interfaces in these Cu-Ni-Fe alloys (cf. Fig. 16), it is suggested that the coherency stress

activated extension of a slip dislocation at the interface assists in the nucleation step of the proposed multiplication process. Because of the high aging temperature (800°C ≈ 0.75 T_m), dislocation climb can readily occur; and it has been shown that a stress acting on a crystal is equivalent to a supersaturation of point defects.[88] That is, the coherency stresses provide a driving force for dislocation climb which can occur rapidly at the aging temperature studied. The slip dislocation extends by glide along ⟨110⟩ in the interface which is the line of intersection of a {111} slip plane and {100} interface. But because the misfit directions are along ⟨100⟩ in the interface, the dislocation line will climb so that it lies along ⟨100⟩ in order to better accommodate the misfit. At these high temperatures it may be that the {110} planes are also active slip planes in fcc crystals, in which case the dislocations could glide conservatively so as to be extended initially along ⟨100⟩ directions in the interface. The sequence of steps in the proposed dislocation multiplication process is shown in Fig. 23 where it has been assumed that the initial dislocation has $\bar{b}$ at 45° to the interface and is in screw orientation which has lower energy than a dislocation of edge or mixed character. This process depends on the availability of suitable slip dislocations and is both thermally and stress activated occurring at some critical combination of temperature and platelet thickness. As observed in this study and also by Butler and Thomas,[24] loss of coherency occurs more rapidly at higher temperatures and for smaller platelet thicknesses at the higher temperature which is consistent with the proposed mechanism.

The resulting dislocation configuration will have a segment of partial edge dislocation lying along ⟨100⟩ in the interface connected by a curved segment of mixed character to the initial screw dislocation (see Fig. 23c). The continued development of the spiral dislocation around the platelet is in some ways analogous to the development of helical dislocations. Weertman[89] showed that the equilibrium form of a dislocation acted upon by an external force is either a straight line or a helix. The total force acting on the dislocation is the sum of the chemical force $\bar{F}_c = \hat{\xi} \times \tilde{b}$, and the mechanical force, $\bar{F}_s = \hat{\xi} \times \tilde{G}$, where $\hat{\xi}$ is the unit tangent to the dislocation line, $\tilde{b} = (kT/b^3)(\ln N_o/N)\bar{b}$ and $G_i = \sum_j \sigma_{ij} b_j$ and N_o and N are the equilibrium and actual vacancy concentrations. In subsequent papers by Weertman[90] and deWit[91] it has been shown that helical dislocations can develop from initially straight dislocations of screw, edge or mixed character acted upon by an external force. For screw dislocations bulk diffusion of vacancies is required whereas an edge dislocation can develop into a helix by core diffusion without any net transport of point defects. And a mixed dislocation can also grow into a helix by core diffusion if the axis of the helix shifts as the helix grows. A good summary on the formation of helical dislocations is given in the book by Hirth and Lothe.[92] It is important to note that a helical dislocation can develop in the absence of a supersaturation of point defects and without long range diffusion.

For the present case of a slip dislocation winding around a coherent platelet, the main force acting on the dislocation is the coherency stresses developed at the interface. The nature of these stresses is such as to provide a driving force for the climb of the dislocation

into a configuration around the platelet interface that relieves the elastic coherency strains. Based on the theoretical analysis of helical dislocations, it seems plausible that the extended dislocation at the interface and the curved, mixed dislocation segment acted upon by the coherency stresses can lead to the development of a spiral dislocation around the platelet. Since the tangent to the dislocation line points in opposite directions at the two interfaces, the extra half plane of atoms associated with the edge component lies within the same phase and the spiral dislocation can be thought of as a series of dislocation loops intersected by a continuous dislocation line (see Fig. 24). As shown in the electron micrograph of Fig. 17, the interfacial dislocations observed in these Cu-Ni-Fe alloys loop around the ends of the platelets. Also, the micrograph in Fig. 16 shows dislocations being laid down along the interface which is consistent with this proposed mechanism for the loss of coherency.

As the dislocation continues to wind around the platelet, each turn of the spiral is expected to be pinched off and to form a loop as shown in Fig. 23d, leaving behind the original dislocation. The dislocation line on opposite sides of the spiral is of opposite sense or direction and thus the two segments are attracted and will form a closed loop. If the interfaces rotate to the {110} plane containing $\bar{b}$, then the loops become pure edge prismatic loops. Before the first turn of the spiral forms a loop, successive turns of the spiral will be in various stages of formation so that many dislocation loops can be generated from a single slip dislocation captured at the interface. This same dislocation mechanism can produce other sets of interfacial dislocations with

different Burgers vectors. However, the subsequent dislocations will interact with the initial set of dislocations and will thus be hindered in climbing around the particle (see Fig. 13 a-b). This proposed model for the spiraling dislocation is similar in many respects to a dislocation climb[93,88] source which is a pinned dislocation that forms a spiral by climbing out of its glide plane.

Experimental evidence to support the proposed model for loss of coherency has been obtained by aging a sample of alloy 2 at 800°C for 10 hours, reducing the thickness ~20% by cold rolling and then aging an additional 8 hours. Thin foils prepared from this deformed and aged specimen contained some particles that were beginning to lose coherency, whereas foils prepared from the same material aged for 100 hours at 800°C but not deformed showed no evidence of loss of coherency.

4. Change in Particle Morphology With Loss of Coherency

The rotation of the semi-coherent interface toward a {110} orientation can now be understood in terms of the proposed model for loss of coherency. As shown previously, a coherent interface attracts preferentially slip dislocations with Burgers vectors inclined at 45° to it. In Appendix A it is shown that a {100} semi-coherent interface with $\bar{b}$ at 45° to it has a larger structural interfacial energy than a {110} interface which contains $\bar{b}$. This difference in interfacial energy provides a torque that tends to rotate the interface toward a {110} orientation. The local rotation of the interface plane at interfacial dislocations is clearly shown in Fig. 6. As the semi-coherent interfaces rotate, the initially coherent {100} platelets become semi-coherent rods with faces parallel to {110} planes and the rod axes along ⟨100⟩ as shown in Fig. 7.

Many semi-coherent particles are observed that only have interfacial dislocations in parallel interfaces which have rotated away from the initial {100} orientation (see Fig. 5b). This observation is consistent with the proposed model of a spiral dislocation around the platelet and the subsequent rotation of the semi-coherent interfaces.

After the particle loses coherency, it is observed that enhanced particle coarsening occurs with respect to the coherent platelets (see Fig. 5b). Weatherly and Nicholson[80] have also observed this effect in the coarsening of θ' particles in Al-Cu; and the kinetic measurements of Boyd and Nicholson[94] for the coarsening of θ' platelets indicate that once the coherent particles attain a certain diameter and size distribution the coarsening rate diminishes to an almost negligible rate. These observations indicate that a coherent interface imposes a restriction on the final size of the particle. If the increase in elastic strain energy is greater than the reduction of chemical interfacial energy, then the coherent particle will not coarsen. Once a particle loses coherency, it will coarsen preferential as the remaining coherent particles dissolve. This preferential coarsening of semi-coherent particles has been considered by Brown, et al.[85] who discussed the energy criterion for which the semi-coherent state is stable with respect to the coherent one; and they also showed that for an intermediate range of particle sizes the semi-coherent state is metastable compared to the coherent one.

E. Summary

The transmission electron microscopy observations have revealed some unusual effects associated with the loss of coherency in spinodally decomposed Cu-Ni-Fe alloys. Slip dislocations with their Burgers vectors inclined at 45° to the initially coherent {100} interfaces are observed, even though such dislocations are only partly effective in accommodating the misfit at the interfaces. Unusual dislocation configurations are observed with some dislocation lines extending into one of the phases, suggestive of a complex climb mechanism. Also, the process occurs preferentially at a few platelets while the other platelets in the same grain remain coherent. As coherency is being lost, the initial {100} interface is observed to rotate toward a {110} plane.

The proposed mechanism for the spiraling of an adsorbed slip dislocation around the coherent platelet is able to explain these observations. The operation of this mechanism is dependent on the availability of suitable slip dislocations present in the crystal and occurs by a rather complex climb process that is thermally and stress activated. The rotation of the interface is related to the observation that the Burgers vectors of the interfacial dislocations are inclined at 45° to the {100} interfaces. The proposed dislocation mechanism for loss of coherency is consistent with other experimental observations made on other alloys as reported in the literature.

III. MECHANICAL BEHAVIOR OF SEMI-COHERENT PARTICLES

A. Introduction

When the microstructure of these decomposed Cu-Ni-Fe alloys is still coherent, the flow stress is proportional to the difference in compositions between the two phases and the lattice mismatch across the interface seems to be an important factor in the strengthening.[24,25,58] The difference in elastic constants between the two phases also contributes to the strengthening of alloys with modulated structures.[95] In order to study the effect of interfacial dislocations on the mechanical behavior of a modulated microstructure, tensile specimens were aged at 775°C and 800°C for various times to produce specimens containing coherent and semi-coherent particles. The results of the mechanical testing indicate that interfacial dislocations strengthen the two phase structure and that large coherent platelets about to lose coherency enhance the initial work hardening rate. Transmission electron microscopy showed that in specimens strained 5% dislocation tangles had formed without evidence of particle by-passing and that in specimens pulled to failure (15-20% ε) large slip bands and particle shearing had occurred. Also, discontinuous grain boundary precipitation was observed in some of the aged specimens. These experimental results are discussed in relation to other studies reported in the literature.

B. Experimental Procedure

Some of the tensile specimens for this study were machined from ~35 mils thick sheet material of alloy 2 (64% Cu-25% Ni-9% Fe) which had been fabricated in the same way as described previously. One group of

specimens was made from 12 mils thick sheet that had been annealed and cold rolled to that thickness. These thinner specimens were made in order to duplicate as nearly as possible the heat treating conditions of 8 mils thick coupons used earlier in studying the loss of coherency process (see Part II). The machined tensile specimens were encapsulated in evacuated quartz tubes, solution treated at 1050°C, quenched in the quartz tubes into ice water and then aged for various times at 800°C and 775°C. The specimens aged at 800°C were solution treated for 10 hrs at 1050°C in order to produce a large grain size to facilitate examination of thin foils in the electron microscope, whereas the specimens aged at 775°C were solution treated for only 2 hrs at 1050°C. The resulting grain sizes (average diameter of inscribed circle) of the three groups of tensile specimens, solution treated and aged for 10 hrs, were:

   (1) 0.151 mm for 35 mils thick specimens aged at 800°C

   (2) 0.098 mm for 35 mils thick specimens aged at 775°C

   (3) 0.074 mm for 12 mils thick specimens aged at 775°C

An Instron testing machine was used to pull the flat tensile specimens which had 1 in. gage lengths and 1/8 in. gage widths. A drawing of the specimen configuration is given in Fig. 25. The 35 mils thick specimens were pulled using 1/4 in. diameter pin grips whereas the 12 mils thick specimens were held by self-clamping, vice grips. Before testing, the specimens were hand ground through 600 grit wet paper to remove surface irregularities and the cross sectional areas were measured. Three specimens for each aging condition were tested at room temperature, two specimens being pulled to failure and one of them only being strained 5% for

subsequent examination in the electron microscope. The 35 mils thick specimens were pulled at a constant strain rate of 0.02 cm/min whereas the 12 mils thick specimens were pulled at 0.01 in./min (0.025 cm/min). The yield stress was measured at 0.2% strain offset, and the total elongation to failure was determined by the change in spacing of two lines scribed on the gage length. The reduced areas of the fractured specimens were measured and the ultimate tensile strengths calculated. The work hardening rates (i.e., the slope of the load-elongation curve) were measured at 1%, 2% and 5% plastic strain for all specimens tested and also at 10% plastic strain for the specimens aged at 800°C.

Polished sections from the grip areas of the tensile specimens were examined using an optical metallography. Thin foils for transmission electron microscopy were prepared from the grip areas and the deformed gage lengths following the same procedure described previously. The tensile specimens were initially hand ground on wet emery paper to a thickness of ~6 mils and then 2.3 mm diam discs were spark cut from them. These discs were further reduced in thickness to 2-3 mils using fine polishing paper and were then electropolished in a double jet polisher.

C. Experimental Results

The platelets in this decomposed Cu-Ni-Fe alloy remained coherent in all the specimens aged up to 100 hrs at 775°C and 800°C. Semi-coherent particles were only observed in specimens aged for 200 and 1000 hrs. The microstructures of undeformed samples aged for 10, 100 and 200 hrs at 775°C are shown in Fig. 26a-c. In the sample aged 200 hrs, some semi-coherent particles were observed although many of the platelets

were still coherent. The specimens aged for 1, 10 and 100 hrs at 800°C
had the same coherent platelet microstructure as shown in Fig. 26a-b,
although the volume fraction of the minor phase was somewhat less. For
example, in a sample aged 10 hrs at 800°C the platelet thickness was
$\sim\lambda/4$, whereas in a foil aged the same time at 775°C the thickness was
$\sim\lambda/3$ where λ is the wavelength. A semi-coherent particle in an undeformed
sample aged for 1000 hrs at 800°C is shown in Fig. 27a-c under three
different diffracting conditions which reveal the different sets of
interfacial dislocations. After aging for 1000 hrs at 800°C, the
initially coherent platelets have become more equiaxed, semi-coherent
particles as shown in Fig. 28. In such a microstructure, the interlamellar
spacing (λ) is no longer meaningful. The microstructural changes that
occurred during aging are summarized in Table III.

Optical micrographs taken of the polished grip areas are shown in
Figs. 29-33. Some of the areas in the 12 mils thick specimens aged
at 775°C showed a discontinuous grain boundary reaction (see Fig. 29),
whereas the thicker specimens only had grain boundary precipitates of
the minor (Ni-Fe rich) phase without any evidence of the discontinuous
reaction (see Figs. 31-33). A well-developed Widmanstätten pattern
is clearly shown in Fig. 33 taken of a specimen aged 1000 hrs at 800°C.

The data obtained from the tensile testing are given in Tables IV
and V. These results are summarized in Figs. 34-39 which show graphs
of the yield stress at 0.2% offset, total elongation to failure and
work hardening rates as a function of aging time for the three groups
of specimens. Stress-strain curves for the 35 mils thick specimens
aged at 775°C and 800°C and strained 5% are shown in Fig. 40.

Typical microstructures observed in tensile specimens strained 5% are shown in Figs. 41 and 42. The micrograph in Fig. 41b shows dislocation tangles that have formed at the interfaces. The interaction of slip dislocations (which are irregular in appearance) with the parallel misfit dislocations at a semi-coherent particle is shown in Fig. 42a-c. The dislocations visible in micrographs a and b have the appearance of slip dislocations with $\bar{b}$ = a/2 [110] or a/2 [$\bar{1}$01] since they are out of contrast for $\bar{g}$ 1$\bar{1}$1 (see Table I for $\bar{g} \cdot \bar{b}$ products). The parallel misfit dislocations are out of contrast for $\bar{g}$ $\bar{1}\bar{1}$1 and thus have $\bar{b}$ = a/2 [$\bar{1}$10] or a/2 [101]. The short segments of dislocation lines visible in micrographs b and c (see arrows) appear to have resulted from the reaction of the slip dislocations with the interfacial dislocations. Since these short segments are out of contrast for $\bar{g}$ 200, they have $\bar{b}$ = a[010], a[001] or a/2 [0$\bar{1}$1].

Deformed microstructures of specimens pulled to failure (~15% ϵ) are shown in Figs. 43 and 44. Sheared "coherent" platelets and heavy slip bands along ⟨110⟩ are shown in Fig. 43. The micrograph in Fig. 44 was taken of a foil in a [001] orientation containing one variant of the {100} platelets that was normal to the electron beam. Thus, the dense tangles of dislocations seen in this micrograph appear to be at the platelet interfaces lying in the plane of the foil.

D. Discussion

1. Mechanical Behavior

The microstructures of the specimens aged up to 100 hrs at both 775°C and 800°C contained relatively thin coherent platelets lying parallel to {100} planes. As the aging time increased from 1 hr to 100 hrs, this coherent microstructure coarsened. In the specimens aged 200 hrs at 775°C, some of the platelets were beginning to lose coherency; and a completely semi-coherent microstructure with more equiaxed particles was observed in the specimens aged 1000 hrs at 800°C. The mechanical behavior of the coherent microstructure in these decomposed Cu-Ni-Fe alloys has been analyzed in detail previously.[24,25,58] Because only the specimens aged for 1000 hrs contained completely semi-coherent particles, the present experimental results are insufficient to quantitatively analyze the strengthening effect of the interfacial dislocations.

For the specimens aged at 775°C, the decrease in the yield stress at 100 hrs is significantly different from the measured yield stresses at 10 and 200 hrs since it differs by more than two standard deviations from these values (see Table V). The systematic difference in the yield stresses of the 12 and 35 mils thick specimens was due to the smaller grain size of the 12 mils thick specimens which had been cold rolled and recrystallized. Overaging of the coherent platelets caused a decrease in the yield stress of specimens aged 10 hrs and 100 hrs, whereas the increase in yield stress at 200 hrs appears to have resulted from the development of interfacial dislocations which contributed to the strengthening. Considering the specimens aged from 1 to 100 hrs at 800°C, the decreasing yield stress with aging time resulted from

overaging of the coherent platelets. The data given in Tables III and IV for these specimens aged at 800°C suggest that the yield stress of this coherent microstructure is proportional to $\lambda^{-1/2}$. Although the specimens aged 1000 hrs at 800°C contained semi-coherent particles, the yield stress decreased further because of the marked differences in particle size and morphology between samples aged 1000 hrs and less than 1000 hrs at this temperature.

The electron micrographs of tensile specimens strained 5% (see Fig. 41) indicate that the coherent platelets are sheared by the slip dislocations as the material deforms. If the dislocations only moved through the softer Cu-rich phase and passed around the harder Ni-Fe rich particles, then a high density of dislocation loops should be observed. In order to deform one cubic micron of this material 5% (i.e. 0.05 ε), about 100 dislocations per square micron must pass through it. Thus, if the particles were being by-passed, then ~100 dislocation lines should be observed along each micron length of platelet interface (i.e., a dislocation spacing of ~100Å). Additional evidence that particle by-passing did not occur was the large displacements of sheared platelets along $\langle 110 \rangle$ observed in specimens pulled to failure (see Fig. 43).

In directionally solidified eutectic alloys containing large lamellae with spacings of 0.15 to 8 μm, it has been observed that the yield stress is proportional to $\lambda^{-1/2}$ where λ is the lamellar spacing.[96-98] By using a modification of the Hall-Petch theory, Shaw[96] has interpreted this result to mean that dislocations pass through the interface barrier at the upper yield point. Cline and Stein[97] have calculated the magnitude

of the image force due to the difference in shear moduli across the
lamellar interface in the Ag-Cu eutectic; and their results suggest
that a variation in the number of dislocations in a pile-up with the
lamellar spacing may explain the effect of the lamellar spacing on the
flow strength. The available experimental evidence suggests that
interfacial dislocations are probably present at the lamellar interfaces
in the directionally solidified Ag-Cu eutectic, and Cline and Lee[98]
have proposed a model for strengthening due to these interfacial
dislocations.

Because of the similarity in microstructures of the directionally
solidified Ag-Cu eutectic and the decomposed Cu-Ni-Fe alloys, it seems
likely that both types of structures deform in a similar manner. When
the coherent particles in the Cu-Ni-Fe alloys are very small and the
morphology is irregular and wavy ($\lambda < 200\text{Å}$) as shown in Fig. 1a-b, a
dislocation will encounter many obstacles as it glides through this
structure under an applied stress. As the particles grow and the
platelet morphology evolves, the interface barrier encountered by a
slip dislocation becomes more like that in the lamellar microstructure
of the directionally solidified eutectic alloys. The transmission
electron microscopy observations of Butler and Thomas[24] showing matrix
dislocations curving through the irregular, two phase structure when
$\lambda \sim 100\text{Å}$ and lying along the planar interfaces when $\lambda \sim 635\text{Å}$ support this
interpretation for the interaction of slip dislocations with the
interfaces.

The strengthening of the coherent microstructure in decomposed

Cu-Ni-Fe alloys arises from differences in the lattice parameters and also the shear moduli of the two phases. When the particles become semi-coherent, the coherency strains are relieved and thus the yield stress should be reduced. However, the experimental evidence suggests that the strengthening effect of the interfacial dislocations was greater than the reduction in strength due to the partial relief of the coherency strains

In age-hardening alloys, overaging is generally associated with a change in the slip mechanism from particle shearing to particle by-passing (i.e., an Orowan mechanism).[99] But because of the low dislocation densities observed in deformed specimens, dislocation by-passing of coherent platelets does not appear to be occurring in these Cu-Ni-Fe alloys even for $\lambda > 0.1$ μm. The large volume fraction (and high density of particles) of the minor phase in this spinodal alloy may prevent slip dislocations from passing around the coherent platelets. Since the data suggest that $\sigma_y \propto \lambda^{-1/2}$, the observed decrease in the flow stress for specimens aged up to 100 hrs may be due to dislocation pile-ups that occur in the larger coherent platelets analogous to the pile-up mechanism suggested to explain the dependence of flow stress on the lamellar spacing in directionally solidified eutectic alloys. If only single slip dislocations were being forced through this coherent micro-structure, then the flow stress would be proportional to λ^{-1}.

The work hardening rate at 1% strain has a maximum value for those Cu-Ni-Fe specimens aged 100 hrs (see Figs. 37-39). The microstructure after 100 hrs of aging contains coherent platelets that are large enough to lose coherency; but because of the difficulty in nucleating the

interfacial dislocations, the platelets are still coherent. As the

material is deformed, the initial slip dislocations will be captured at

the coherent interfaces since they will partially relieve the coherency

strains; and the electron micrographs of deformed specimens show slip

dislocations that have been captured at the interfaces (see Figs. 41b

and 44). The resulting reduction in the mobile dislocation density

may explain the larger work hardening rate observed for specimens aged

100 hrs.

For the specimens aged 1 to 1000 hrs at 800°C, the work hardening

rate at 10% strain has about the same value for all the specimens tested

(see Table IV). This result suggests that the dislocation density

becomes saturated after very large plastic strains and that the work

hardening rate becomes constant irrespective of the undeformed micro-

structure. Electron microscopy observations on specimens pulled to

failure also support this conclusion. As shown in Fig. 43, heavily

deformed slip bands have occurred in a tensile specimen strained ~17%.

It seems likely that the constant work hardening rate observed at 10%

strain may be due to the development of such large slip bands.

The interaction of slip dislocations with interfacial dislocations

is shown in the three electron micrographs given in Fig. 42a-c. The

slip dislocations visible in micrograph b (and also in a) have reacted

with the parallel interfacial dislocations seen in micrographs a and c.

As discussed in the previous section, the short segments resulting

from this dislocation reaction have $\bar{b}$ = a[010], a[001] or a/2[0$\bar{1}$1]. The

four possible reactions between the slip and interfacial dislocations

give resultant Burgers vectors of the types a⟨100⟩ or a/2⟨211⟩. Thus,

the short reacted segments have $\bar{b}$ = a[010] or a[001]. Furthermore, the dislocation reactions which give $\bar{b}$ = a/2⟨211⟩ are not expected to occur since the energy of the resultant dislocation is greater than the sum of the energies of the two initial dislocations (i.e., this reaction has a positive interaction energy).

If the semi-coherent particles are sheared during deformation, two effects that will contribute to the strengthening are the interfacial dislocations and the difference in shear moduli across the interface. In an analysis of the flow stress of directionally solidified eutectic alloys, the increase in the stress to overcome the image force at the interface has been given as[98]

$$\tau(\Delta G) = \frac{\Delta G}{8\pi}$$

where ΔG is the difference in shear moduli. For this Cu-Ni-Fe alloy, $\Delta G \sim 2\times10^3$ kg/mm^2[58] and thus $\sigma(\Delta G) \sim 80$ kg/mm^2 or $\sigma(\Delta G) \sim 160$ kg/mm^2 (cf. observed $\sigma_y \simeq 20$-25 kg/mm^2 as given in Tables IV and V). Cline and Lee[98] have also proposed a model for the interaction of slip and interfacial dislocations similar to the model for the interactions of dislocations with forest dislocations, such as a Frank network. From their analysis, the stress necessary for a dislocation to cross the interface dislocation network, $\tau(\Delta b)$, is approximately equal to

$$\tau(\Delta b) = \frac{G\Delta b}{2\pi b}$$

where Δb is the difference in Burgers vectors of the semi-coherent phases and G is the shear modulus of the matrix. For this Cu-Ni-Fe alloy, $\Delta b/b \sim 0.008$ and $G = 6.4\times10^3$ kg/mm^2 for the Cu-rich phase[58] giving a value of $\tau(\Delta b)$ of ~8 kg/mm^2 or $\sigma(\Delta b) \sim 16$ kg/mm^2. This estimate of the increase in stress is for the interaction of a slip dislocation with only one

set of interfacial dislocations. But if misfit dislocations with more

than one Burgers vector are at the interface, then this estimated

$\tau(\Delta b)$ should probably be multiplied by two or three. These estimates

for the strengthening due to the image force and the interfacial dis-

locations suggest that the image barrier is the dominant factor. However,

the tensile data did show a net increase in the flow stress as coherency

was being lost.

The observed interaction between slip and interfacial dislocations

suggests that junction formation may play a role in the work hardening

behavior of the semi-coherent microstructure. In studying the strain

hardening of single aluminum crystals during polyslip, Mukherjee, et al.[100]

found a good correlation of the data with the concept that attractive

junctions[101] play an important role in accounting for the rate of strain

hardening in fcc crystals. Although the reacted dislocations in Fig. 42

are not attractive junctions (since the interaction energy for a reaction

giving $\bar{b} = a\langle 100\rangle$ is zero), dislocations on other slip systems could

interact with the interfacial dislocations to give attractive junctions.

The total elongations to failure of the tensile specimens were

observed to increase with aging time (see Figs. 34 and 36). Metallography

showed that enhanced grain boundary coarsening and, in some cases, a

discontinuous grain boundary reaction had occurred in these decomposed

alloys (see Figs. 19, 29, 32 and 33). Also, as will be discussed in

detail in the last part of this thesis, the fracture mode changed from

intergranular to transgranular after aging this alloy longer than 10 hrs

at 775°C and 800°C. The increase in the total elongation with aging

was most likely due to the microstructural differences between the grain

boundaries and the matrix. Because the particles at some of the grain boundaries are larger than the matrix particles, these regions deform more readily than the matrix and consequently fail before the matrix. As the matrix structure coarsens, the mechanical behavior of the grain boundary regions and the matrix becomes comparable and the total elongation to failure increases.

2. Grain Boundary Reaction

As shown in Figs. 19, 32 and 33, enhanced particle coarsening occurred at some of the grain boundaries in this decomposed Cu-Ni-Fe alloy. Furthermore, in a 12 mils thick specimen aged for 100 hrs at 775°C, a discontinuous grain boundary reaction has been observed (see Fig. 29). Similar observations of grain boundary transformations in these Cu-Ni-Fe alloys aged at other temperatures have been made previously.[58,61,102] Earlier studies on Cu-Ni-Co and Cu-Ni-Fe alloys[103,104] also showed the occurrence of the discontinuous grain boundary reaction which resulted in softening as it consumed the fine precipitate structure of the matrix. The changes in microstructure of these copper-base alloys during aging follow the general sequence[105] of which Al-Ag alloys provide the prototype although a depleted grain boundary zone is not observed in the spinodally decomposed copper-base alloys. It was further noted in these studies by Geisler and co-worker[103,104] that when these copper-base alloys are very slowly cooled from the solid solution region the grain boundary reaction is suppressed, and a well developed Widmanstätten pattern is observed as in Fig. 33.

In studying the grain boundary reaction in the Al-Ag system, Aaronson and Clark[106] have shown that the driving force for (and therefore the

rate of) discontinuous precipitation is inversely proportional to the
extent to which continuous precipitation has occurred. The kinetics
of the discontinuous grain boundary reaction in Al-Zn alloys has recently
been studied.[107] Upon quenching from temperatures above the solvus,
those Al-Zn alloys lying within the miscibility gap quickly develop
composition fluctuations, or Guinier-Preston zones, which can be
detected by the small-angle X-ray scattering technique.[22,108,109]
Malhotra and Rundman[107] found that the growth of the discontinuous
precipitate at room temperature in Al-Zn alloys was inversely proportional
to the extent to which spinodal decomposition had occurred during the
quench. This observation suggests a possible explanation for the dis-
continuous reaction occurring in the 12 mils thick specimens aged at
775°C and not in the 35 mils thick material. Since the quenching rate
was more severe for the thinner material, the extent of spinodal
decomposition would have been less in these specimens. Consequently,
the quenched 12 mils thick specimens would have had a larger driving
force for the discontinuous grain boundary reaction than the 35 mils
thick specimens.

E. Summary

The mechanical strengthening of the coherent platelet microstructure
in this Cu-Ni-Fe alloy is associated with the differences in lattice
parameters and shear moduli between the two phases. When coherency is
lost, the strengthening is due to the difference in shear moduli and
also to the interfacial dislocations. This modulated structure deforms
by dislocations shearing through the coherent platelets; and the work
hardening rate appears to be influenced by the capture of slip dislocations

at the coherent interfaces. The microstructural differences between

the grain boundaries and the matrix seem to affect the total elongations

to failure of the aged tensile specimens. The discontinuous grain

boundary reaction that was only observed in the thinner specimens may

have resulted from a difference in quench rates between the 12 mils

and 35 mils thick specimens.

IV.   INTERGRANULAR FRACTURE OF DECOMPOSED
Cu-Ni-Fe ALLOYS

A.   Introduction

In earlier studies of spinodally decomposed Cu-Ni-Fe alloys[24,25,61]

in which the mechanical behavior was correlated with microstructural

changes, it was observed that the aged tensile specimens failed inter-

granularly with total elongations to failure of ~10%. The experimental

observations suggested that this mode of failure was due to microstructural

differences between the grain goundaries and the matrix. For the inter-

granular fracture of aged aluminum alloys, Gerberich, et al.[110] have

suggested that the stress intensity for crack nucleation shows a $d^{-1/2}$

dependence where d is the grain diameter. The objectives of the present

study were to analyze why spinodally decomposed Cu-Ni-Fe alloys fail

intergranularly and to determine the grain size effect for this mode

of failure. An explanation is given for the intergranular fracture

of these alloys based on an analysis of the failure of brazed joints.

B.   Experimental Procedure

An ingot of alloy 2 (64% Cu-27% Ni-9% Fe) was fabricated to 0.25 in.

thick material. After the final cold rolling, the material was annealed

in three batches using different annealing temperatures and times to

give three grain sizes ranging from 6 μm to 90 μm. The grain diameters

were measured from optical micrographs using the linear intercept method.

Standard flat tensile specimens and 2.5 in. square WOL fracture toughness

specimens (see Figs. 25 and 45) were machined from the annealed material.

The specimens were then solution treated at 1050°C, water quenched and

aged for one hour at 625°C to give the maximum yield strength as reported

earlier.[25,61] The fracture toughness specimens were fatigue cracked

and then loaded to failure using a MTS testing machine, and the tensile

specimens were pulled on an Instron testing machine.

The fracture surfaces were examined in a scanning electron microscope

to determine the mode of failure. Thin foils were prepared from the

undeformed grip areas of the tensile specimens for examination in the

electron microscope; and larger pieces from the grip areas were mounted

and polished for optical metallography. The X-ray microprobe was used

in order to measure any segregation that had occurred in these spinodally

decomposed specimens. The fractured tensile specimens aged at 775°C,

and 800°C were also examined in the scanning electron microscope.

C. Experimental Results

The graph given in Fig. 46 shows the linear dependence of the

experimentally measured yield stresses and stress intensities on $d^{-1/2}$.

The elongations to fracture were measured on 1 in. gage length tensile

specimens, and the values ranged from 29% for the small grain size

decreasing to 18% for the large grain size. The K_i values are plane

stress rather than plane strain values because of the large plastic zone

which preceded fracture. Furthermore, the stress intensity was measured

at the onset of crack growth so that this is not the critical stress

intensity but rather the stress intensities for initiation of slow crack

growth. The small grain size specimens failed on two orthogonal shear

planes which were 45° to the fatigue crack, whereas the intermediate

grain size specimen failed along one shear plane at 45° to the fatigue

crack and the large grain size specimen had a relatively flat, but

faceted, fracture with shear lips along the edges.

The fractography examination using scanning electron microscopy
showed that the fatigue cracks for all the specimens were intergranular
with no appreciable plastic deformation. During fracture testing, the
crack in the small grain size specimen propagated by a dimpled tearing
mechanism with small ledges on the fracture surface that appear to be
grain boundaries (see Fig. 47). For the large grain size specimen,
the crack propagated intergranularly with appreciable plastic deformation
as evidenced by the dimpled surfaces and the tearing which is shown
in Fig. 48. Some of the relatively flat grain boundaries have the
appearance of wavy or serpentine glide which is indicative of a ductile
fracture mode. The fracture surface of the intermediate grain size
specimen showed definite failure along some grain boundaries, although
not as pronounced as in the large grain size specimen, with numerous
tear ridges and dimples.

Optical metallography of the heat treated specimens showed that
along some of the grain boundaries discontinuous precipitation had
occurred. In the large grain size material, the jagged, saw-tooth
morphology of the precipitate was resolvable; whereas, in the small
grain size material a definite thickening of some grain boundaries was
observed. Transmission electron microscopy showed a characteristic
spinodal microstructure with wavy, irregular particles aligned along
{100} planes and with a wavelength of ~75Å (see Fig. 1a). Because of
the randomness of the grain boundary precipitation and the preferential
electropolishing that occurred along grain boundaries, no grain boundary
precipitates were observed in the thin foils of the test specimens.
However, in samples aged for very long times or at higher temperatures,

preferential coarsening of the spinodal microstructure and discontinuous pre-cipitation have been observed at some grain boundaries (e.g., Figs. 29 and 49).

The fracture surfaces of the tensile specimens aged at 775°C are shown in Figs. 50 and 51. A transition from intergranular to transgranular failure occurred after aging for 10 hrs at this temperature. The fracture surface of the specimen aged 10 hrs has some areas of ductile rupture (see Fig. 50); and although the specimens aged 100 and 200 hrs failed in a ductile manner, large cavities suggestive of grain boundary separation were observed as shown in Fig. 51b. The fractograph in Fig. 52 shows a good example of grain boundary separation that occurred in a tensile specimen aged 10 hrs at 800°C. The microstructures of these fractured specimens are shown in the optical micrographs of Figs. 31 and 32 which show particle coarsening along some of the grain boundaries.

Some X-ray microprobe results suggest that solute segregation may be occurring at the grain boundaries in this spinodally decomposed alloy. Microprobe analysis of the grain boundary precipitates observed after aging the alloy for 1000 hrs at 625°C showed ~20% increase in the Ni and Fe concentrations at the precipitates compared to the matrix with a cor-responding decrease in the Cu concentration (see Fig. 53). For a sample aged one hour at 625°C no change in composition was detected at the grain boundaries. But if the grain boundary zone were less than one micron wide (which is the diameter of the electron beam), then such zones would not be resolved using the microprobe.

D. Discussion

The experimentally observed dependence of flow stress on grain size may be explained on the basis of macroscopic yielding due to dislocation pile-ups or slip sources at grain boundaries and as represented by the Petch equation. Based on the analysis of Gerberich, et al.[110] for age-hardening aluminum alloys, the stress intensity to nucleate fracture at a grain boundary is given by the equation

$$K_{nucl} = (\phi/d)^{1/2} \varepsilon^* \ell E$$

where ϕ is a constant, d is the grain diameter, ε^* is the fracture strain at the grain boundary, ℓ is the width of the grain boundary region and E is Young's modulus. The present experimental results suggest that an equation of this general form may also be valid for the intergranular fracture of spinodally decomposed Cu-Ni-Fe alloys. The experimental observations suggest that preferential grain boundary precipitation causes softening and subsequent crack propagation at the grain boundaries. Or possibly, as suggested by the microprobe results, the intergranular failure results from solute segregation or preferential growth of the minor phase at the grain boundaries after aging for one hour at 625°C.

The fracture characteristics of this spinodally decomposed Cu-Ni-Fe alloy are similar to those of spinodally decomposed Au-Pt alloys as reported by Carpenter.[49] Because the kinetics of the grain boundary reaction are so rapid in Au-Pt alloys, the correlation between the intergranular fracture mode and the discontinuous grain boundary precipitation is more evident in that case. On the basis of his experimental observations, Carpenter concluded that the Au-Pt alloys failed at the

grain boundaries because of the softer material present there. Micro-hardness measurements made in the present study on a Cu-Ni-Fe sample aged for 1000 hrs at 625°C indicated qualitatively that the grain boundary precipitate regions are softer than the surrounding matrix. Because the indentation was larger than the grain boundary width, no quantitative microhardness data were obtainable. In an earlier study by Geisler and Newkirk,[103] it was observed that the discontinuous grain boundary reaction in Cu-Ni-Co alloys resulted in softening of the periodic microstructure present in the matrix.

For the tensile specimens aged at 775°C and 800°C, a transition from intergranular to transgranular failure occurred after aging for 10 hrs. This observation suggests that in the specimens aged 10 hrs or less the grain boundary regions had a lower yield stress, and possibly a higher work hardening rate, than the matrix. Then greater localized deformation in the softer grain boundary regions would lead to inter-granular failure. But in the tensile specimens aged more than 10 hrs, the matrix structure had coarsened to such an extent that the mechanical behavior of the grain boundary regions and the matrix had become com-parable. Consequently, the polycrystalline material deformed more uniformly and the mode of failure became transgranular. The electron microscopy observations described in Part III indicate that both phases deform together in this lamellar microstructure (see Figs. 43 and 44).

As suggested by Geisler,[105] the intergranular fracture along weakened grain boundaries in age-hardening alloys is analogous to the failure of butted joints formed by a thin layer of copper between steel or of solder between copper. More recently, Saxton, et al.[111] and

West, et al.[112] have studied the deformation and failure of brazed joints. Because of the structural similarity, the observations on the failure of brazed joints seem relevant to explaining the intergranular fracture of decomposed Cu-Ni-Fe alloys. The high load-carrying capacity of a joint brazed with a soft metal is a result of the development of triaxial stresses within the joint due to the difference in yield strengths between the joint material and the base material. Saxton, et al.[111] found that an increase in the work hardening capability of a braze metal results in higher tensile strengths for brazed joints. In studying the microscopic deformation of brazed joints, West, et al.[112] found that as the thickness-to-diameter ratio (t/d) decreases joint strains at any given stress decrease (i.e., greater plastic constraint of the joint) and that the stress to cause local yielding in the base metal decreases with increases in t/d. These results are related to the observation that as t/d increases more flow and strain hardening is permitted in the braze resulting in higher values for the interfacial shear stress, τ_{rz}, which is responsible for the triaxial stress state within the brazed joint.

In decomposed Cu-Ni-Fe alloys, preferential coarsening and discontinuous precipitation at the grain boundaries produce a microstructure there that is softer than that of the matrix. This interpretation is supported by the overaging effect observed in this alloy aged at 800°C (see Fig. 34). Also, the coarser grain boundary structure may have a larger work hardening rate than the matrix as suggested by the data for $d\sigma/d\varepsilon$ given in Figs. 37-39. After short aging times, the grain boundary regions are thin and cracks propagate through these regions after small total strains (but large local strains) leading to premature failure (see Figs. 34 and 36). As the grain boundary regions thicken

(i.e., t/d increases) and the matrix coarsens resulting in a lower "base" material strength, the triaxial stress state at the grain boundaries is partially relaxed due to greater plastic deformation of the matrix. Consequently, the total elongation to failure increases and the fracture surface shows more evidence of ductile failure. When the ultimate tensile strengths of the grain boundary regions and the matrix become comparable, then the mode of failure changes from intergranular to transgranular as shown in Figs. 50 and 51.

E. Summary

The intergranular fracture of decomposed Cu-Ni-Fe alloys, and other age-hardening alloys having discontinuous precipitation and preferential coarsening at the grain boundaries, appears to be caused by microstructural differences between the grain boundary regions and the matrix which result in the development of a triaxial stress state at the grain boundaries during deformation. The analogy with brazed joints is excellent, and the observations made by other workers on the failure of such joints are very helpful in understanding the inter-granular fracture of polycrystalline, age-hardening alloys such as Cu-Ni-Fe. Although these aged alloys are relatively ductile, failure occurs preferentially at the grain boundaries because of the softer material present there. The observed grain size dependence of the stress intensity to initiate fracture is similar to that proposed earlier to describe the intergranular failure of aged aluminum alloys.

V. CONCLUSIONS

A. Summary of Experimental Results

As the modulated structure in these spinodally decomposed Cu-Ni-Fe alloys coarsens, the coherent platelets appear to lose coherency by a complex climb process that involves the spiraling of captured slip dislocations around the particles. Because the Burgers vector of the initial slip dislocation does not lie in the interface, a driving force exists that tends to rotate the semi-coherent {100} interface toward the {110} plane containing $\bar{b}$. Due to the difficulty of creating interfacial dislocations, available slip dislocations are utilized in a dislocation multiplication process that produces many misfit-accommodating dislocation loops from a single dislocation captured at the interface. The proposed mechanism for loss of coherency is able to explain the various experimental observations.

In tensile specimens aged at 775°C and 800°C, overaging was observed to occur due to the coarsening of the coherent microstructure. Electron microscopy of deformed specimens showed that this Cu-Ni-Fe alloy with a lamellar microstructure deformed by particle shearing and that dislocation tangles developed at the interphase interfaces. The results indicate that the development of interfacial dislocations causes a small net increase in the flow stress even though such dislocations relieve the coherency strains at the interfaces. It was also observed that specimens containing large coherent particles which were about to lose coherency had a larger initial work hardening rate than specimens with larger semi-coherent particles or smaller coherent particles.

The intergranular fracture of these decomposed Cu-Ni-Fe alloys,

and other age-hardening alloys, is associated with microstructural differences and consequent property differences between the grain boundary regions and the matrix. Because the coarser grain boundary structure is softer than the matrix, localized yielding and greater plastic strain in such regions lead to premature failure. As observed earlier in aged aluminum alloys, the stress intensity to nucleate grain boundary cracks is proportional to the inverse square root of the grain diameter. Analogous to the observations made on the failure of brazed joints, the development of a triaxial stress state in the grain boundary regions may explain the observed fracture characteristics of decomposed Cu-Ni-Fe alloys.

B. Future Work to be Done

In order to demonstrate the validity of the proposed mechanism for loss of coherency in these Cu-Ni-Fe alloys, a single crystal experiment could be performed. A high density of slip dislocations with a specific Burgers vector could be introduced into the crystal by deforming it on a single slip system. Then when this deformed crystal was aged inside the miscibility gap, only two variants of the {100} platelets would be expected to lose coherency and only one set of interfacial dislocations would probably form if the proposed mechanism is correct. It would also be interesting to study other ternary Cu-Ni base alloys with larger lattice parameter differences between the two phases in order to determine the effect of lattice mismatch on the loss of coherency. By looking at alloys with a smaller volume fraction of the minor phase, the effect of particle shape on the loss of coherency process could be studied (e.g., a 70% Cu-21% Ni-

9% Fe alloy containing cuboidal particles[24]). In conjunction with such
a study, it would be informative to do a systematic study following
the changes in particle morphology and transformation kinetics as a
function of volume fraction by looking at several alloy compositions
across the miscibility gap inside and outside the spinodal.

The effect of the interfacial dislocations on the mechanical behavior
of these Cu-Ni-Fe alloys could be studied in more detail by studying
the temperature dependence of the yield stress and work hardening rate.
If more detailed mechanical tests were to be done, it would be advantagous
to determine the effect of quench rates on the kinetics of the discon-
tinuous grain boundary reaction in this alloy system. In order to
prevent intergranular fracture and premature failure in these decomposed
alloys, it would be necessary to change the grain boundary structure
by thermal-mechanical treatment. By slowly cooling the alloys from
the solid solution region, a Widmanstätten structure would develop
which would probably inhibit the discontinuous grain boundary reaction.
Another possibility would be to age for a short time just under the
solvus curve (e.g., 10 min at 800°C), quench to room temperature, cold
work and then anneal at a lower temperature (600-700°C). Such a thermal-
mechanical treatment has been used successfully at Bell Labs on Au-Pt
alloys. An alternative procedure that might work would be to age the
alloy for 10 min at 800°C and then step age for one hour at ~600°C.
The initial aging at 800°C may allow sufficient decomposition to occur
so that the grain boundary reaction would be inhibited at the lower
aging temperature.

APPENDIX A: CALCULATION OF STRUCTURAL INTERFACIAL ENERGIES

Van der Merwe[82,83] has derived theoretical expressions for the structural component of the interfacial energy in an evaporated thin film for the case of two simple cubic crystals in parallel orientation that differ in lattice parameter along only one cube axis. If the film thickness (h) and the misfit ($\delta = (a_1 - a_2)/1/2(a_1 + a_2)$) are sufficiently small, then a fully coherent boundary will have a lower energy than a semi-coherent one with the equilibrium configuration of misfit dislocations. Depending on the relative hardness and thickness of the crystals, the resulting elastic strain energy will be accommodated in either one or both of the crystals. The elastic energy required to homogeneously deform the thin film in one direction is[83]

$$E_{struct}^{coherent} = \frac{\mu_1 (1 - \nu_1) h \delta'^2}{1 - 2\nu_1} \tag{1}$$

where $\delta' = (a_1 - a_2)/a_1 \simeq \delta$ at small values, a_1 = lattice parameter of the overgrowth, a_2 = lattice parameter of the substrate, μ_1 = shear modulus of overgrowth and ν_1 = Poisson's ratio of overgrowth. As a first approximation, this elastic strain energy is doubled if the film is homogeneously deformed in two directions. And for the case of coherent precipitates, the film thickness (h) corresponds to one-half of the platelet thickness. Because this equation is for the case where all the elastic strain energy is accommodated in the thin film, it gives too large an energy for the case where both crystals are deformed elastically to accommodate the misfit.

As the film grows, a critical thickness is reached at which misfit-accommodating dislocations lower the structural interfacial energy as shown by van der Merwe.[83] The physical situation treated by van der Merwe is that of two simple cubic crystals in parallel orientation with the misfit in only one direction being accommodated by parallel edge dislocations (see Fig. 21). By treating the interaction across the boundary with a sinusoidal force law and the interaction within a given crystal on the basis of an elastic continuum, the following expression is derived for the structural interfacial energy of two semi-infinite crystals:[82]

$$E_{struct}^{semi-coh} = \frac{\mu c}{4\pi^2} \{1 + \beta - (1 + \beta^2)^{1/2} + \beta \ln[2\beta(1 + \beta^2)^{1/2} - 2\beta^2]\}$$

$$\beta = 2\pi\delta(\Omega/\mu)$$

$$\frac{1}{\Omega} = [(1 - \nu_1)/\mu_1] + [(1 - \nu_2)/\mu_2]$$

(2)

where $c = 1/2(a_1 + a_2)$, μ = shear modulus at the boundary, μ_1 and μ_2 = the shear moduli within 1 and within 2 respectively, and ν_1 and ν_2 = Poisson's ratio within 1 and 2. In a subsequent paper van der Merwe[83] showed that the interfacial energy for a film of "infinite" thickness is very nearly the same as for a film of finite thickness greater than one-half the separation of the misfit dislocations. Although the case of misfit in two directions has not been treated, van der Merwe[71] suggested that to a first approximation the energies of the two sets of dislocations are simply additive and one can ignore the interaction between intersecting dislocations.

Loss of coherency occurs for the critical value of misfit, δ'_c, at which $E_{struct}^{coherent} = E_{struct}^{semi-coh}$. If one assumes that the critical misfit

is sufficiently small so that $\beta^2 \simeq 0$ and that $\nu_1 = \nu_2 = \nu$, the following expression is obtained:[83]

$$\ln \frac{4\pi\delta_c'\mu_1/\mu e}{(1-\nu)(1+\mu_2/\mu_1)} + \frac{2\pi(1-\nu)^2(1+\mu_1/\mu_2)h\delta_c'}{(1-2\nu)a_1} = 0 \qquad (3)$$

where $e = 2.72$, the natural base number. For $\nu = 1/3$ and $\mu_1 = \mu_2 = \mu$, the critical thickness of the overgrowth corresponding to δ_c' is[73]

$$h_c = \frac{3a_1[1 - \ln(3\pi\delta_c')]}{16\pi\delta_c'} \qquad (4)$$

This last equation can be used to estimate the critical thickness of a coherent platelet $(2h_c)$ at which misfit dislocations lower the structural interfacial energy. The misfit parameter, δ, used by van der Merwe in deriving the above expressions is related to the resolved edge component of the Burgers vector $(b_\perp)$ lying in the interface and the distance between the misfit dislocations (m) by the Brooks formula:

$$m = \frac{b_\perp}{\delta} \qquad (5)$$

This formula applies to the situation where all the misfit across the interface is accommodated by the dislocations.

The above equations resulting from van der Merwe's analysis will be used to estimate the energies of various interfacial structures in these Cu-Ni-Fe alloys. The misfit parameter for these alloys aged at 775°C is $\delta \simeq 0.8\%$ normal to the interface as coherency is being lost as measured from moiré fringes (see Fig. 18) and from split diffraction spots.[24] This value is probably representative of the equilibrium misfit parameter (i.e. the unconstrained misfit) for the semi-coherent particle because of the stress relaxation normal to the platelet inter-face. Using this value of $\delta = 0.8\%$ and $a_1 \simeq \bar{a} = 3.59\text{Å}$, the critical

thickness of the platelets for loss of coherency is found from Eq. (4) to be $2h_c \simeq 200\text{Å}$. This value is in good agreement with the calculations of van der Merwe[83] where it was found that for a critical misfit of ~0.8% the corresponding thin film thickness was about 25 atomic layers (i.e. $h_c \simeq 90\text{Å}$). Because this calculated value is less than the observed value of ~500Å for the coherent platelets, the formation of interfacial dislocations is probably hindered by the nucleation step in the loss of coherency process.

To calculate the structural interfacial energy for the coherent interface, an appropriate thickness of the platelet must be used. An upper limit for this energy is given by taking $h = 250\text{Å}$ which is one-half of the observed thickness of the coherent platelets, and a lower limit is given by using the above calculated critical thickness for loss of coherency (i.e. $h = 100\text{Å}$). Taking $\mu_1 \simeq \bar{u} = 7.3 \times 10^{11}$ dyn/cm^2,[58] $\nu_1 = 1/3$, $\delta' = 0.8\%$ and using these two values for h, the coherent structural energy for misfit along one direction is found from Eq. (1) to be $E_{\text{struct}}^{\text{coherent}} = 95\text{-}235$ ergs/cm^2 with a mean value of 165 ergs/cm^2. For misfit along two cube directions the total structural interfacial energy is ~330 ergs/cm^2.

For the semi-coherent interface, two cases will be considered: (1) a (100) interface with the Burgers vector ($\bar{b} = a/2\ [1\bar{1}0]$) inclined at 45° to the interface and the dislocation line along [001]; and (2) a (110) interface with $\bar{b} = a/2\ [1\bar{1}0]$ lying in the interface and the dislocation line along [001]. The following values of the parameters will be used for the calculations.

$$c = 1/2(a_1 + a_2) = 3.59 \text{Å}$$

$$\delta = 0.8\%$$

$$\nu_1 = \nu_2 = 1/3$$

$$\mu_1 = 8.3 \times 10^{11} \text{ dyn/cm}^2$$

$$\mu_2 = 6.3 \times 10^{11} \text{ dyn/cm}^2$$

$$\mu = 1/2(u_1 + u_2) = 7.3 \times 10^{11} \text{ dyn/cm}^2$$

$$\Omega = 5.4 \times 10^{11} \text{ dyn/cm}^2$$

$$\beta = 3.7 \times 10^{-2}$$

Substituting these values into Eq. (2), one calculates for the (100) interface that $E_{\text{struct}}^{\text{semi-coh}} = 85$ ergs/cm^2. This value probably underestimates the actual energy because the equation derived by van der Merwe is for the case of parallel pure edge dislocations with Burgers vector equal to the lattice parameter whereas the observed interfacial dislocations have a resolved edge component lying in the interface equal to one-half the lattice parameter. Consequently, a greater number of these inefficient dislocations are required to completely accommodate the misfit at the interface. If only one set of dislocations is present at the interface, then the misfit in the orthogonal cube direction is still accommodated by elastic strain and the total structural interfacial energy for this case is $E_{\text{struct}}^{\text{semi-coh}}$ (100) $\simeq$ 85 ergs/cm^2 + 165 ergs/cm^2 = 250 ergs/cm^2.

For the second type of semi-coherent interface parallel to (110), a fewer number of misfit dislocations are required compared to the (100) interface since the Burgers vector lies in the interface and the dislocations are pure edge in character. The equilibrium separation between misfit dislocations is given by the Brooks formula (see Eq. (5)); and if

the interface changes its orientation from (100) to (110) then this distance is increased by the factor $\sqrt{2}$ with a corresponding reduction in the dislocation density and the structural interacial energy. The fact that the (110) interface has a lower energy than the (100) interface also follows from Eq. (2) used to calculate the semi-coherent interfacial energy. The reference lattice parameter, c, in this equation corresponds to the atomic distance along the misfit direction. For the (110) interface this misfit direction is $[1\bar{1}0]$ with $a_{\langle 110 \rangle} = |\bar{b}| = 2.54$Å. Using this value of c in Eq. (2), one obtains $E_{struct}^{semi-coh}$ (110) = 60 ergs/cm^2; and if only one set of dislocations is present at the interface, then the total structural interfacial energy for this case is $E_{struct}^{semi-coh}$ (110) $\simeq$ 225 ergs/cm^2. As more interfacial dislocations with other Burgers vectors to accommodate the misfit develop at the interface, the structural interfacial energy will be reduced further.

APPENDIX B: RESOLUTION OF COHERENCY STRESSES
ACTING ON GLIDE DISLOCATIONS

The following discussion and stress analysis are based on an analysis done by Dahlgen[62] for the calculated yield stress of a coherent platelet microstructure. As an approximation to the coherency stresses acting on the platelets, it will be assumed that the stress normal to the interface is zero, $\sigma_{zz} = 0$ (see Fig. 20), since the total displacement across many platelets is small and that the two stresses parallel to the interface are equal, $\sigma_{xx} = \sigma_{yy}$, since the two phases are tetragonal. Because the four-fold symmetry axis of the tetragonal structure is taken normal to the x-y plane, $\sigma_{xy} = 0$. The other two shear stresses, σ_{yz} and σ_{xz}, are not zero, but for thin platelets these stresses are small. If the platelet thickness is much less than its length, then these shear stresses can be neglected.

For an isotropic material

$$\epsilon_{xx} = \frac{1}{E} \{\sigma_{xx} - \nu(\sigma_{yy} + \sigma_{zz})\}$$

where E is Young's modulus and ν is Poisson's ratio. Since it is being assumed that $\sigma_{xx} = \sigma_{yy}$ and $\sigma_{zz} = 0$ this equation gives

$$\epsilon_{xx} = \frac{1}{E} (\sigma_{xx} - \nu\sigma_{xx})$$

and

$$\sigma_{xx} = \frac{E}{1-\nu} \epsilon_{xx}$$

where the cohernecy strain is $\epsilon_{xx} = (\bar{a} - a_{io})/a_{io}$, $\bar{a}$ being the common non-equilibrium lattice parameter ($\bar{a} \simeq 1/2(a_{1o} + a_{2o})$) and a_{io} being the appropriate equilibrium cubic lattice parameter of the ith phase. This elastic coherency strain has a smaller value than the previously defined

misfit strain, $\delta' = (a_1 - a_2)/a_1$, for the equilibrium misfit dislocation structure; and as an approximation $\varepsilon_{xx} \simeq 1/2 \ \delta = 0.4\%$ for these Cu-Ni-Fe alloys.[58] Taking $\nu = 1/3$, $E = 2 \times 10^4$ kg/mm^2 and $\varepsilon_{xx} = 0.004$, the corresponding value of the coherency stress is

$$\sigma_{xx} = \sigma_{yy} \simeq 120 \text{ kg/mm}^2$$

The Ni-Fe rich phase, with a smaller equilibrium lattice parameter, is acted on by a tensile stress and the Cu rich phase by a compressive stress.

The interaction between the coherency stresses and the slip dislocations is found by resolving the shear components of these stresses on the slip plane and in the slip direction. For fcc crystals the slip planes are {111} and the slip directions are ⟨110⟩. The stress resolution can be done using the stress tensor and the following formula:

$$\sigma_{\mu\rho} = \sum_{i,j} \sigma_{ij} \ l_{i\mu} \ l_{j\rho}$$

where $\sigma_{\mu\rho}$ is the resolved stress acting in the ρ direction on the slip plane with normal μ and $l_{i\mu}$ and $l_{j\mu}$ are direction cosines between the given directions. Table II gives these resolved shear stresses for the case of a (001) interface and all possible Burgers vectors. The normals to the slip planes all point in the positive z direction to give consistent results.

ACKNOWLEDGEMENTS

REFERENCES

1. The Scientific Papers of J. Willard Gibbs, p. 105. Dover (1961).

2. J. W. Cahn, Trans. AIME 242, 166 (1968).

3. J. E. Hilliard in Phase Transformations, p. 497. Amer. Soc. for Metals (1970).

4. D. de Fontaine in Ultrafine-Grain Metals, p. 93. Syracuse Univ. Press (1970).

5. M. Hillert, Acta Met. 9, 525 (1961).

6. J. W. Cahn, Acta Met. 9, 795 (1961).

7. J. W. Cahn, Acta Met. 10, 179 (1962).

8. J. W. Cahn and J. E. Hilliard, J. Chem. Phys. 28, 258 (1958).

9. J. W. Cahn and J. E. Hilliard, J. Chem. Phys. 31, 688 (1959).

10. J. P. Hirth, W. A. Tiller and G. M. Pound, Phil. Mag. 22, 117 (1970).

11. W. A. Tiller, G. M. Pound and J. P. Hirth, Acta Met. 18, 225 (1970).

12. J. W. Morris, Jr., Phil. Mag. 23, 1041 (1971).

13. J. W. Cahn and J. E. Hilliard, Acta Met. 19, 151 (1971).

14. H. E. Cook, D. de Fontaine and J. E. Hilliard, Acta Met. 17, 765 (1969).

15. H. E. Cook and D. de Fontaine, Acta Met. 17, 915 (1969).

16. H. E. Cook and D. de Fontaine, Acta Met. 19, 607 (1971).

17. J. W. Cahn, Acta Met. 14, 1685 (1966).

18. A. Nagarajan and P. A. Flinn, Appl. Phys. Lett. 11, 120 (1967).

19. L. H. Bennett and L. J. Swartzendruber, Acta Met. 18, 485 (1970).

20. D. Chandra and L. H. Schwartz, Metall. Trans. 2, 511 (1971).

21. T. De Nys and P. M. Gielen, Metall. Trans. 2, 1423 (1971).

22. K. B. Rundman and J. E. Hilliard, Acta Met. 15, 1025 (1967).

23. M. Murakami, O. Kawano, Y. Murakami and M. Morinaga, Acta Met. 17, 1517 (1969).

24. E. P. Butler and G. Thomas, Acta Met. 18, 347 (1970).

25. R. J. Livak and G. Thomas, Acta Met. 19, 497 (1971).

26. R. J. Livak, unpublished research.

27. A. J. Bradley, Proc. Phys. Soc. 52, 80 (1940).

28. V. Daniel and H. Lipson, Proc. Roy. Soc. London 181A, 368 (1943).

29. V. Daniel and H. Lipson, Proc. Roy. Soc. London 182A, 378 (1944).

30. M. E. Hargreaves, Acta Cryst. 4, 301 (1951).

31. A. Guinier, Solid State Phys. (Advances in Research and Applications) 9, 293 (1959).

32. D. de Fontaine, in Local Atomic Arrangements Studied by X-Ray Diffraction, p. 51. Gordon and Breach (1966).

33. H. E. Cook, Acta Met. 18, 297 (1970).

34. V. A. Phillips, in Institute of Metals Monograph No. 33 of Conf. on Mechanisms of Phase Transformations in Crystalline Solids, p. 11, Manchester (1968).

35. W. G. Dorfeld and V. A. Phillips, Acta Met. 18, 955 (1970).

36. E. L. Huston, J. W. Cahn and J. E. Hilliard, Acta Met. 14, 1053 (1966).

37. F. A. Badia, G. N. Kirby and J. R. Mihalisin, Trans. ASM 60, 395 (1967).

38. J. E. Morral and J. W. Cahn, Acta Met. 19, 1037 (1971).

39. M. Bouchard and G. Thomas, in Proc. of 29th Annual Electron Microscopy Society of America Meeting, p. 126. Claitor's Publishing Div. (1971).

40. M. V. Dzhibuti and Yu. D. Tyapkin, Soviet Physics - Crystallography 13, 240 (1968).

41. Yu. D. Tiapkin and M. V. Jibuti, Acta Met. 19, 365 (1971).

42. H. Gaye and C. H. P. Lupis, Trans. AIME 245, 2543 (1969).

43. V. A. Phillips, Trans. AIME 230, 967 (1964).

44. A. J. Ardell, R. B. Nicholson and J. D. Eshelby, Acta Met. 14, 1295 (1966).

45. V. A. Phillips, Acta Met. 14, 1533 (1966).

46. M. Hillert, M. Cohen and B. L. Averbach, Acta Met. 9, 536 (1961).

47. T. J. Tiedema, J. Bouman and W. G. Burgers, Acta Met. 5, 310 (1957).

48. L. J. van der Toorn, Acta Met. 8, 715 (1960).

49. R. W. Carpenter, Acta Met. 15, pp. 1297 and 1567, (1967).

50. J. Weise and V. Gerold, Z. Metallkunde, 59, 904 (1968).

51. G. Kralik, J. Weise and V. Gerold, in Institute of Metals Monograph No. 33 of Conf. on Mechanisms of Phase Transformations in Crystalline Solids, p. 27, Manchester (1968).

52. A. J. Ardell, K. Nutall and R. B. Nicholson, in Institute of Metals Monograph No. 33 of Conf. on Mechanisms of Phase Transformations in Crystalline Solids, p. 22. Manchester (1968).

53. R. D. Jones and K. G. Thomas, Phil. Mag. 22, 427 (1970).

54. R. Gibala, Trans. AIME 230, 255 (1964).

55. J. E. Woodilla, Jr., and B. L. Averbach, Acta Met. 16, 255 (1968).

56. W. Köster and W. Dannöhl, Z. Metallkunde 27, 220 (1935).

57. A. J. Bradley, W. F. Cox and H. J. Goldschmidt, J. Inst. Metals 67, 189 (1941).

58. E. P. Butler, University of California, Lawrence Berkeley Laboratory Report UCRL-18840, June 1969.

59. H. E. Cook and J. E. Hilliard, Trans. AIME 233, 142 (1965).

60. E. P. Butler, Metal Sci. Jour. 5, 8 (1971).

61. R. J. Livak, M. S. Thesis, University of California, Berkeley, UCRL-19189, March 1970.

62. S. D. Dahlgren, Ph. D. Thesis, University of California, Berkeley, UCRL-16846, May 1966.

63. A. G. Khachaturyan, Phys. Status Solidi 35, 119 (1969).

64. M. Bouchard, R. J. Livak and G. Thomas, Surface Science 31, 275 (1972).

65. R. Cadoret and P. Delavignette, Phys. Status Solidi 32, 853 (1969).

66. P. B. Hirsch, A. Howie, R. B. Nicholson, D. W. Pashley and M. J. Whelan, Electron Microscopy of Thin Crystals, p. 340. Butterworth (1965).

67. J. M. Oblak and B. H. Kear, Trans. ASM 61, 519 (1968).

68. A. J. Ardell, Phil. Mag. 16, 147 (1967).

69. F. C. Frank and J. H. van der Merwe, Proc. Roy. Soc. London 198A, 205 (1949).

70. F. C. Frank and J. H. van der Merwe, ibid., 216.

71. J. H. van der Merwe, Proc. Phys. Soc. 63A, 616 (1950).

72. H. Brooks, in Metal Interfaces, p. 20. Amer. Soc. for Metals (1952).

73. H. I. Aaronson, C. Laird and K. R. Kinsman, in Phase Transformations, p. 339. Amer. Soc. for Metals (1970).

74. J. W. Matthews, Phil. Mag. 13, 1207 (1966).

75. W. A. Jesser and J. W. Matthews, Phil. Mag. 15, 1097 (1967).

76. W. A. Jesser and J. W. Matthews, Phil. Mag. 17, 595 (1968).

77. W. A. Jesser and J. W. Matthews, Phil. Mag. 17, 461 (1968).

78. W. A. Jesser and J. W. Matthews, Phil. Mag. 17, 475 (1968).

79. E. Levine, J. Washburn and G. Thomas, J. Appl. Phys. 38, 81 (1967).

80. G. C. Weatherly and R. B. Nicholson, Phil. Mag. 17, 801 (1968).

81. K. R. Kinsman and H. I. Aaronson, "Structure of Crystalline Interfaces" to be published in the book Theory of Microstructure from a Seminar held Sept. 1971. International Microstructure Analysis Society (IMS), Denver, Colorado.

82. J. H. van der Merwe, J. Appl. Phys. 34, 117 (1963).

83. J. H. van der Merwe, ibid., 123.

84. G. C. Weatherly, Phil. Mag. 17, 791 (1968).

85. L. M. Brown, G. R. Woolhouse and A. Valdrè, Phil. Mag. 17, 781 (1968).

86. D. de Fontaine, Acta Met. 17, 477 (1969).

87. J. W. Matthews, Scripta Met. 5, 1056 (1971).

88. J. Bardeen and C. Herring, in Imperfections in Nearly Perfect Crystals, p. 261. Wiley (1952).

89. J. Weertman, Phys. Rev. 107, 1259 (1957).

90. J. Weertman, Trans. AIME 227, 1439 (1963).

91. R. de Wit, ibid., 1443.

92. J. P. Hirth and J. Lothe, Theory of Dislocations, p. 569. McGraw-Hill (1968).

93. F. Seitz, Phys. Rev. 79, 1002 (1950).

94. J. D. Boyd and R. B. Nicholson, Acta Met. 19, 1379 (1971).

95. J. S. Koehler, Phys. Rev. B 2, 547 (1970).

96. B. J. Shaw, Acta Met. 15, 1169 (1967).

97. H. E. Cline and D. F. Stein, Trans. AIME 245, 841 (1969).

98. H. E. Cline and D. Lee, Acta Met. 18, 315 (1970).

99. R. M. Brick, R. B. Gordon and A. Phillips, Structure and Properties of Alloys, p. 150. McGraw-Hill (1965).

100. A. K. Mukherjee, J. D. Mote and J. E. Dorn, Trans. AIME 233, 1559 (1965).

101. G. Saada, Acta Met. 8, 200 (1960).

102. R. J. Livak and W. W. Gerberich, in Proc. of the Fifth International Materials Symposium, p. 647, University of California, Berkeley (1971).

103. A. H. Geisler and J. B. Newkirk, Trans. AIME 180, 101 (1949).

104. A. H. Geisler, Trans. ASM 43, 70 (1951).

105. A. H. Geisler, Trans. AIME 180, 230 (1949).

106. H. I. Aaronson and J. B. Clark, Acta Met. 16, 845 (1968).

107. U. K. Malhotra and K. B. Rundman, Metall. Trans. 3, 1521 (1972).

108. V. Gerold, Phys. Status Solidi 1, 37 (1961).

109. A. F. Bonfiglioli and A. Guinier, Acta Met. 14, 1213 (1966).

110. W. W. Gerberich, V. F. Zackay, E. R. Parker and D. Porter, in Ultrafine-Grain Metals, p. 259. Syracuse University Press (1970).

111. H. J. Saxton, A. J. West and C. R. Barrett, Metall. Trans. 2, 999 (1971).

112. A. J. West, H. J. Saxton, A. S. Tetelman and C. R. Barrett, Metall. Trans. 2, 1009 (1971).

Table I. Diffraction conditions for dislocation contrast ($\bar{g}\cdot\bar{b}$ products)

Reflection ($\bar{g}$)

		11Ī	02\bar{2}	Ī1Ī	200	13Ī	Ī3Ī	11Ī	3ĪĪ	2̄20	31Ī	13Ī
	⟨100⟩	X	O	X	X	X	X	X	X	X	X	X
	⟨010⟩	X	X	X	O	X	X	X	X	X	X	X
Burgers ⟨001⟩		X	X	X	O	X	X	X	X	O	X	X
vector ⟨110⟩		X	X	O	X	X	X	X	X	O	X	X
($\bar{b}$) ⟨Ī10⟩		O	X	X	X	X	X	O	X	X	X	X
	⟨101⟩	O	X	X	X	O	X	O	X	X	X	O
	⟨Ī01⟩	X	X	O	X	X	O	X	X	X	X	X
	⟨011⟩	O	O	O	O	X	X	O	X	X	O	X
	⟨0Ī1⟩	X	X	X	O	X	X	X	O	X	X	X

(011) zone   (013) zone   (112) zone   (114) zone

For $\bar{g}\cdot\bar{b} = 0$ then dislocation will be out of contrast.

For $\bar{g}\cdot\bar{b} = X$ dislocations will be in contrast.

XBL 718-7174

Table II: Stress interaction between (001) coherent interface and Burgers vectors of slip dislocations.

Burgers Vector	Slip Plane	Resolved Shear Stress
$\pm[110]$	$(\bar{1}11)$ $(1\bar{1}1)$	0
$\pm[\bar{1}10]$	(111) $(\bar{1}\bar{1}1)$	0
$[101]$	$(\bar{1}11)$ $(\bar{1}\bar{1}1)$	$-\sigma_r$
$[\bar{1}0\bar{1}]$	$(\bar{1}11)$ $(\bar{1}\bar{1}1)$	$+\sigma_r$
$[\bar{1}01]$	(111) $(1\bar{1}1)$	$-\sigma_r$
$[10\bar{1}]$	(111) $(1\bar{1}1)$	$+\sigma_r$
$[011]$	$(1\bar{1}1)$ $(\bar{1}\bar{1}1)$	$-\sigma_r$
$[0\bar{1}\bar{1}]$	$(1\bar{1}1)$ $(\bar{1}\bar{1}1)$	$+\sigma_r$
$[0\bar{1}1]$	(111) $(\bar{1}11)$	$-\sigma_r$
$[01\bar{1}]$	(111) $(\bar{1}11)$	$+\sigma_r$

$$\sigma_r = \sigma_{xx}/\sqrt{6} = 50 \text{ kg/mm}^2$$

The plus (+) means attraction and the minus (-) means repulsion for the interface of the phase under a tensile stress (i.e. the Ni-Fe rich phase with $c_1 < a$).

Table III. Microstructural changes during
aging at 800°C and 775°C.

Aging Time	Wavelength (λ)	Interface	Δa
800°C			
1 hr	500Å	Coherent	~0.8%
10 hrs	1600Å	Coherent	"
100 hrs	2200Å	Coherent	"
1000 hrs	--	Semi-Coherent	"
775°C			
10 hrs	1000Å	Coherent	~0.8%
100 hrs	2000Å	Coherent	"
200 hrs	> ~2300Å	Losing Coherency	"

Table IV. Experimental data for 35 mils thick tensile specimens aged at 800°C.

Aging Time (hours)	Yield Stress (kg/mm^2)	Ultimate Tensile Strength (kg/mm^2)	Total Elongation	Reduction of Area	$d\sigma/d\varepsilon$ at 1% ε (kg/mm^2)	$d\sigma/d\varepsilon$ at 2% ε (kg/mm^2)	$d\sigma/d\varepsilon$ at 5% ε (kg/mm^2)	$d\sigma/d\varepsilon$ at 10% ε (kg/mm^2)
As Quenched (Ref. 61)	13.3±0.7	---	30.6%	---	---	148	---	---
1	24.2±1.02	45.4	10.2%	7.8%	235	194±12.1	154±1.3	106
10	21.1±0.63	46.4	12.8%	10.8%	264±11.9	221±5.0	158±1.7	114
100	20.3±0.64	53.7	17.0%	17.6%	327±24.7	243±11.1	164±2.1	100
1000	19.6±0.90	58.0	22.5%	34.3%	180±5.3	145±6.2	105±3.4	80

Table V. Experimental data for tensile specimens aged at 775°C.

Aging Time (hours)	Yield Stress (kg/mm²)	Ultimate Tensile Strength (kg/mm²)	Total Elongation	Reduction of Area	$d\sigma/d\varepsilon$ at 1% ε (kg/mm²)	$d\sigma/d\varepsilon$ at 2% ε (kg/mm²)	$d\sigma/d\varepsilon$ at 5% ε (kg/mm²)
35 Mils Thick							
10	24.4±0.49	50.7	12.5%	13.3%	338±8.1	254±10.0	157±13.0
100	22.2±0.33	64.2	19.2%	28.0%	378±8.4	255±4.5	150±9.8
200	23.7±0.32	61.4	19.4%	25.4%	353±6.8	242±5.0	153±5.5
12 Mils Thick							
10	24.8±0.29	54.7	15.2%	11.0%	369	273	165
100	22.9±0.28	54.3	16.8%	14.2%	404	262	150
200	24.6±0.20	52.6	18.2%	11.8%	361	241	148

FIGURE CAPTIONS

Fig. 1. Transmission electron micrographs of alloy 2 aged at 625°C for

(a) 6 min $\lambda \sim 75$ Å, (b) 10 hrs $\lambda \sim 135$Å and (c) 1000 hrs

$\lambda \sim 900$Å showing the development of the planar, coherent interfaces.

Fig. 2. The pseudo-binary section along the tie-line of the Cu-Ni-Fe

system used for this study showing the three alloy compositions.

The chemical spinodal was calculated by Butler[58] using $T_c \simeq 825$°C

and $C_c = 0.50$.

Fig. 3. Electron diffraction pattern (a) and corresponding bright field

image (b) showing splitting of the 600 reflection due to the

tetragonal structure of coherent particles in alloy 2 aged 1000 hrs

at 625°C

Fig. 4. Electron diffraction pattern (a) and corresponding bright field

image (b) showing split streaks at the $51\bar{1}$ reflection that are

normal to coherent platelets in alloy 2 aged 100 hrs at 800°C.

Fig. 5. (a) Transmission electron micrograph showing coherent platelets

about 500Å thick and 1-2 μm long in a foil of alloy 2 aged

100 hrs at 800°C. (b) Micrograph taken of the same grain showing

some particles losing coherency. Note rotation of semi-coherent

interface in the upper left corner. Electron beam parallel

to [011] zone axis.

Fig. 6. Bright field micrograph of alloy 2 aged 100 hrs at 800°C showing

a dislocation configuration suggestive of a spiraling mechanism

for the formation of interfacial dislocations. Note local

rotation of interface at dislocation lines.

Fig. 7. Electron micrograph of the symmetrical alloy aged 100 hrs at 775°C showing a corrugated semi-coherent microstructure resulting from rotation of the interfaces toward {110} planes. Electron beam parallel to [011] zone axis.

Fig. 8. Bright field micrographs of the same area under different diffraction conditions of alloy 1 aged 100 hrs at 775°C showing alternating groups of dislocations on the stepped interface to the right. The foil orientation was [011] zone axis and the possible Burgers vectors in (a) are a/2 [$\bar{1}$10] or a/2 [101] and in (b) are a/2 [110] or a/2 [$\bar{1}$01]

Fig. 9. Bright field micrographs of the same area under different diffraction conditions of alloy 2 aged 200 hrs at 775°C. The foil orientation was [013] zone axis; and thus the interfaces in which the dislocations lie are near the (001) plane. The dislocations visible in (a) have Burgers vector a/2 [$\bar{1}$01], whereas the dislocations seen in (b) have $\bar{b}$ = a/2 [011] or a/2 [0$\bar{1}$1].

Fig. 10. Electron micrograph of alloy 2 aged 100 hrs at 800°C showing interfacial dislocations around the center particle that cannot have a Burgers vector lying in the interface since $\bar{g}$ 200 is normal to the interface and the dislocations are visible.

Fig. 11. Bright field micrograph of alloy 2 aged 100 hrs at 800°C showing some interfacial dislocations that do not lie along ⟨ 001⟩ (see arrows). Also note the unequal number of dislocations at the two interfaces.

Fig. 12. Electron micrograph of alloy 2 aged 200 hrs at 775°C showing dislocations near and at the interfaces lying in ⟨110⟩ directions. The foil orientation was [011] zone axis.

Fig. 13. Bright field micrographs of the same area under different diffraction conditions of alloy 2 aged 200 hrs at 775°C. The dislocations visible in (a) have $\bar{b}$ = a/2 [110] or a/2 [$\bar{1}$01] whereas those visible in (b) have $\bar{b}$ = a/2 [0$\bar{1}$1] and appear to be rotating so as to lie along [100].

Fig. 14. Bright field micrographs of the same area under different diffraction conditions of the symmetrical alloy aged 100 hrs at 775°C showing dislocations visible in (b) that lie at steps on the interfaces visible in (a). When (a) is viewed in stereo the steps are evident.

Fig. 15. Stereo micrographs of alloy 2 aged 100 hrs at 800°C showing some dislocations (see arrows) that are inclined to the parallel interfacial dislocations and in some cases appear to be connected to them. Note: To obtain a stereo image, stereo glasses should be placed approximately 5 in. above and centered on the micrographs. The glasses may then be slightly rotated until the two black dots and the dislocation images are superimposed.

Fig. 16. High voltage (650 keV) electron micrograph of alloy 2 aged 100 hrs at 800°C showing a dislocation being extended along the interface and looping back upon itself (see arrow).

Fig. 17. Bright field micrograph of symmetrical alloy aged 100 hrs at 775°C showing interfacial dislocations looping around the platelets.

Fig. 18. Bright field micrographs of the same area under different diffraction conditions showing moiré patterns and interfacial dislocations.- Alloy 2 aged 200 hrs at 775°C.

Fig. 19. Electron micrograph of symmetrical alloy aged 100 hrs at 775°C showing preferential loss of coherency along a grain boundary.

Fig. 20. Schematic drawing of coherent platelet microstructure used in calculating the interfacial energies and also for the resolution of the coherency stresses on the various slip systems.

Fig. 21. Schematic drawing of a parallel array of edge dislocations at an interphase interface considered by van der Merwe[82,83] in calculating the structural interfacial energy.

Fig. 22. Plane section through the platelet microstructure parallel to the ($\bar{1}$11) slip plane showing the stress activated extension of a slip dislocation along the coherent interface.

Fig. 23. Proposed mechanism for the spiraling of a captured slip dislocation around a coherent platelet to form misfit-accommodating dislocation loops. Refer to Part III for discussion.

Fig. 24. Schematic drawing showing the similarity between a spiral dislocation and a series of dislocation loops intersected by a dislocation line.

Fig. 25. Drawing of flat tensile specimens used in this study.

Fig. 26. Transmission electron micrographs showing the lamellar micro-structure of tensile specimens (alloy 2) aged at 775°C for (a) 10 hrs $\lambda \sim 1000$Å, (b) 100 hrs $\lambda \sim 2000$Å and (c) 200 hrs $\lambda > 2300$Å.

Fig. 27. Bright field micrographs of the same area under different diffraction conditions of alloy 2 aged 1000 hrs at 800°C showing the different sets of interfacial dislocations. Refer to Table I for the possible Burgers vectors for each set of dislocations.

Fig. 28. Electron micrograph of alloy 2 aged 1000 hrs at 800°C showing the change in particle morphology for the semi-coherent microstructure.

Fig. 29. Optical micrographs of a 12 mils thick tensile specimen aged 100 hrs at 775°C showing the discontinuous grain boundary reaction. Magnification (a) 225×; (b) 675×.

Fig. 30. Optical micrographs taken of the same area of a 12 mils thick tensile specimen aged 200 at 775°C showing grain boundary precipitates. Magnification (a) 220×; (b) 665×.

Fig. 31. Optical micrographs of 35 mils thick tensile specimens aged at 775°C for (a) 100 hrs and (b) 200 hrs (475×).

Fig. 32. Optical micrographs showing grain boundary precipitates in 35 mils thick tensile specimens aged at 800°C for (a) 10 hrs and (b) 100 hrs. Magnification (a) 1460×; (b) 390×.

Fig. 33. Optical micrographs of 35 mils thick tensile specimens aged 1000 hrs at 800°C showing the Widmanstätten structure and grain boundary precipitation (390×).

Fig. 34. Plot of yield stress at 0.2% offset and total elongation to failure vs aging time for tensile specimens aged at 800°C. Data for as quenched samples taken from Ref. 61.

Fig. 35. Plot of yield stress at 0.2% offset vs aging time for 35 mils thick tensile specimens aged at 775°C.

Fig. 36. Plot of total elongation to failure vs aging time for 12 mils thick tensile specimens aged at 775°C.

Fig. 37. Plot of work hardening rates at 1%, 2% and 5% plastic strain vs aging time for specimens aged at 800°C.

Fig. 38. Plot of work hardening rates at 1%, 2% and 5% plastic strain vs aging time for 35 mils thick specimens aged at 775°C.

Fig. 39. Plot of work hardening rates at 1%, 2% and 5% plastic strain vs aging time for 12 mils thick specimens aged at 775°C.

Fig. 40. Stress-strain curves up to 5% strain for 35 mils thick tensile specimens aged at 775°C for (a) 10 hrs, (b) 100 hrs and (c) 200 hrs and at 800°C for (d) 1 hr, (e) 10 hr, (f) 100 hrs and (g) 1000 hrs.

Fig. 41. Transmission electron micrographs of tensile specimens aged at 775°C for (a) 100 hrs and (b) 200 hrs and strained 5%. In micrograph (b) note the dislocations at the coherent interfaces (see arrow).

Fig. 42. Three bright field micrographs of the same area under different diffraction conditions showing the interaction between slip dislocations and the parallel interfacial dislocations. See Part IV for discussion. Alloy 2 aged 200 hrs at 775°C and strained 5%.

Fig. 43. Electron micrographs of a tensile specimen aged 100 hrs at 800 °C and pulled to failure (~17% ε) showing sheared platelets and heavy slip bands along ⟨110⟩.

Fig. 44. Electron micrograph of a tensile specimen aged 100 hrs at 800°C and pulled to failure showing dense dislocation tangles that formed at the coherent interfaces (see arrows). The foil orientation was [001] zone axis and thus one variant of the platelet morphology was lying in the plane of the foil.

Fig. 45. Drawing of WOL fracture toughness specimens used in this study.

Fig. 46. Plot of stress intensity to initiate crack propagation and yield stress vs (grain diameter)$^{-1/2}$ showing the linear dependence of these two parameters on $d^{-1/2}$.

Fig. 47. Scanning electron fractograph of the small grain fracture specimen showing the ductile nature of the fracture. The ledges appear to be grain boundaries.

Fig. 48. Scanning electron fractograph of the large grain size fracture specimen showing the intergranular fracture.

Fig. 49. (a) Dark field electron micrograph of alloy 2 aged 10 hrs at 700°C showing enhanced coarsening of the spinodal microstructure at the grain boundary.
(b) Bright field electron micrograph of alloy 2 aged 10 hrs at 775°C showing grain boundary precipitates of the minor (Ni-Fe rich) phase.

Fig. 50. Scanning electron fractographs of the same area of a 35 mils thick tensile specimen aged 10 hrs at 775°C showing the partially integranular fracture. Magnification (a) 225x; (b) 560×.

XBB 708-3704

Fig. 1

XBL 693-293

Fig. 2.

XBB 729-4748

Fig. 3

g 51$\bar{1}$

XBB 729-4745

Fig. 4

(100)

0.5 μm
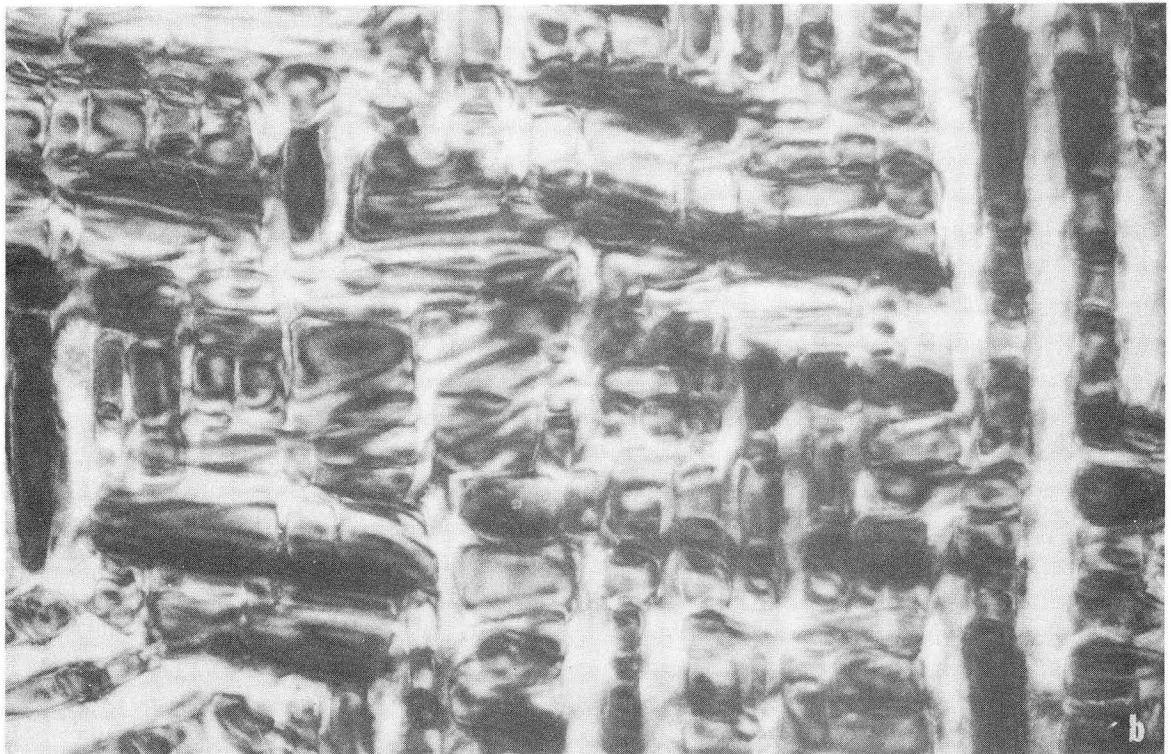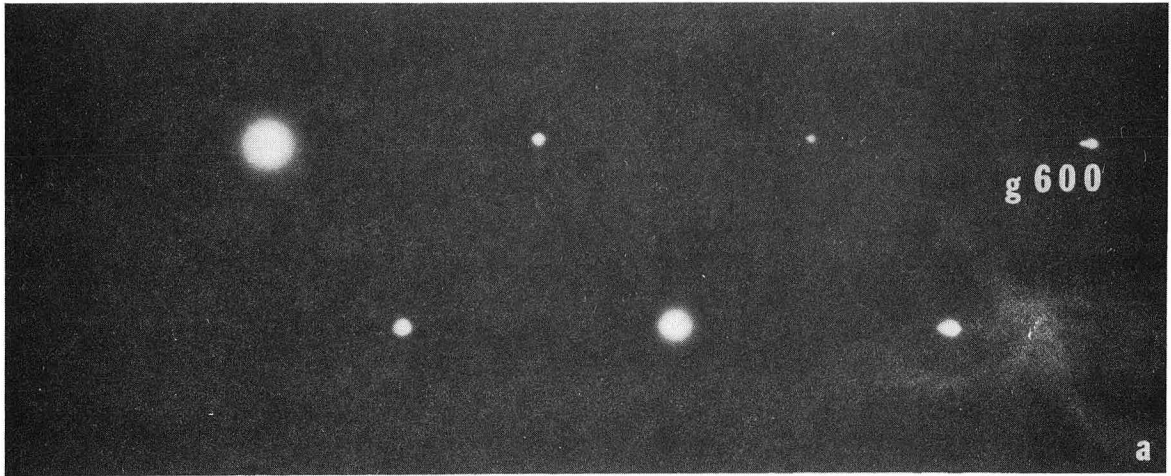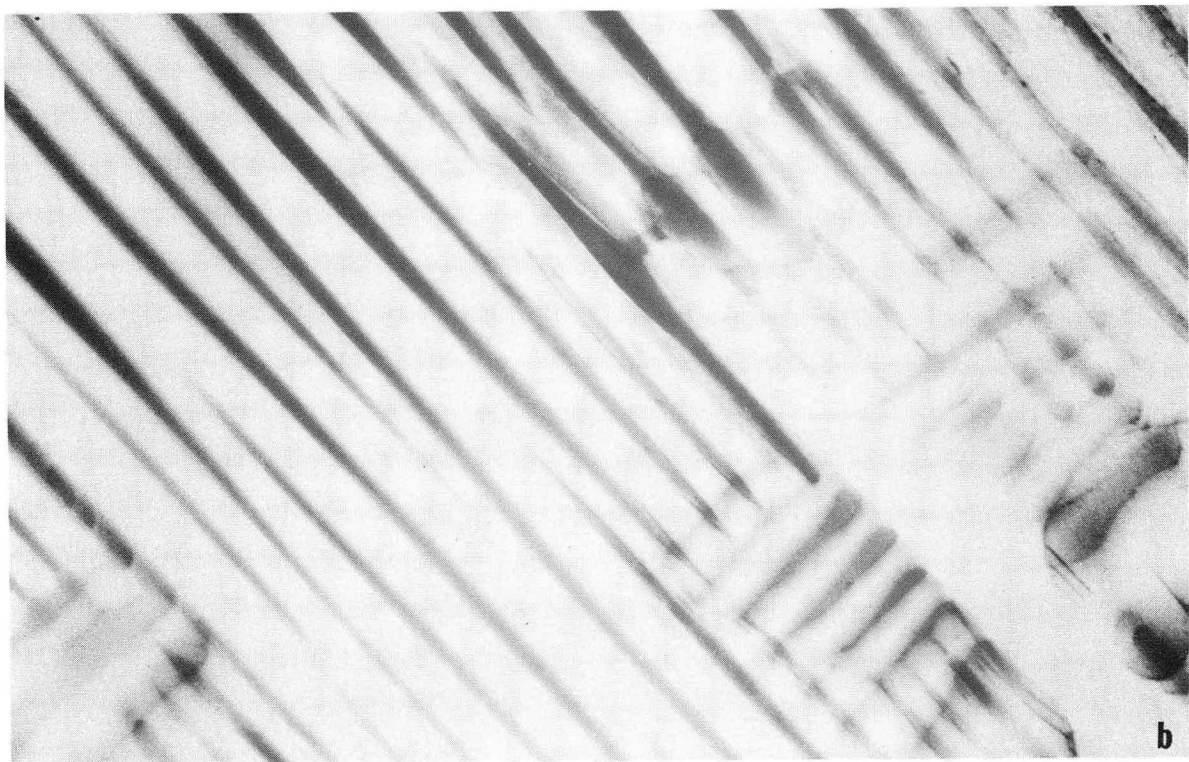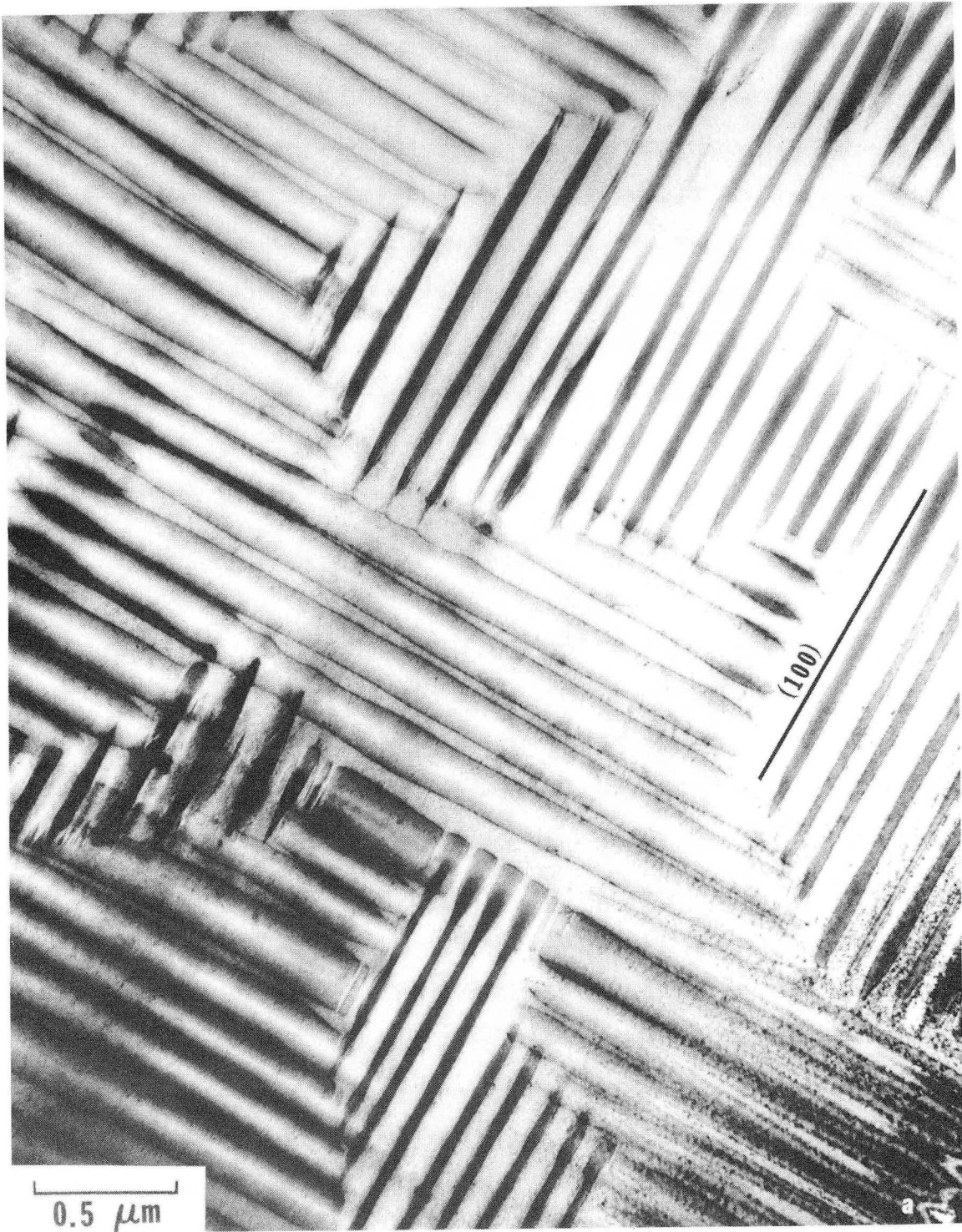
XBB 729-4744

Fig. 5a
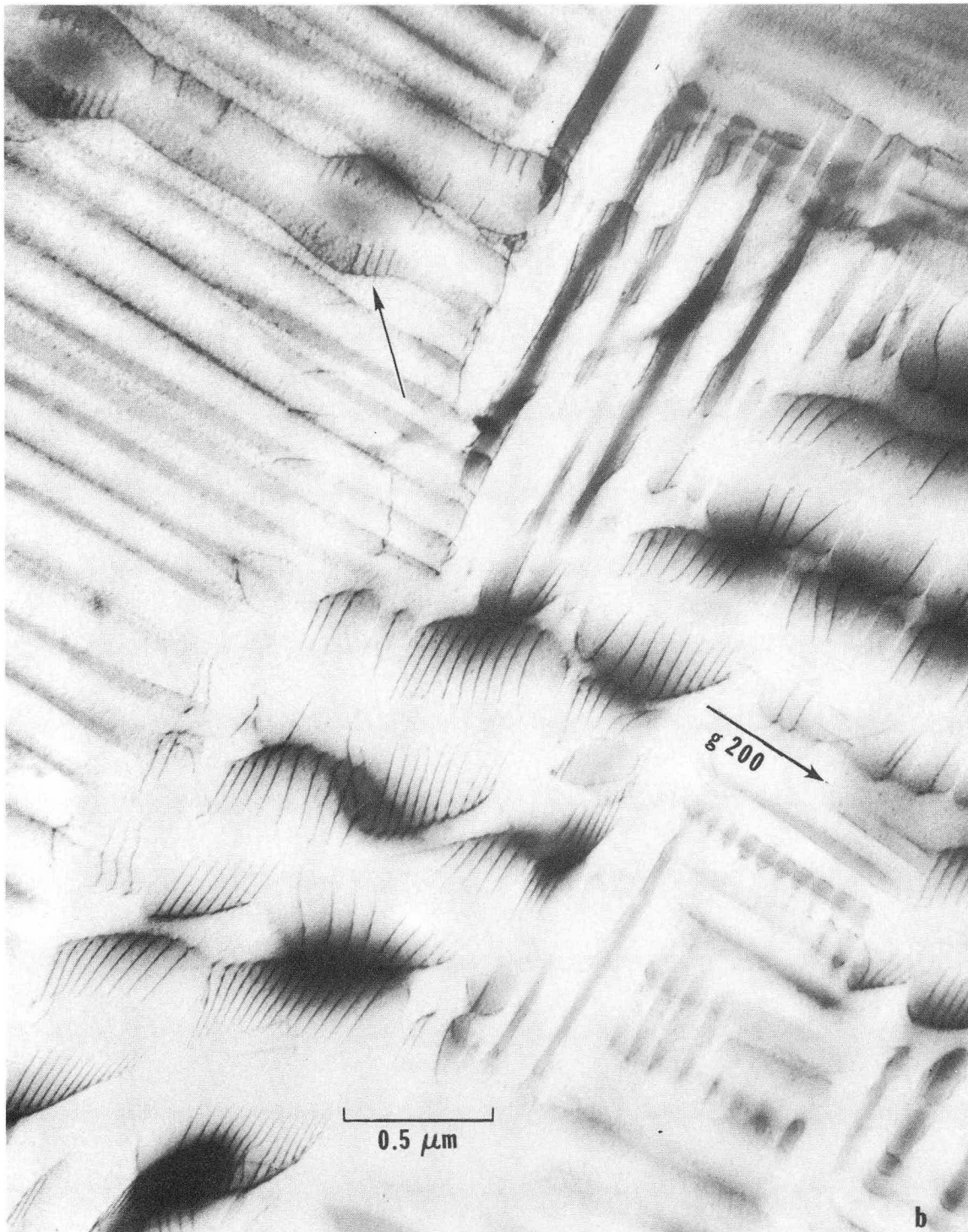
XBB 729-4742

Fig. 5b

XBB 729-4726

Fig. 6

0.3 μm

(110)

(Ī10)
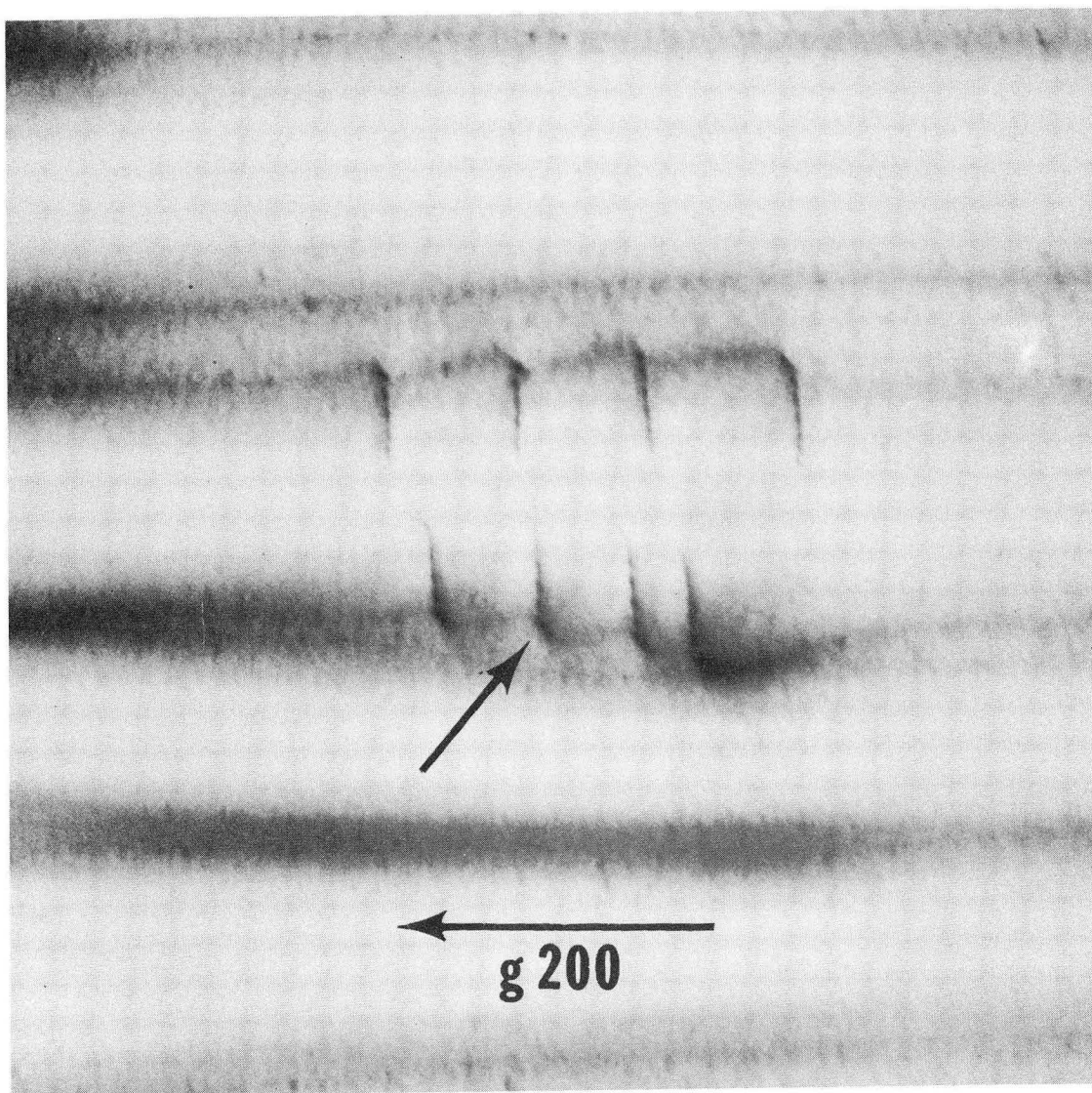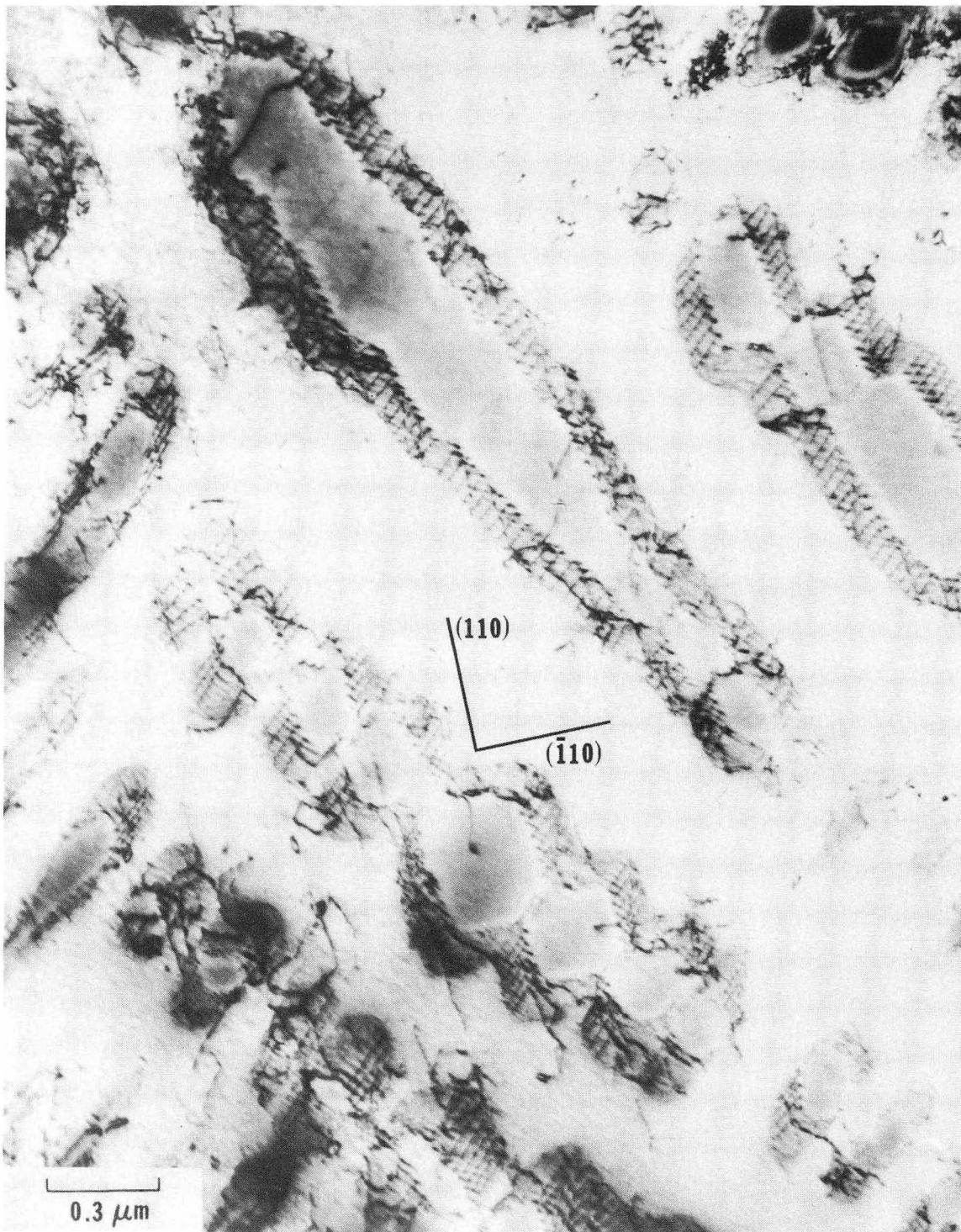
XBB 729-4743

Fig. 7

XBB 718-3733

Fig. 8

0.3 μ

XBB 729-4747

Fig. 9

g200

XBB 729-4731

Fig. 10

001

g 200

0.3 μm

XBB 729-4730

Fig. 11

0.3μm

110
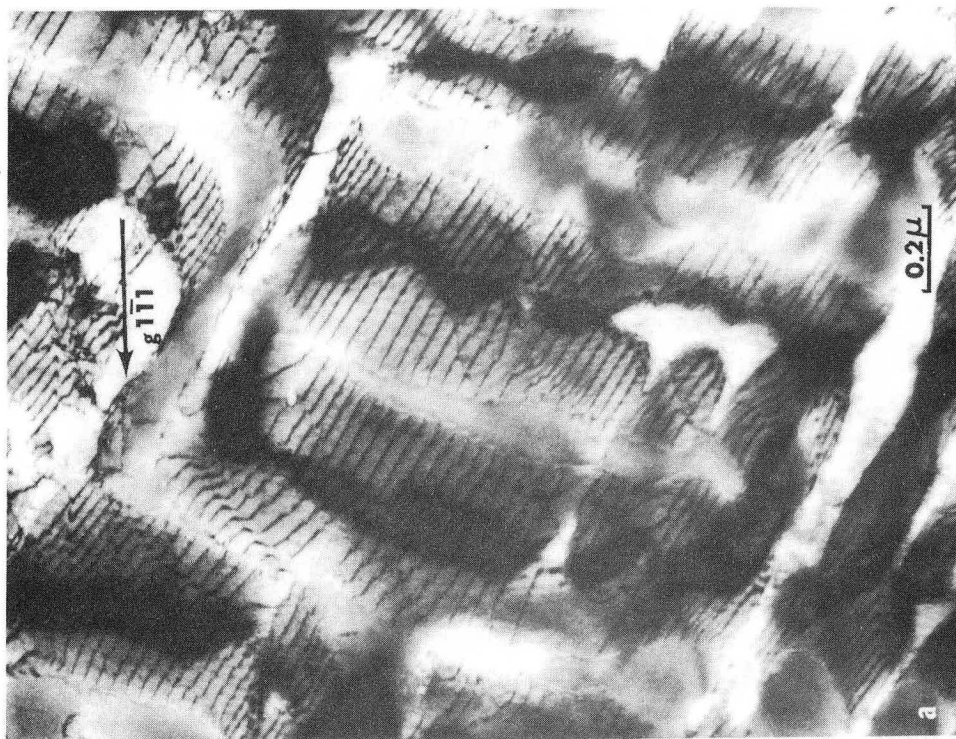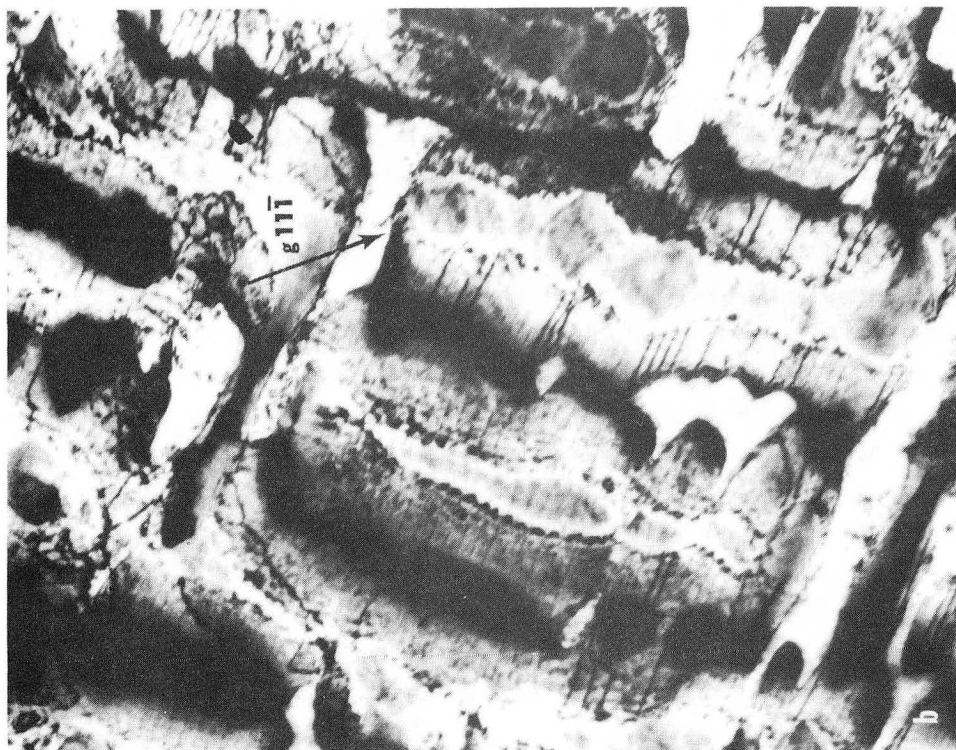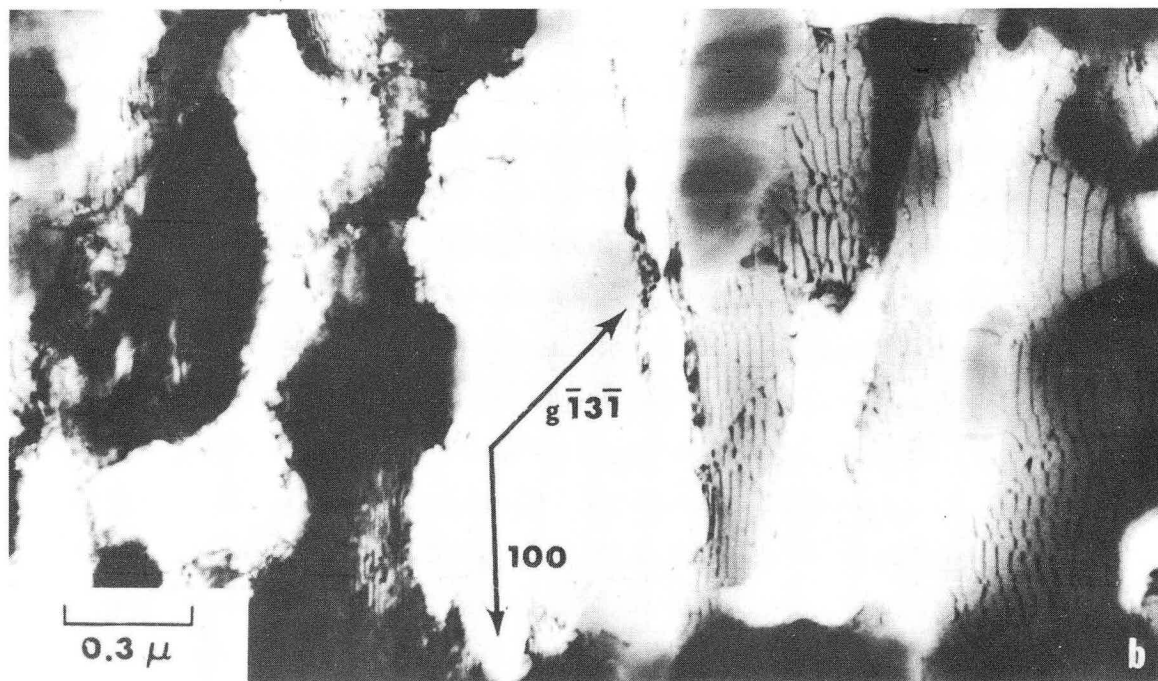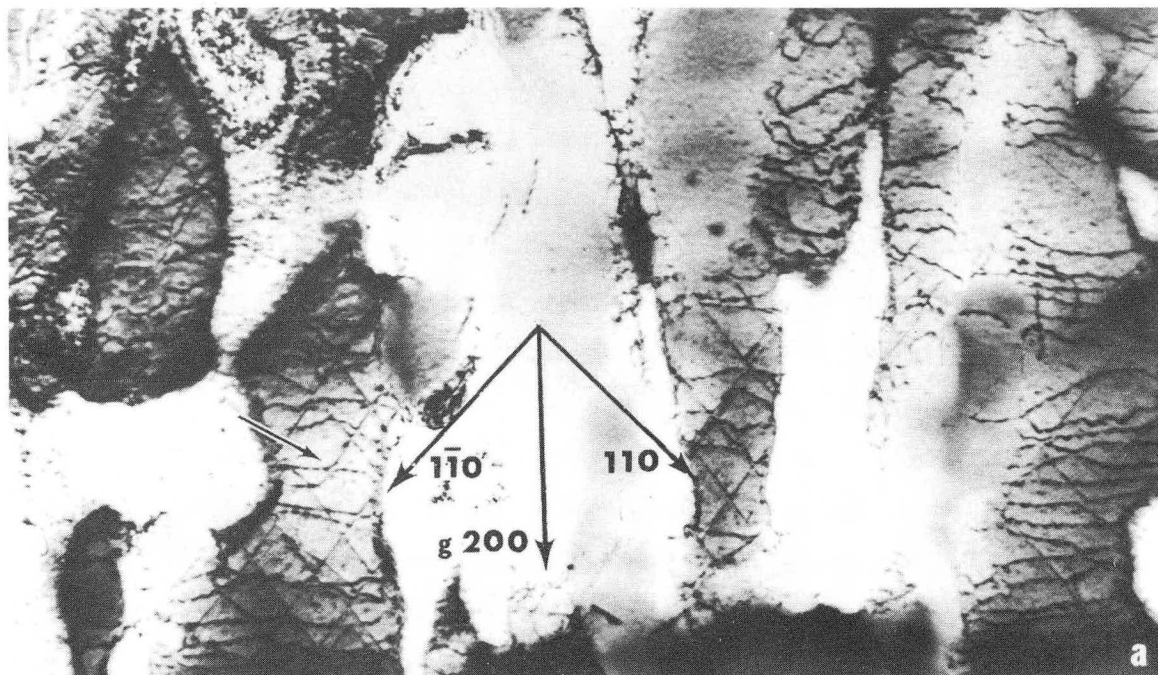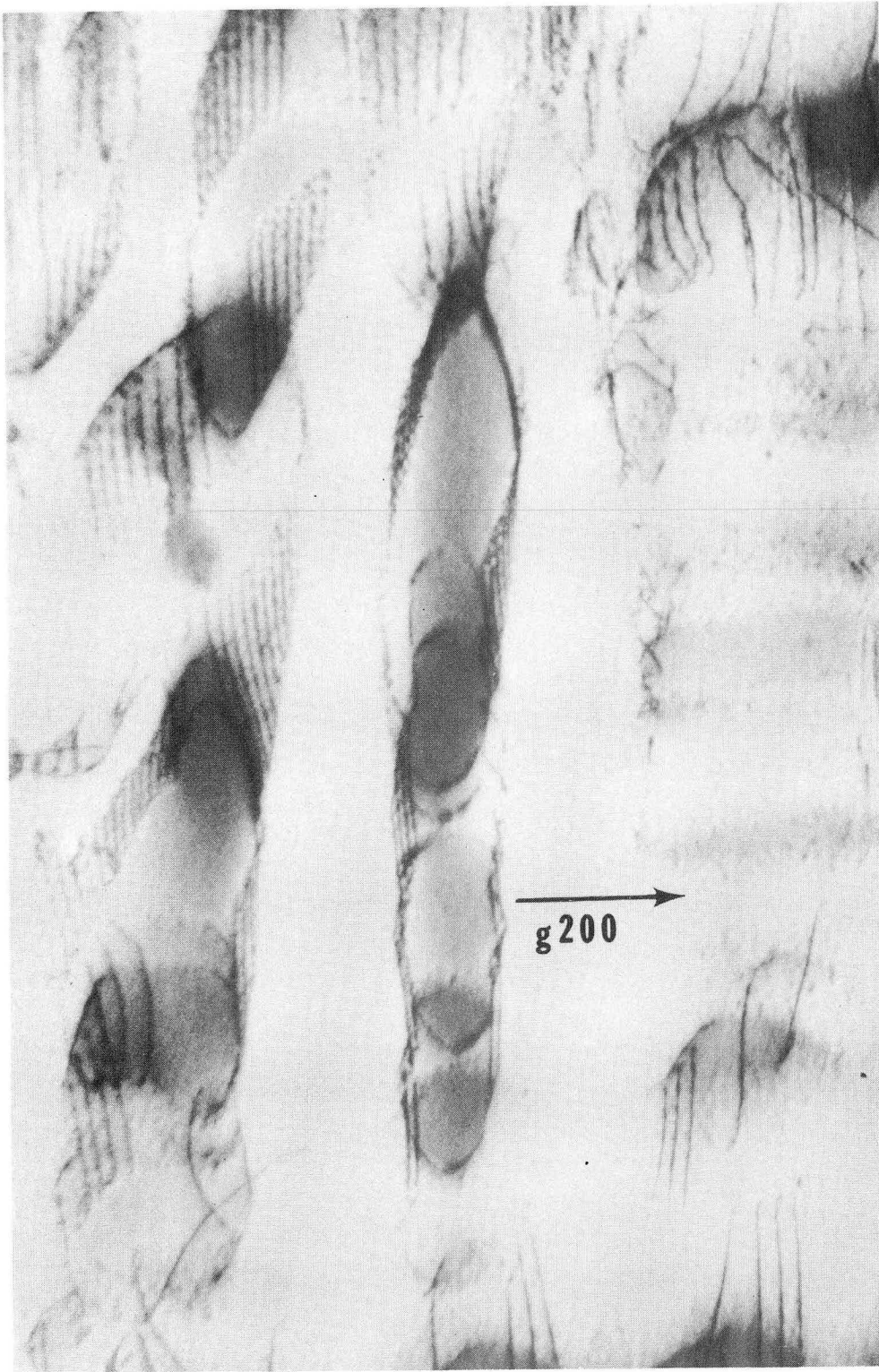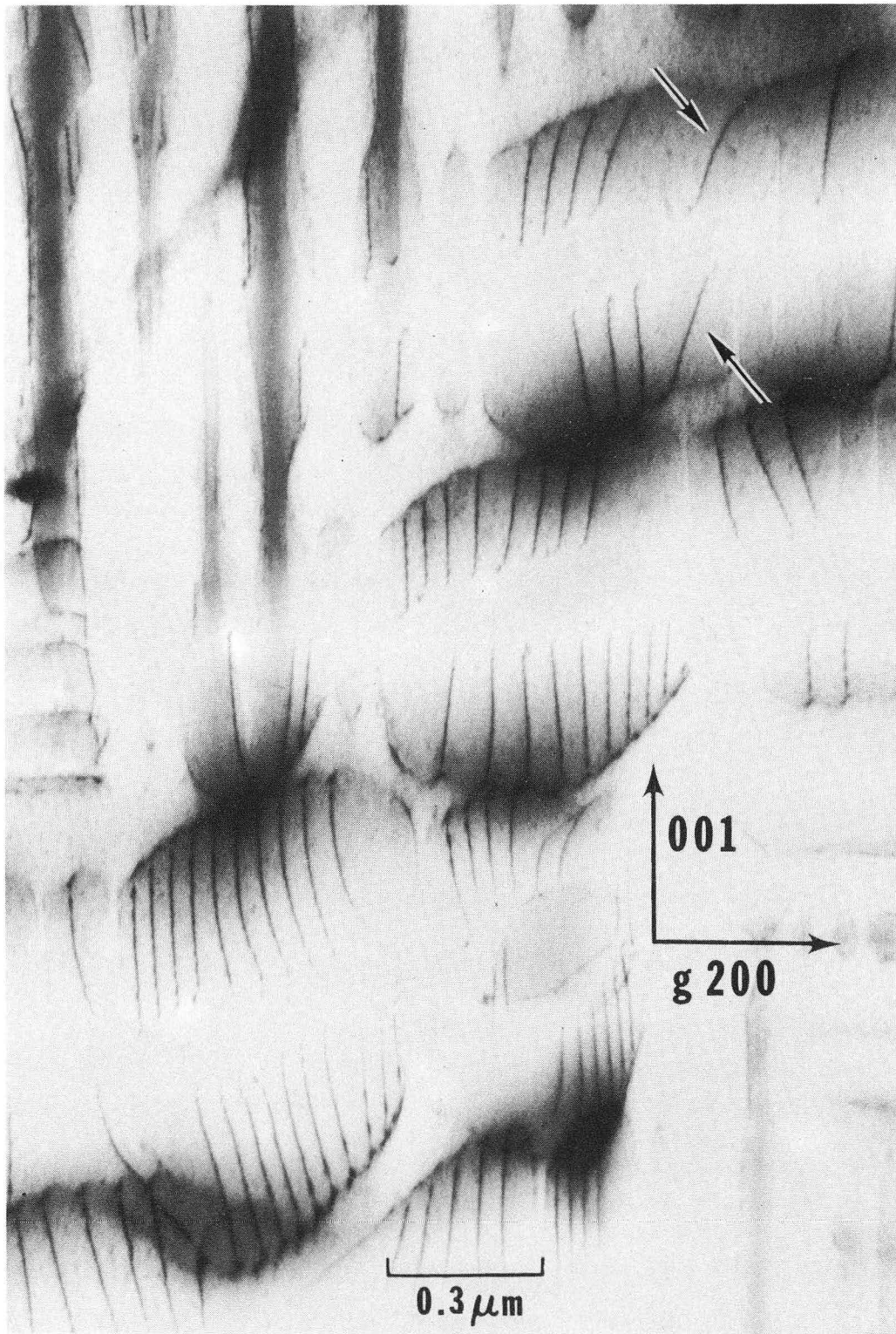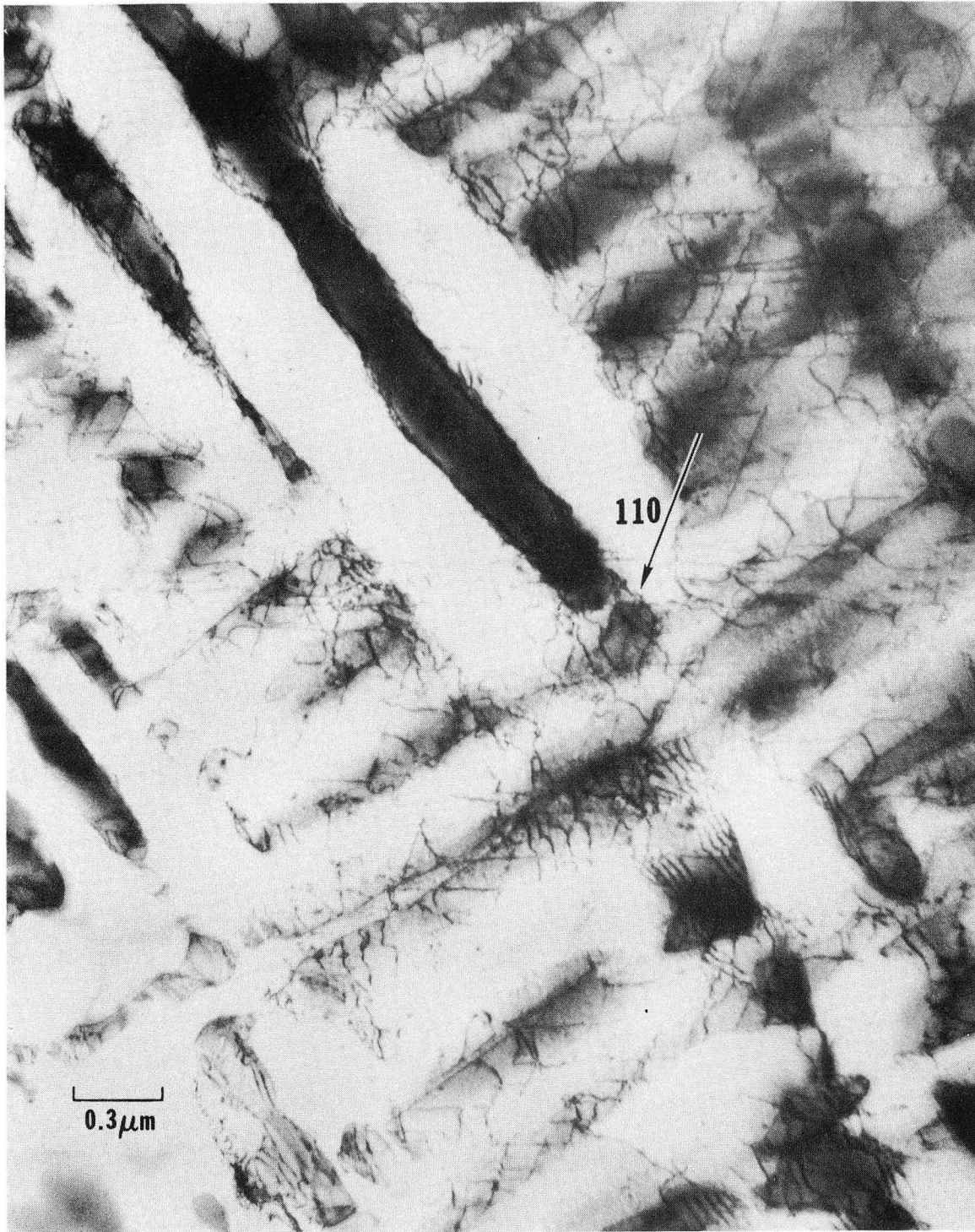
XBB 729-4746

Fig. 12
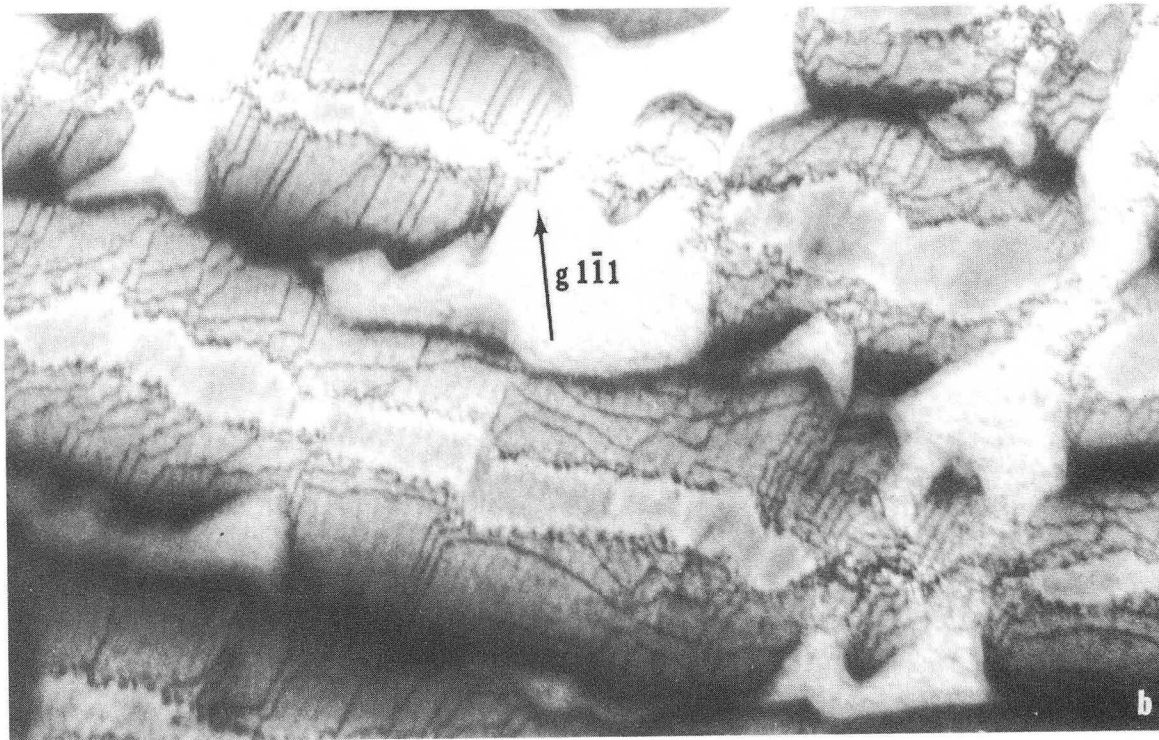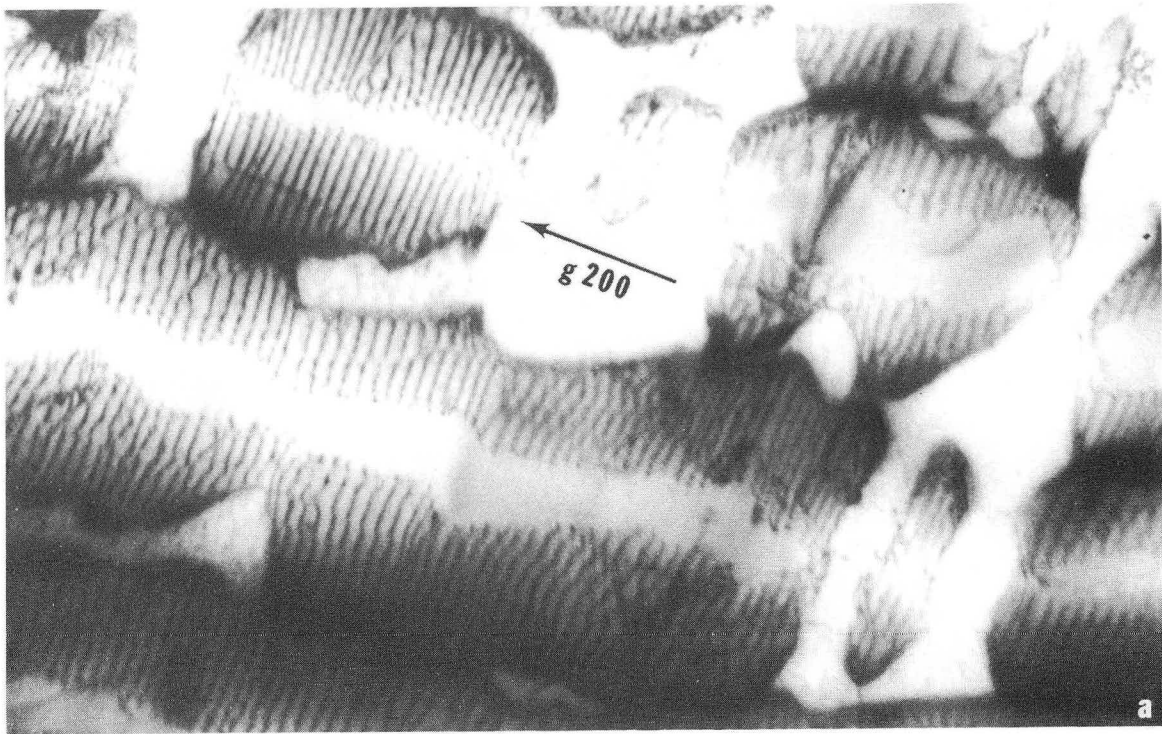
XBB 729-4735

Fig. 13
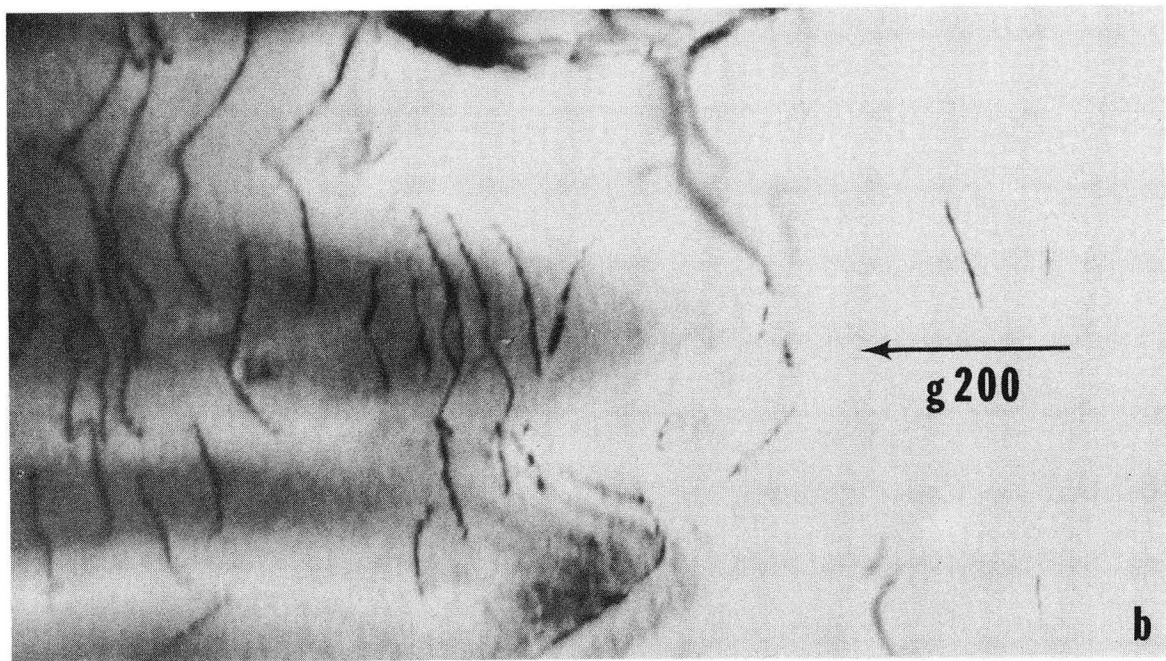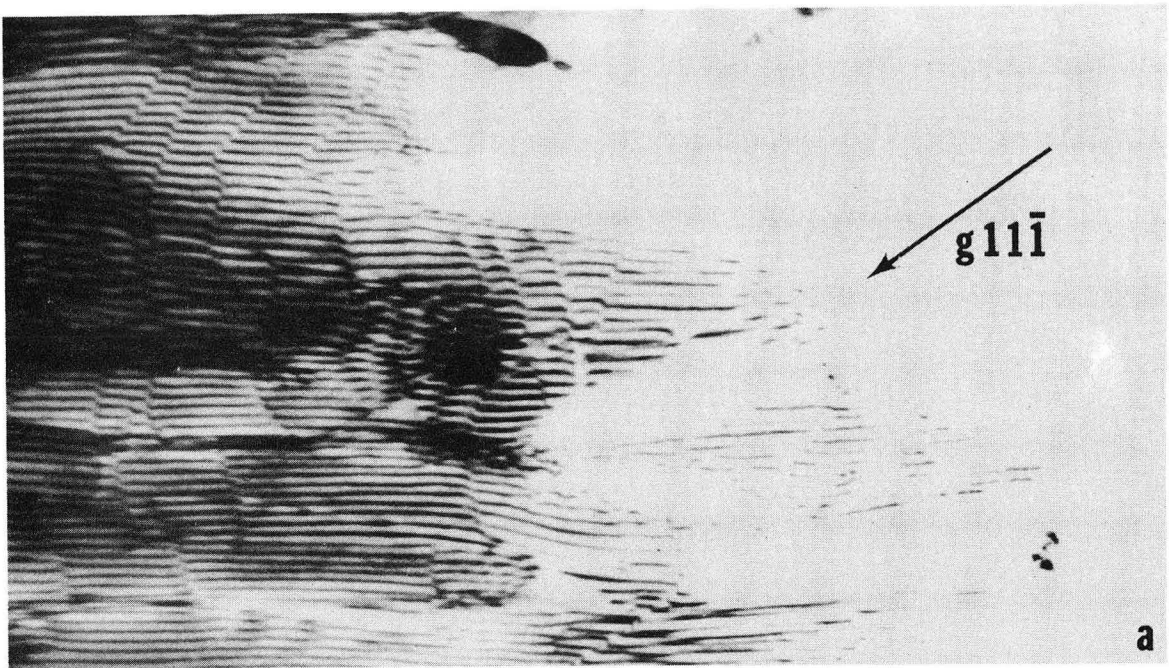
Fig. 14
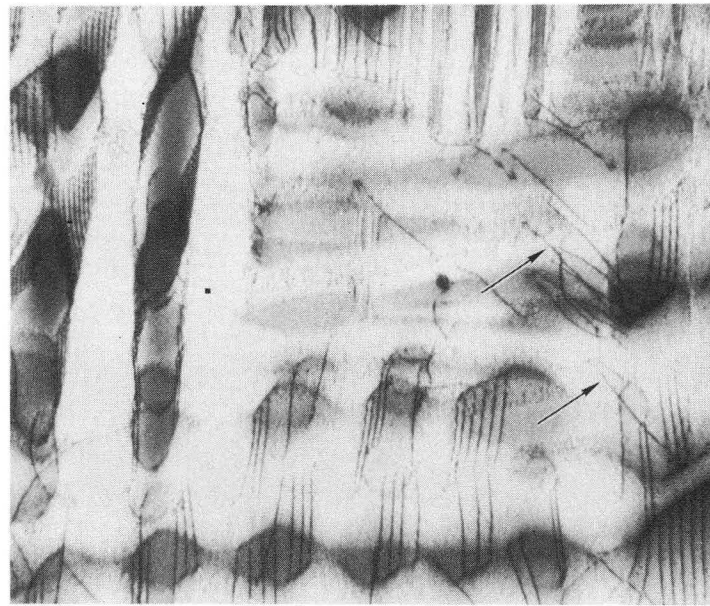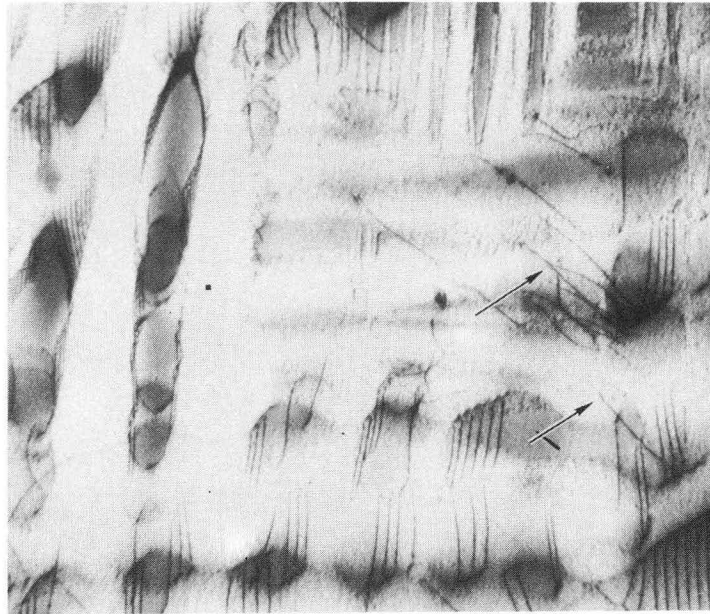
XBB 729-4728

XBB 729-4724

Fig. 15
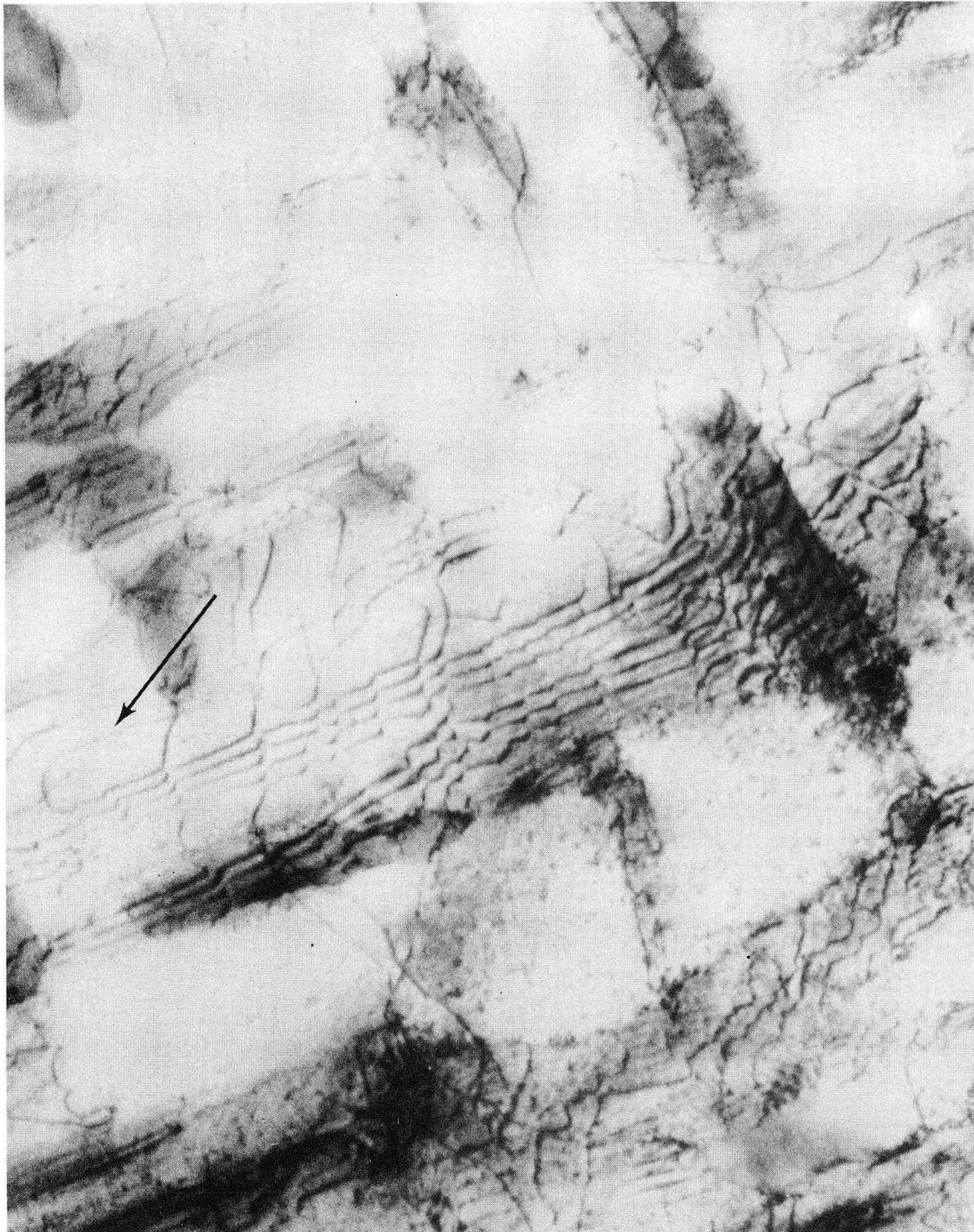
XBB 729-4736

Fig. 16

XBB 729-4725

Fig. 17

Fig. 18

XBB 729-4741

0.5 μm
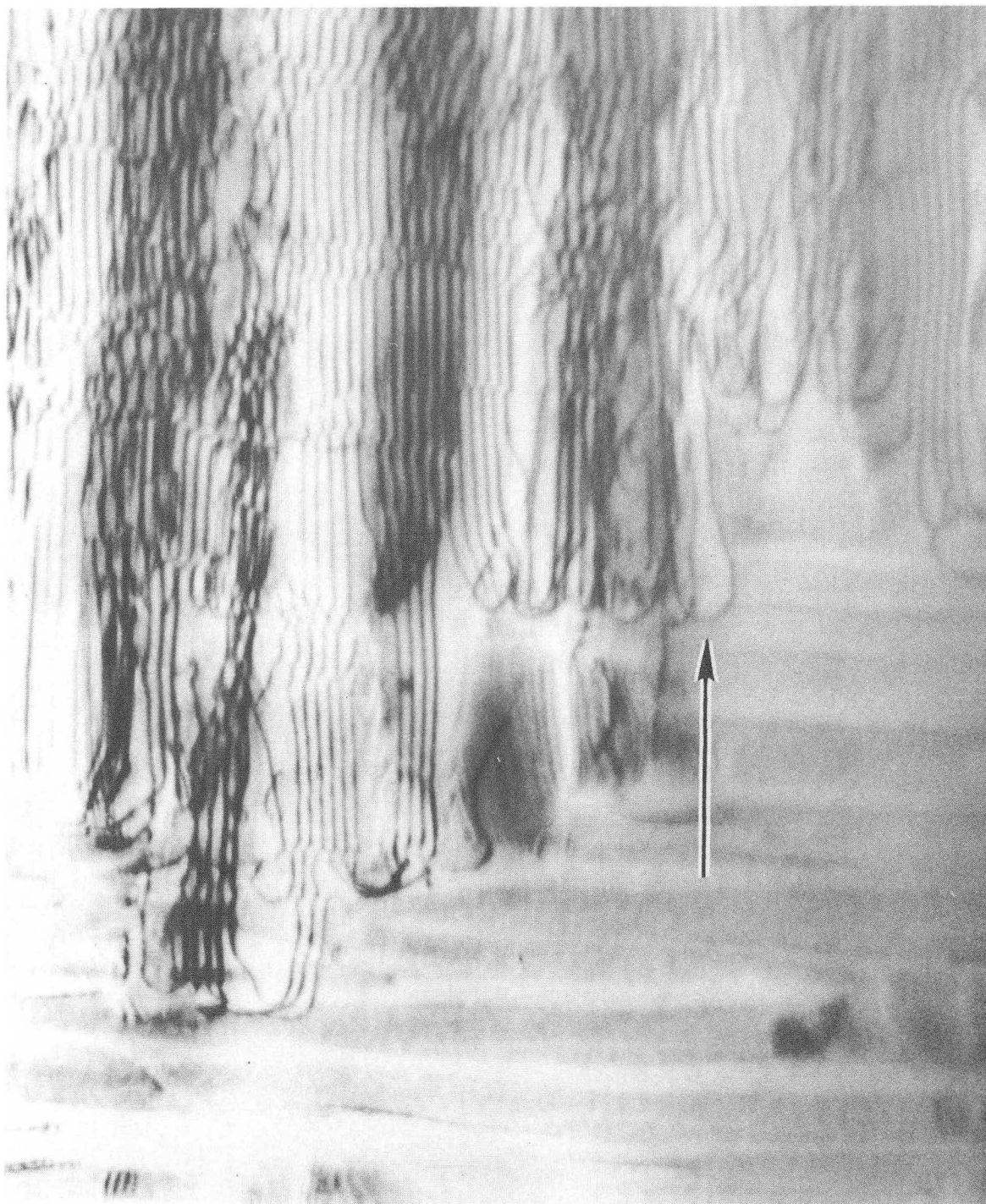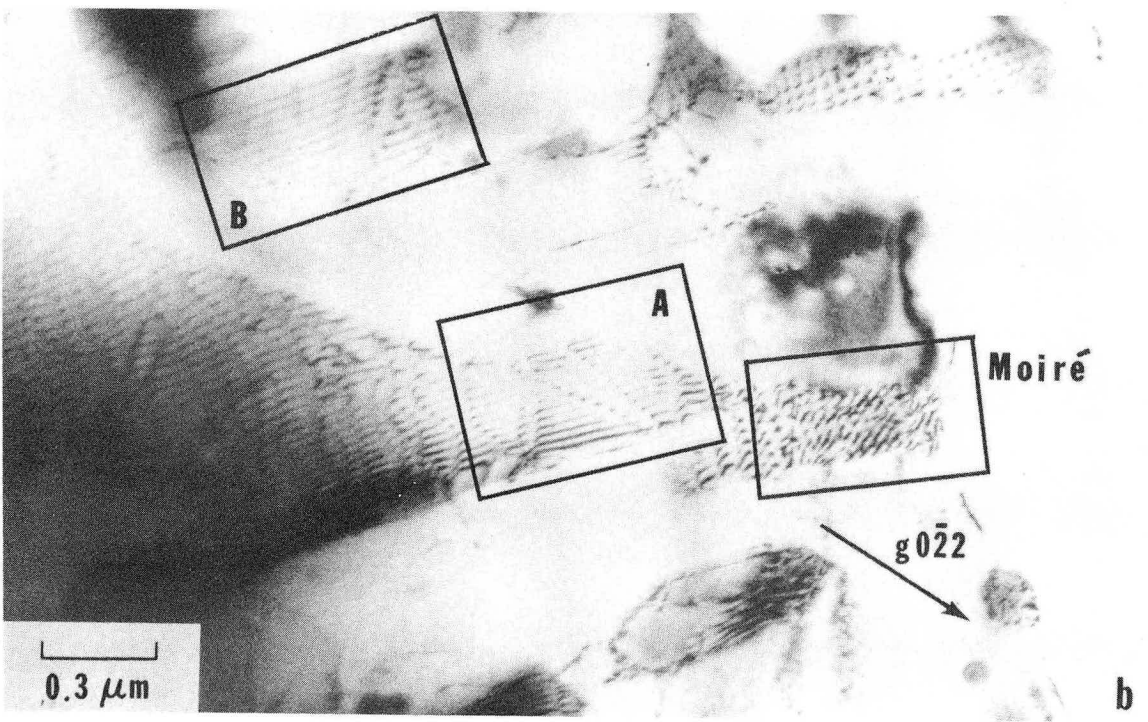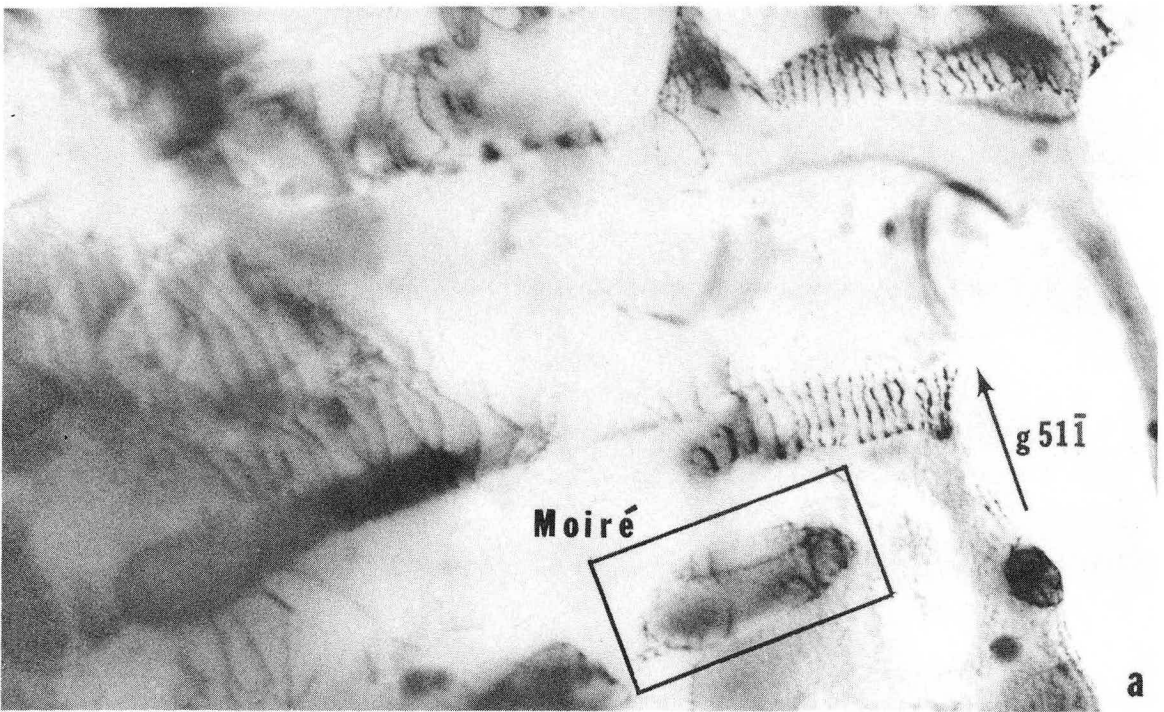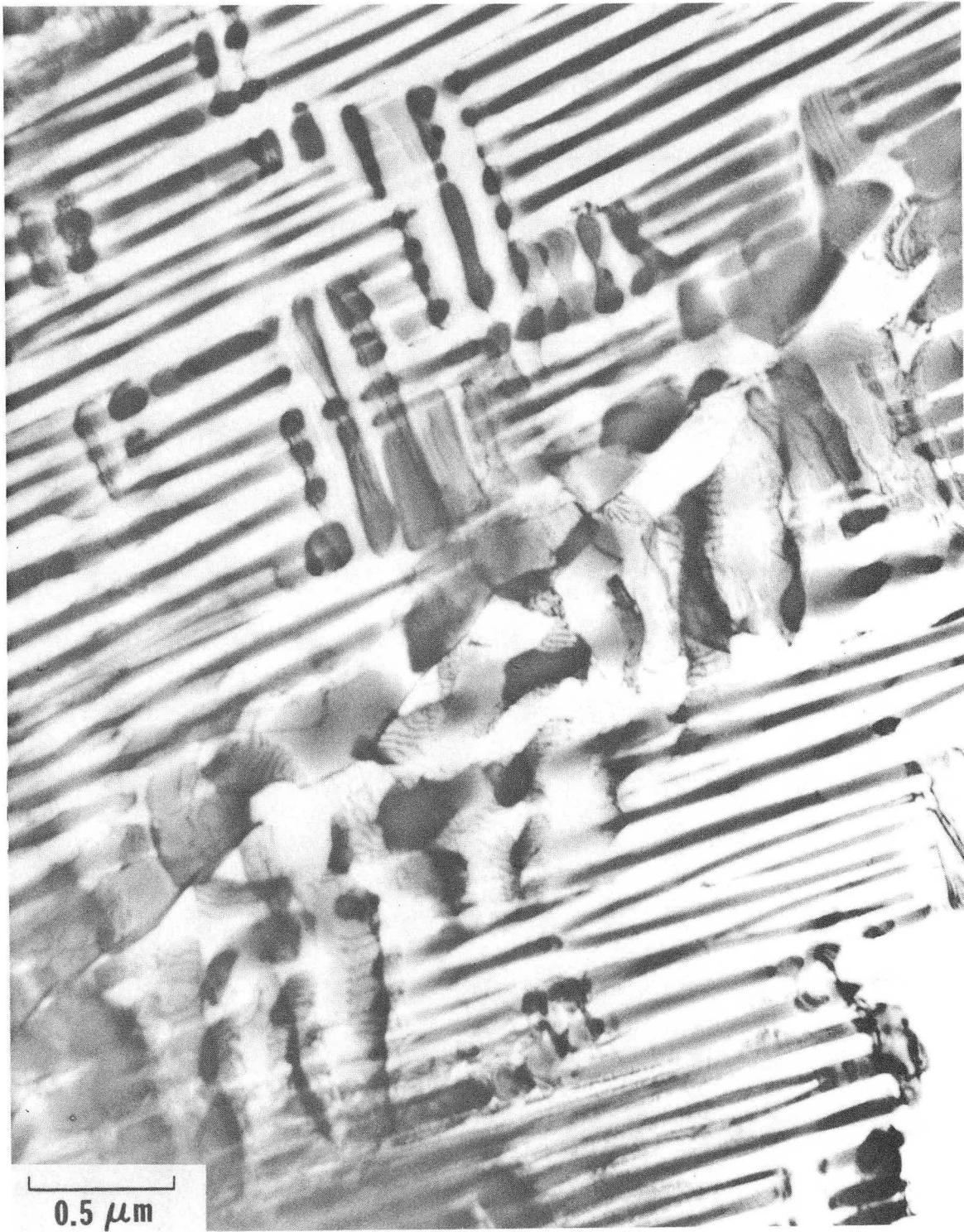
XBB 729-4740

Fig. 19
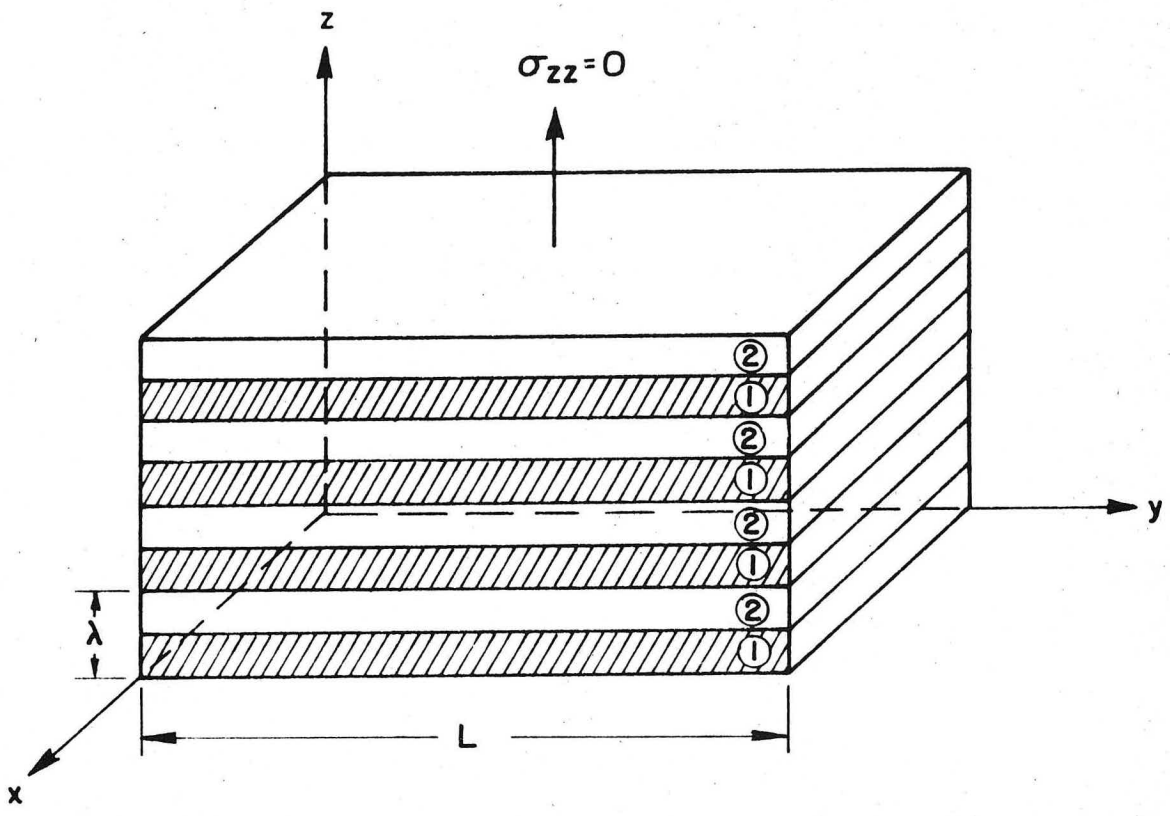
Fig. 20

XBL729 - 6902

Fig. 21

-115-

(a)

(b)

$\bar{b} = a/2\,[0\bar{1}1]$

(c)
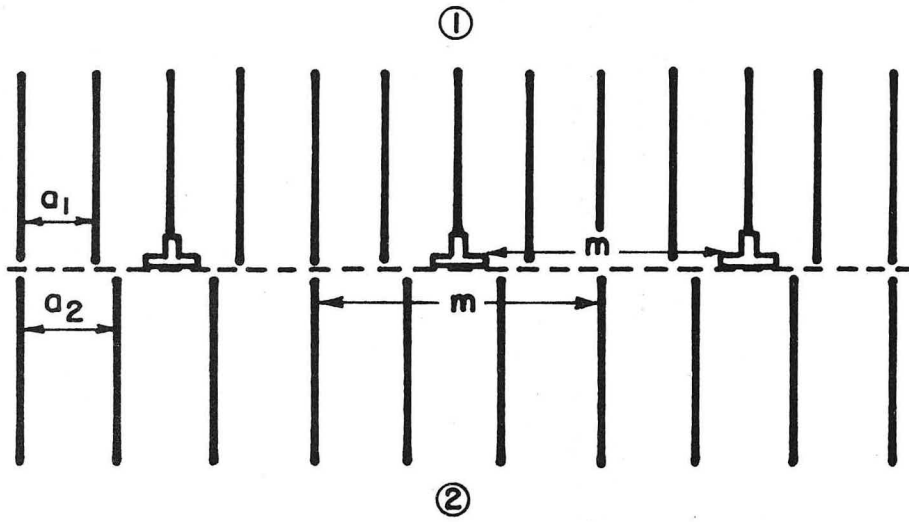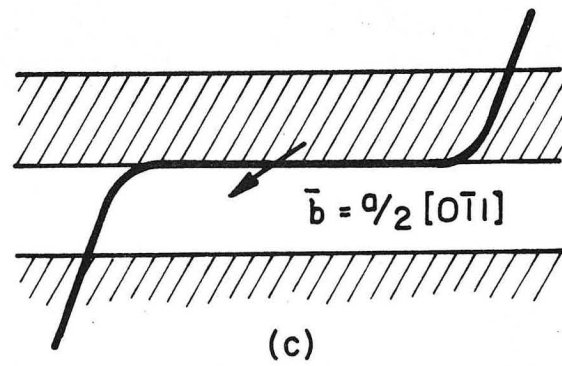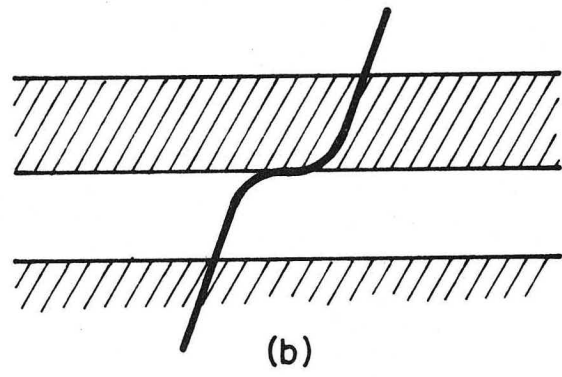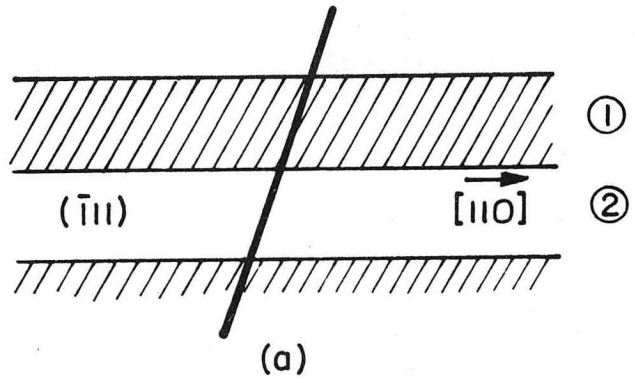
XBL 729-6903

Fig. 22
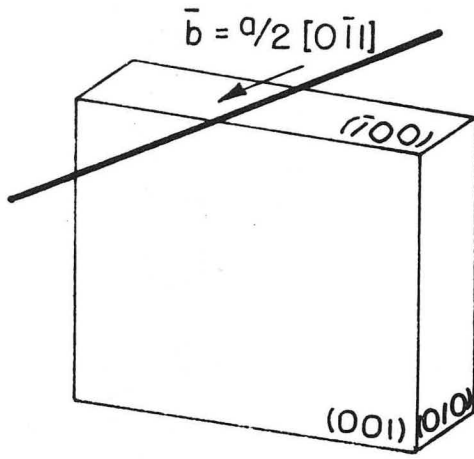
(a)
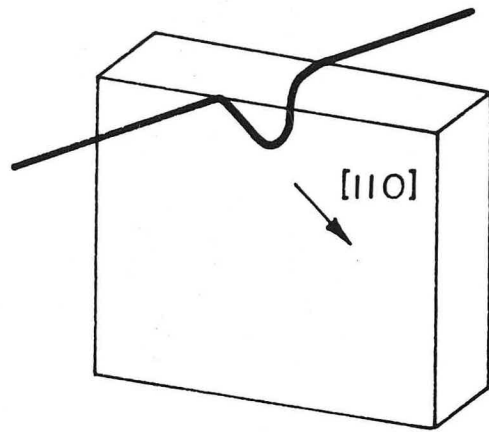
(b)
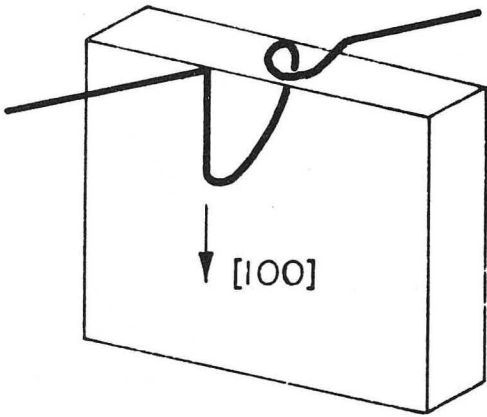
(c)
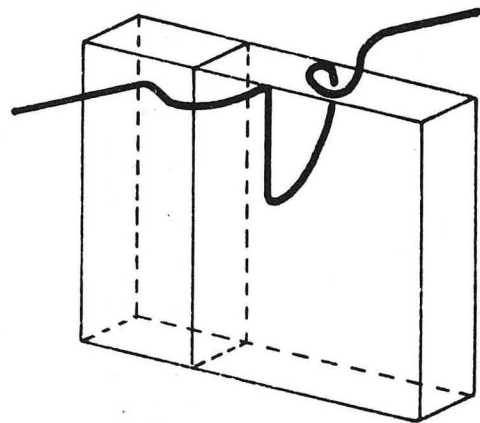
(d)

XBL 729-6904

Fig. 23

$\bar{b}$

$\bar{b}$

$\bar{b}$

(a)

(b)

(c)
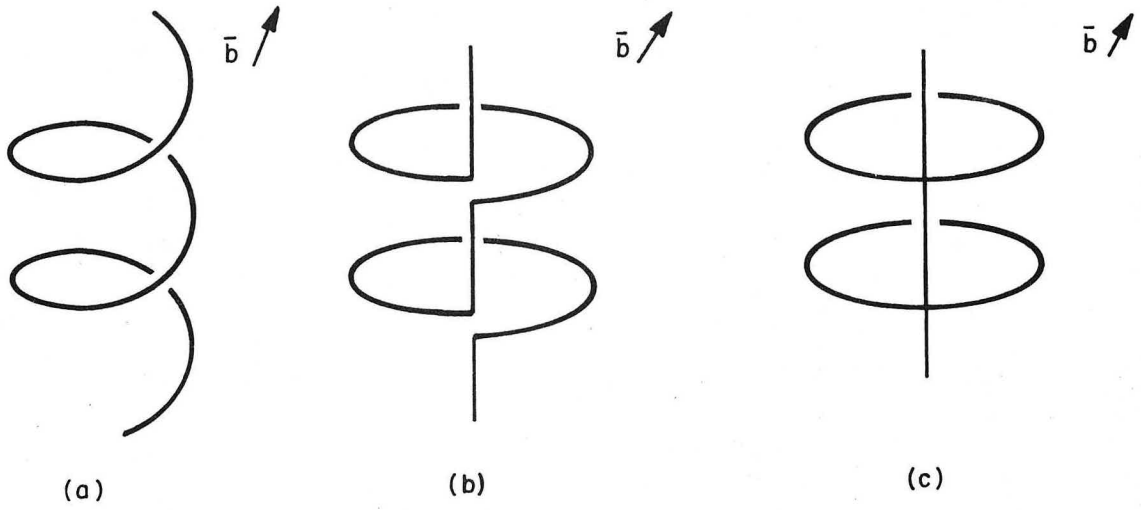
XBL729-6905

Fig. 24
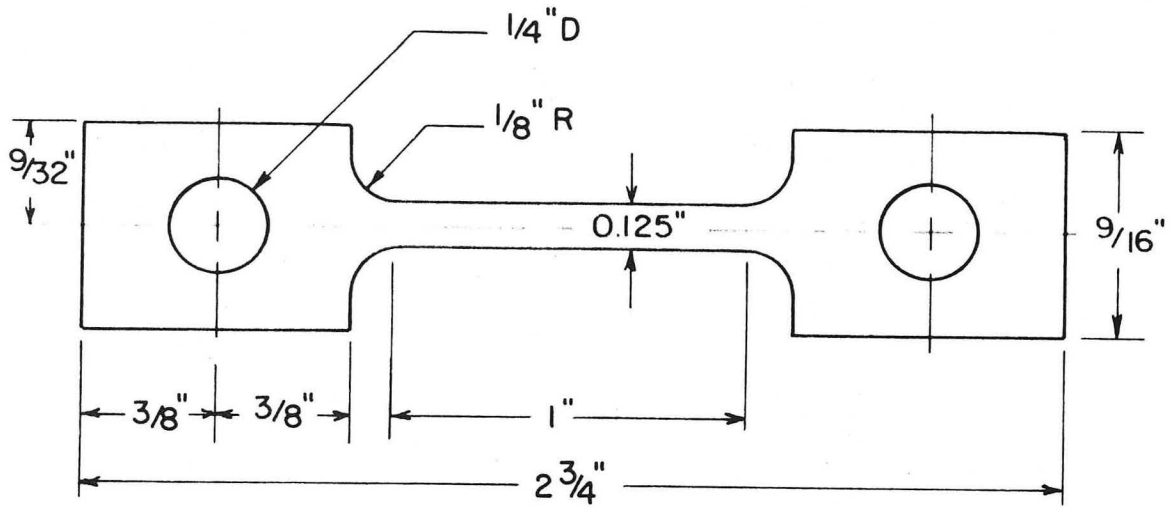
GAGE LENGTH: 1"

TENSILE SPECIMEN

XBL 705-911

Fig. 25

0.5 μm

XBB 729-4723

Fig. 26a

0.5 μm

b
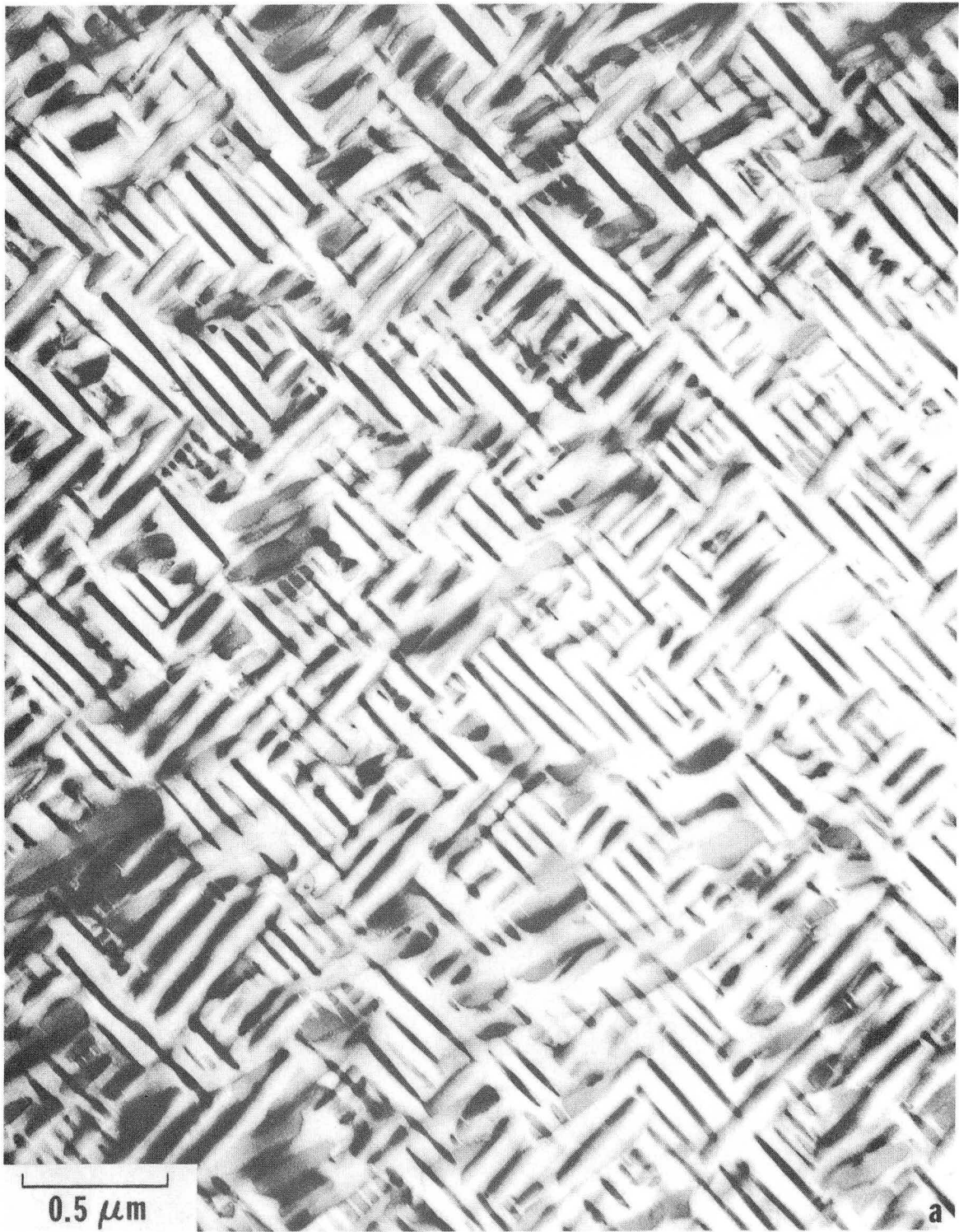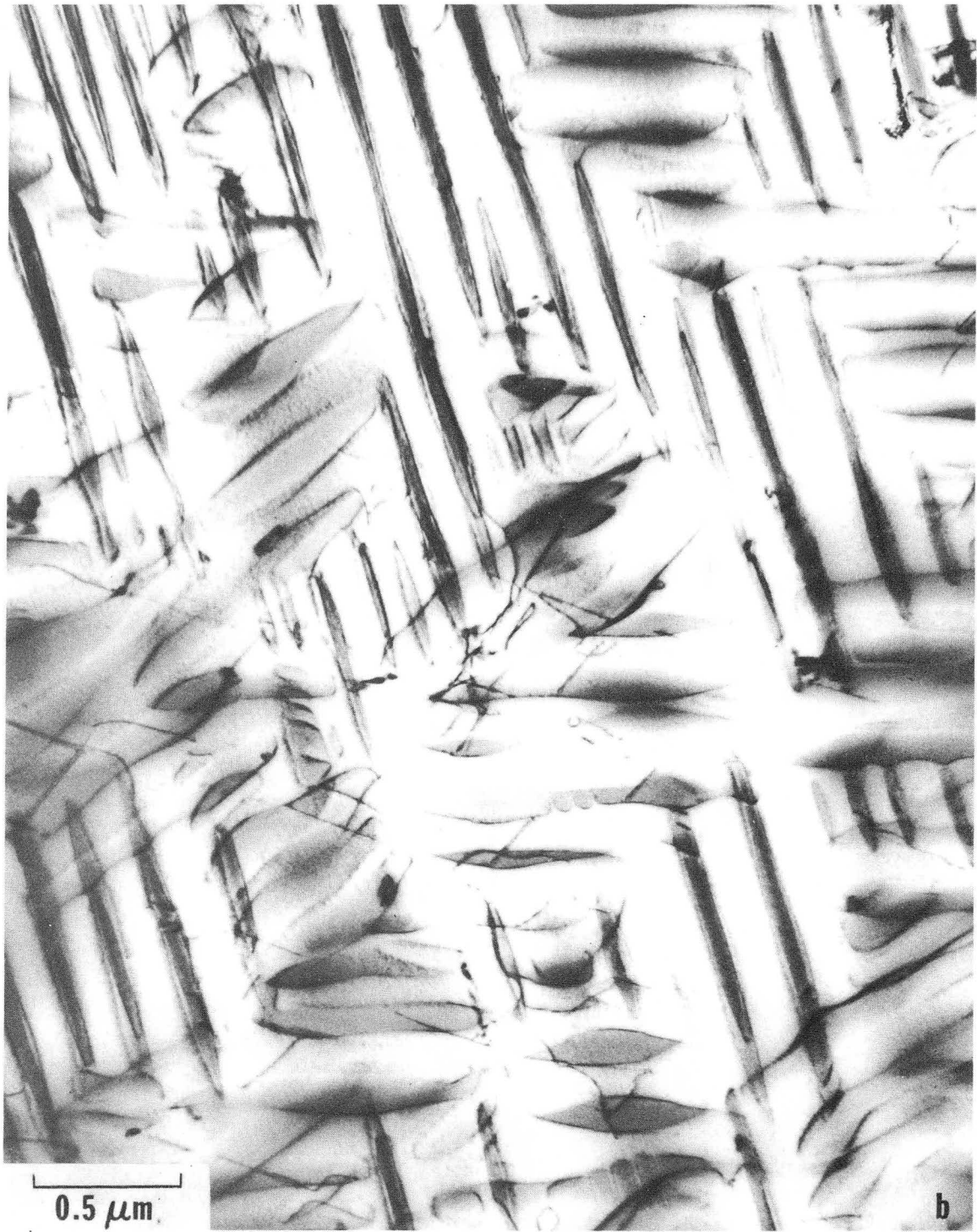
XBB 729-4739

Fig. 26b

0.5 μm
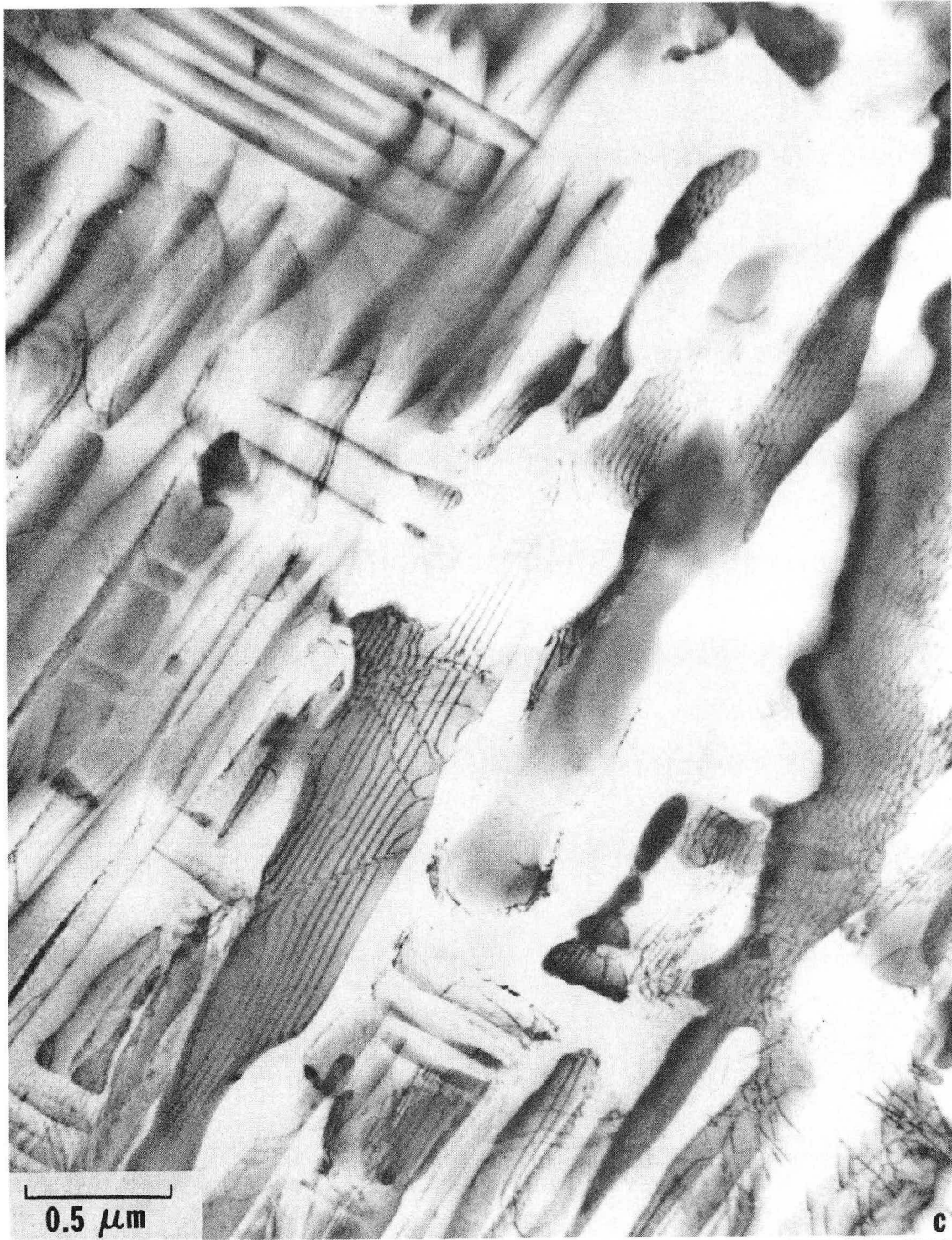
XBB 729-4738

Fig. 26c

0.3 μm

g 200

g 1Ī1

g 11Ī

XBB 729-4737

Fig. 27

0.5 μm
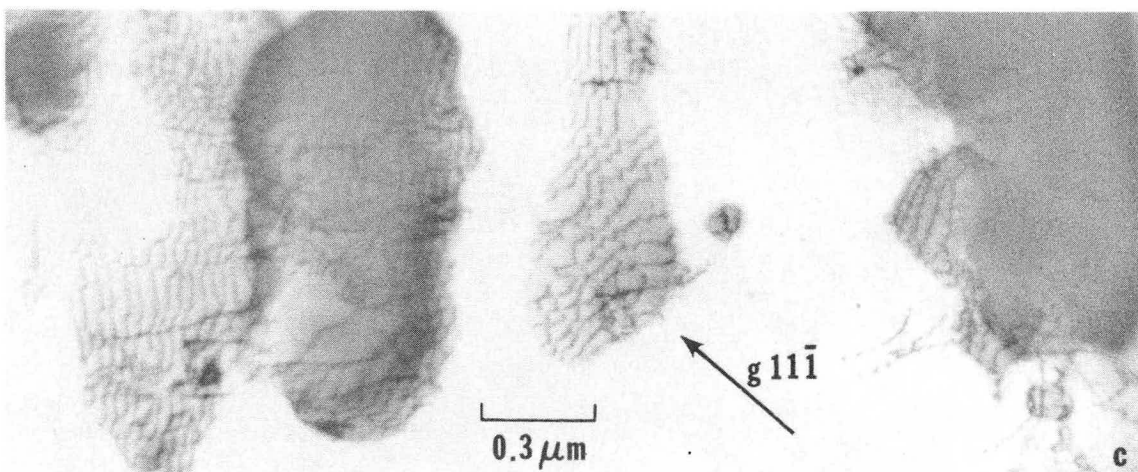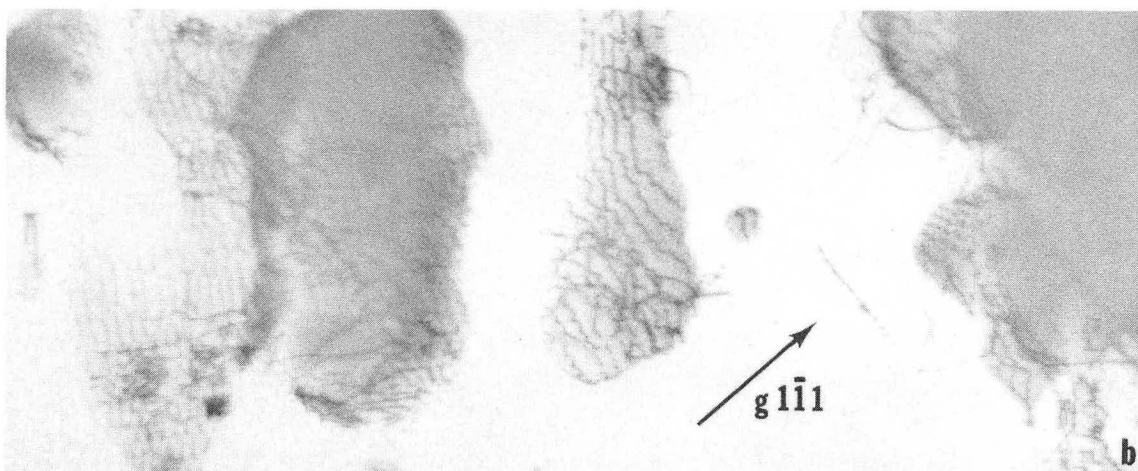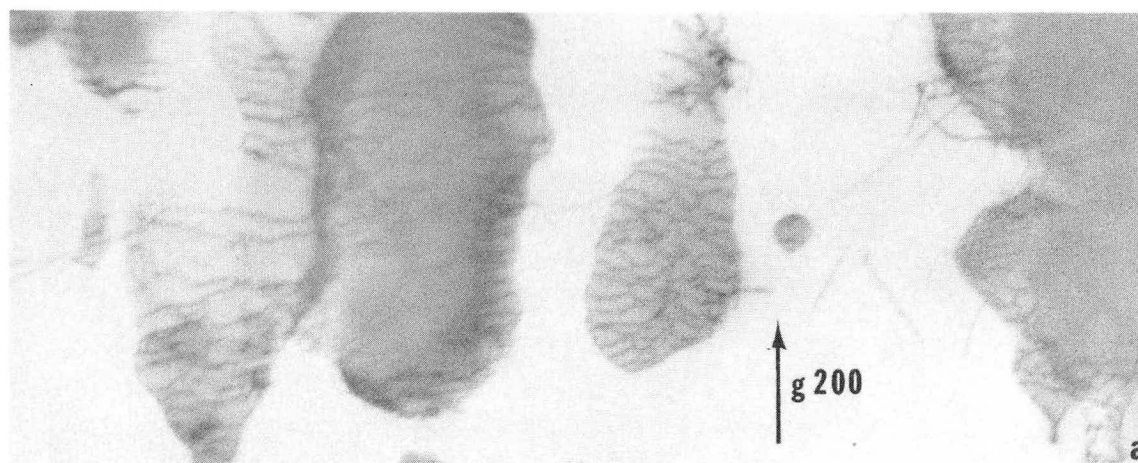
XBB 729-4729

Fig. 28
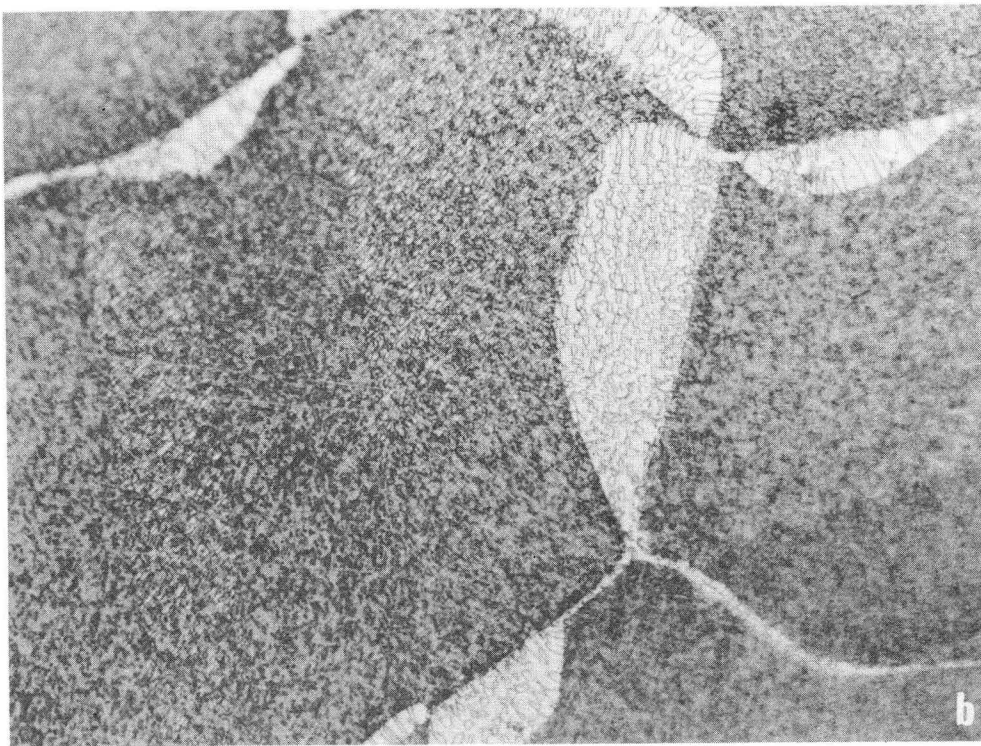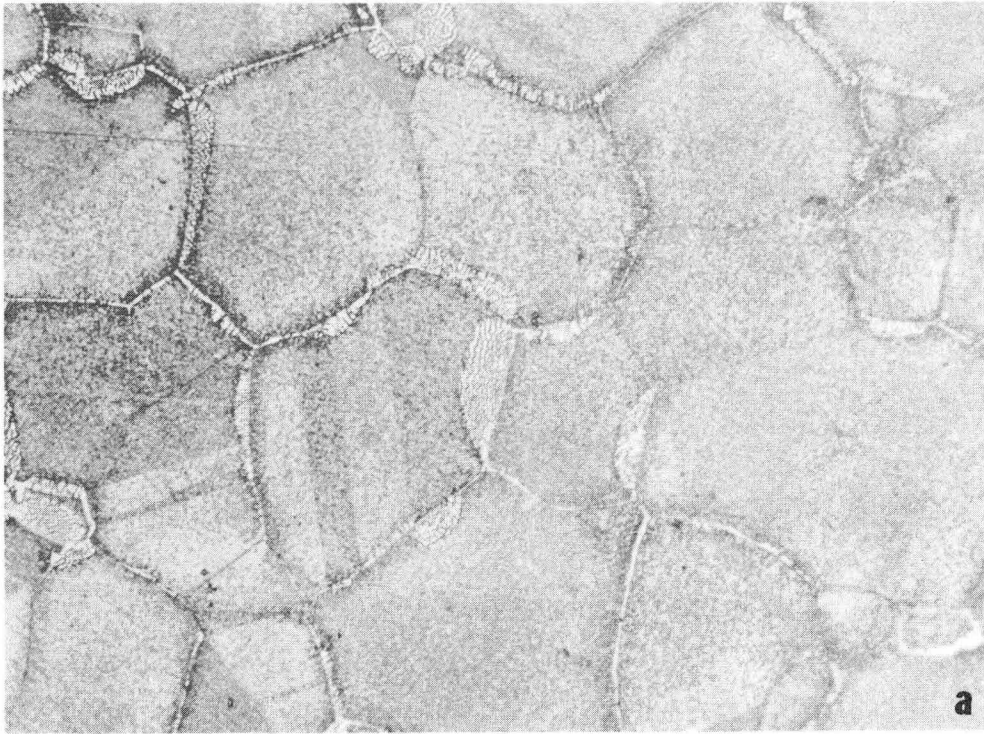
XBB 729-4613

Fig. 29
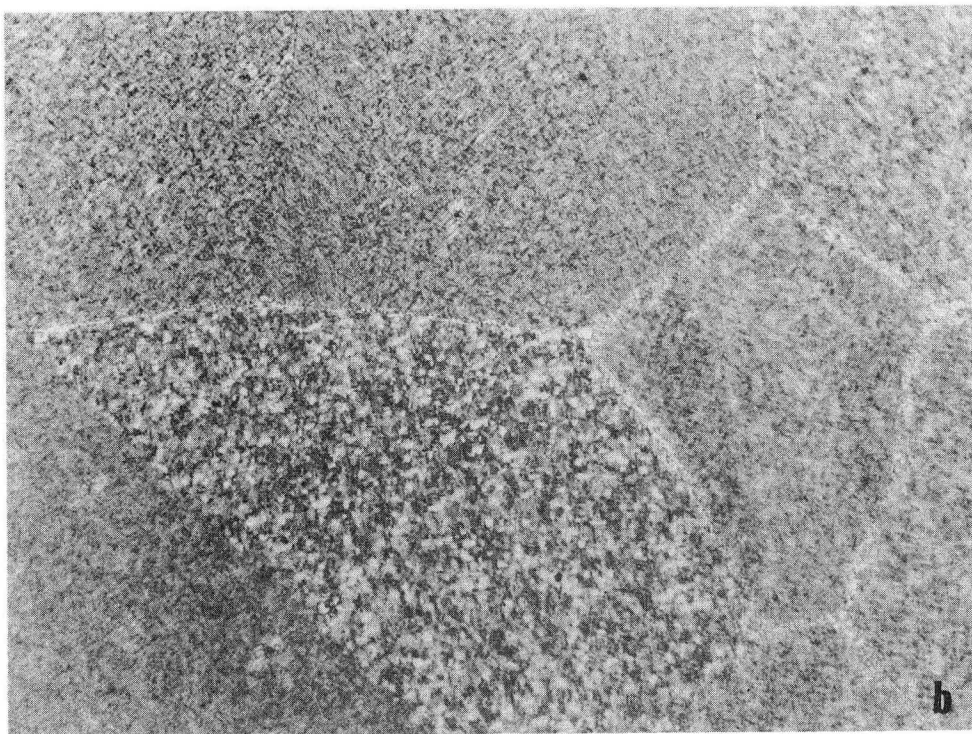
XBB 729-4614

Fig. 30
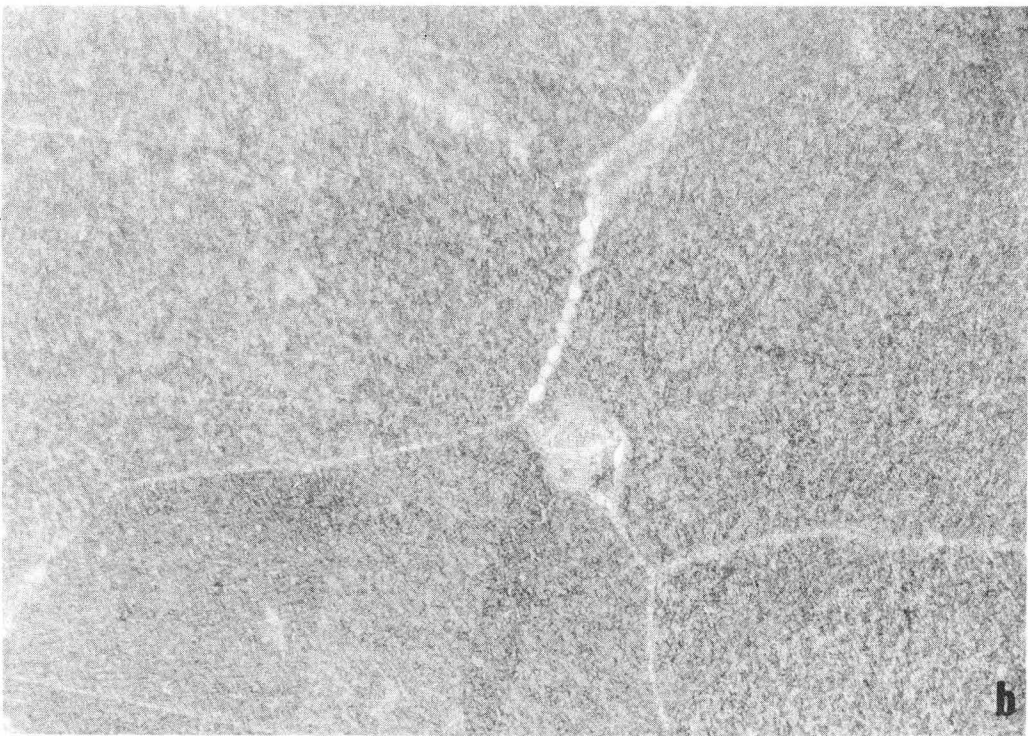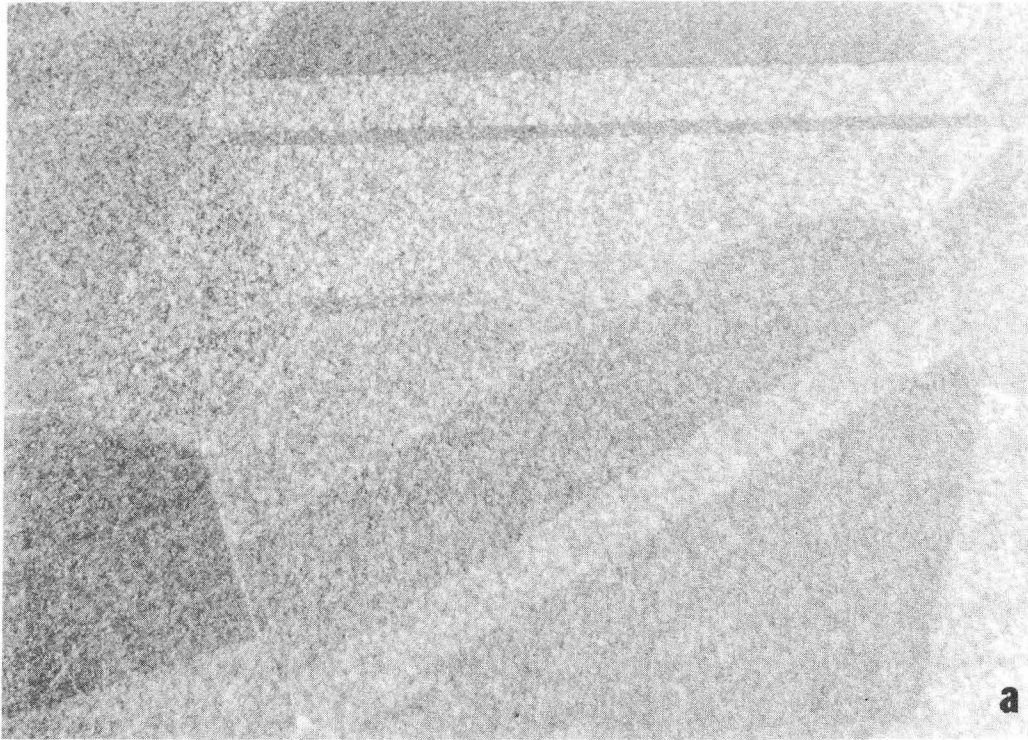
XBB 729-4619

Fig. 31
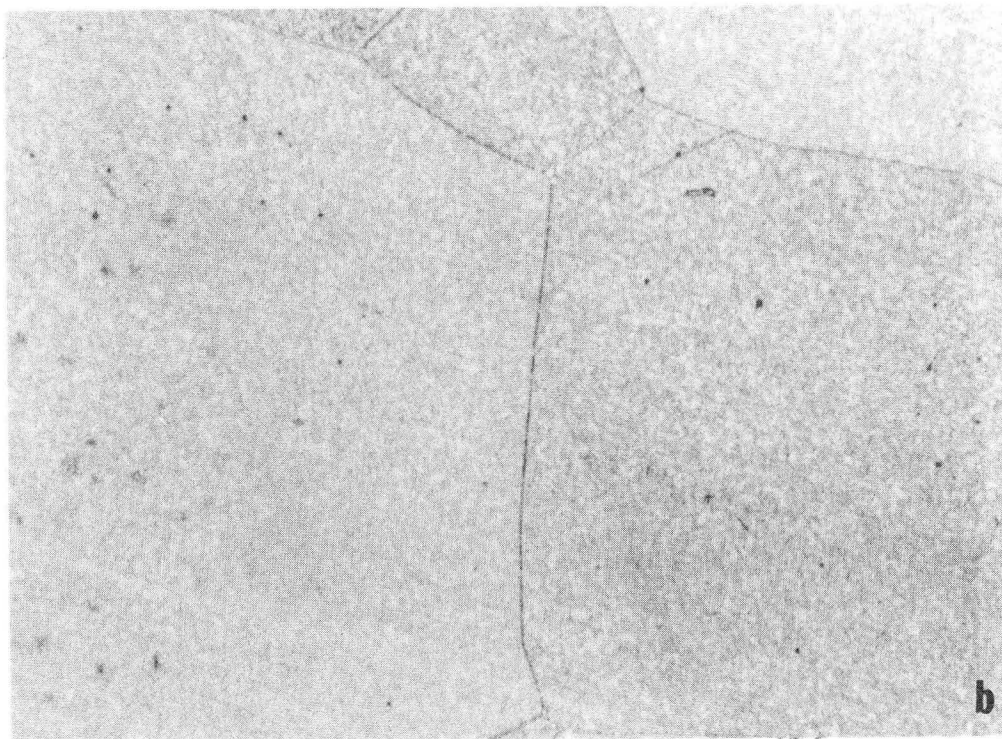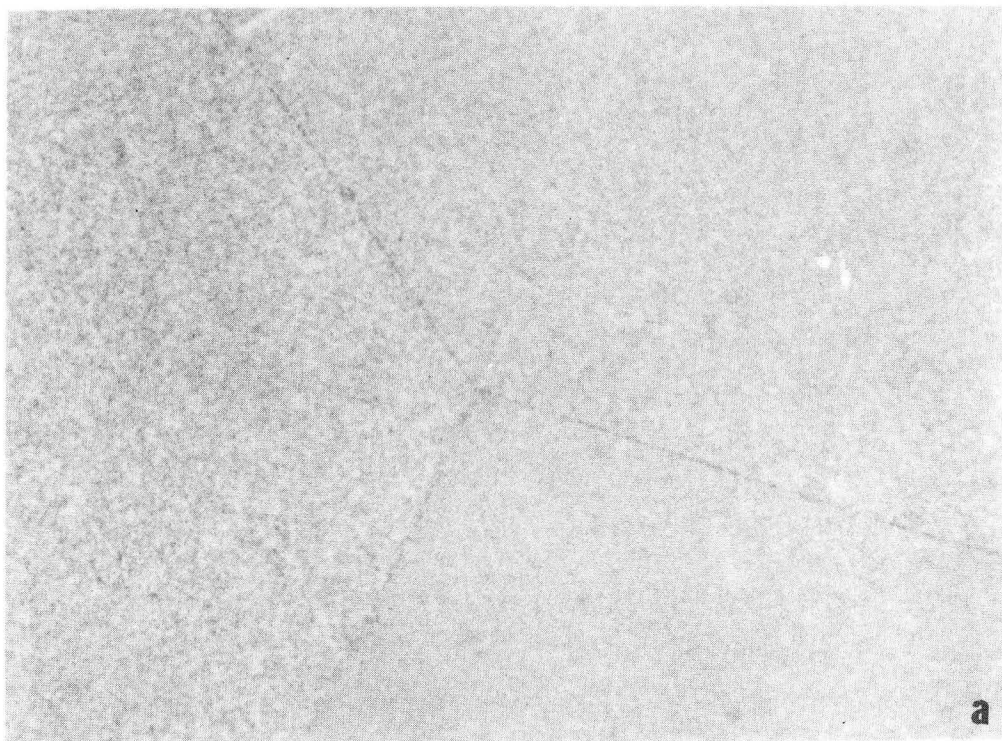
XBB 729-4620

Fig. 32
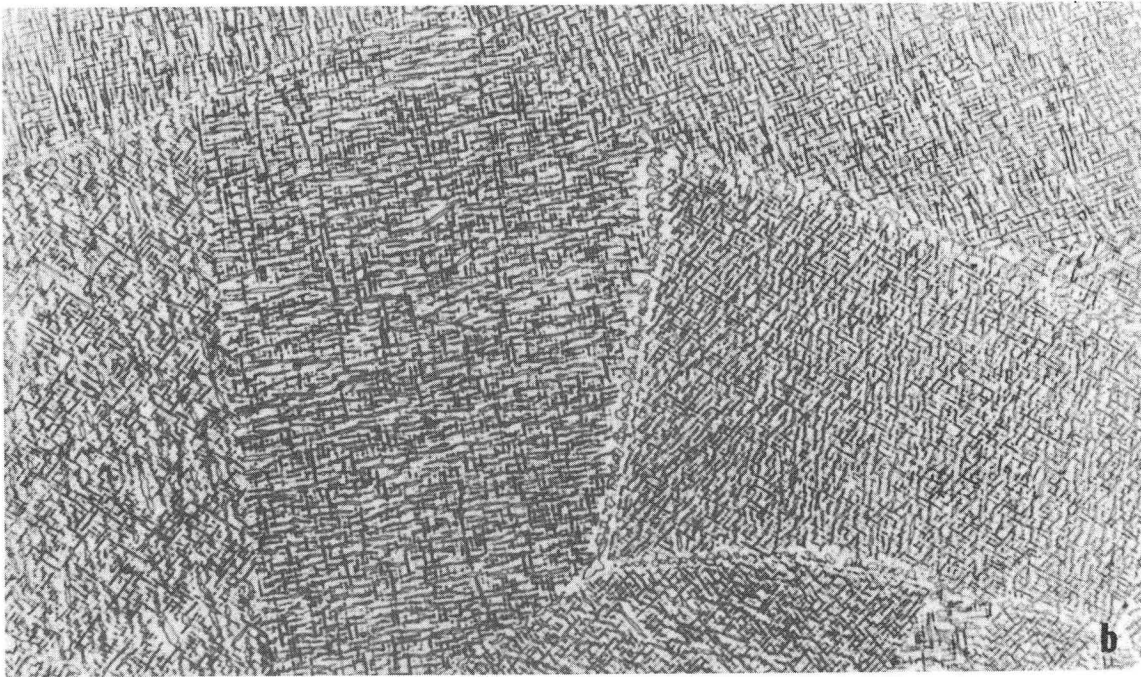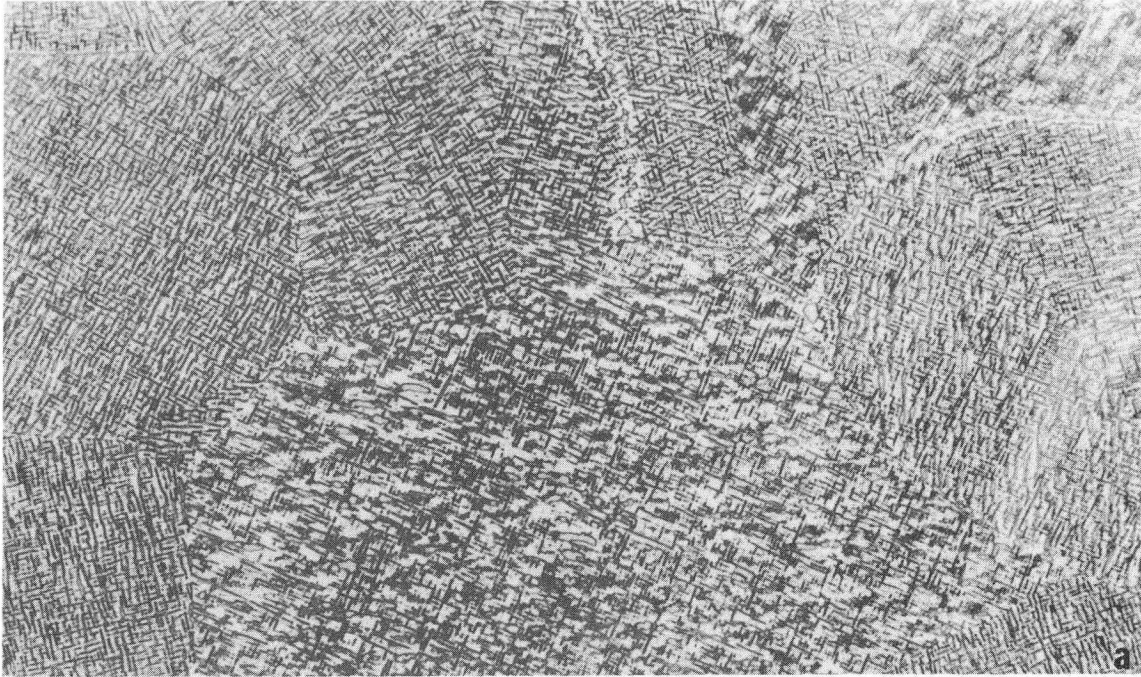
XBB 729-4615

Fig. 33
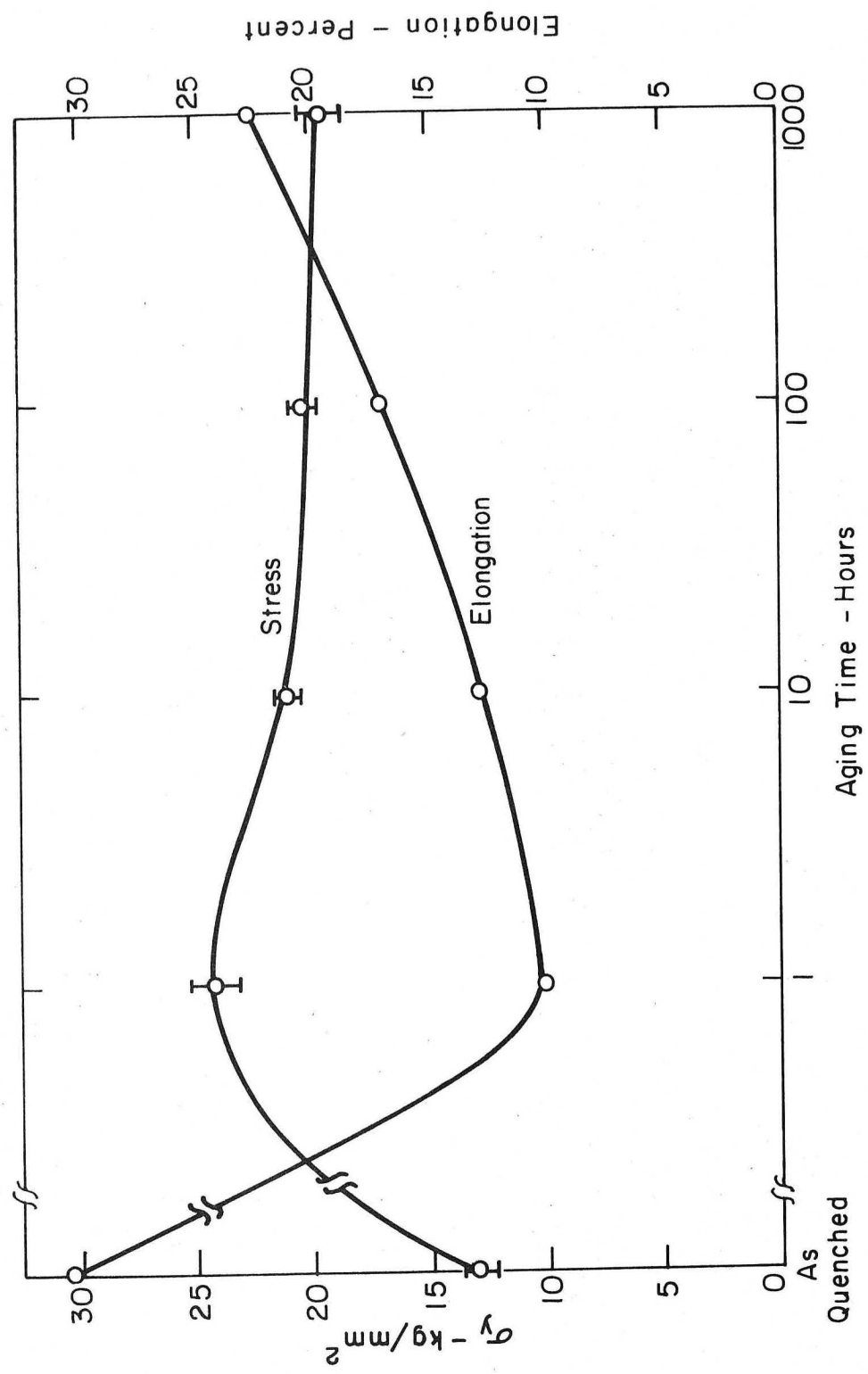
XBL729-6899

Fig. 34
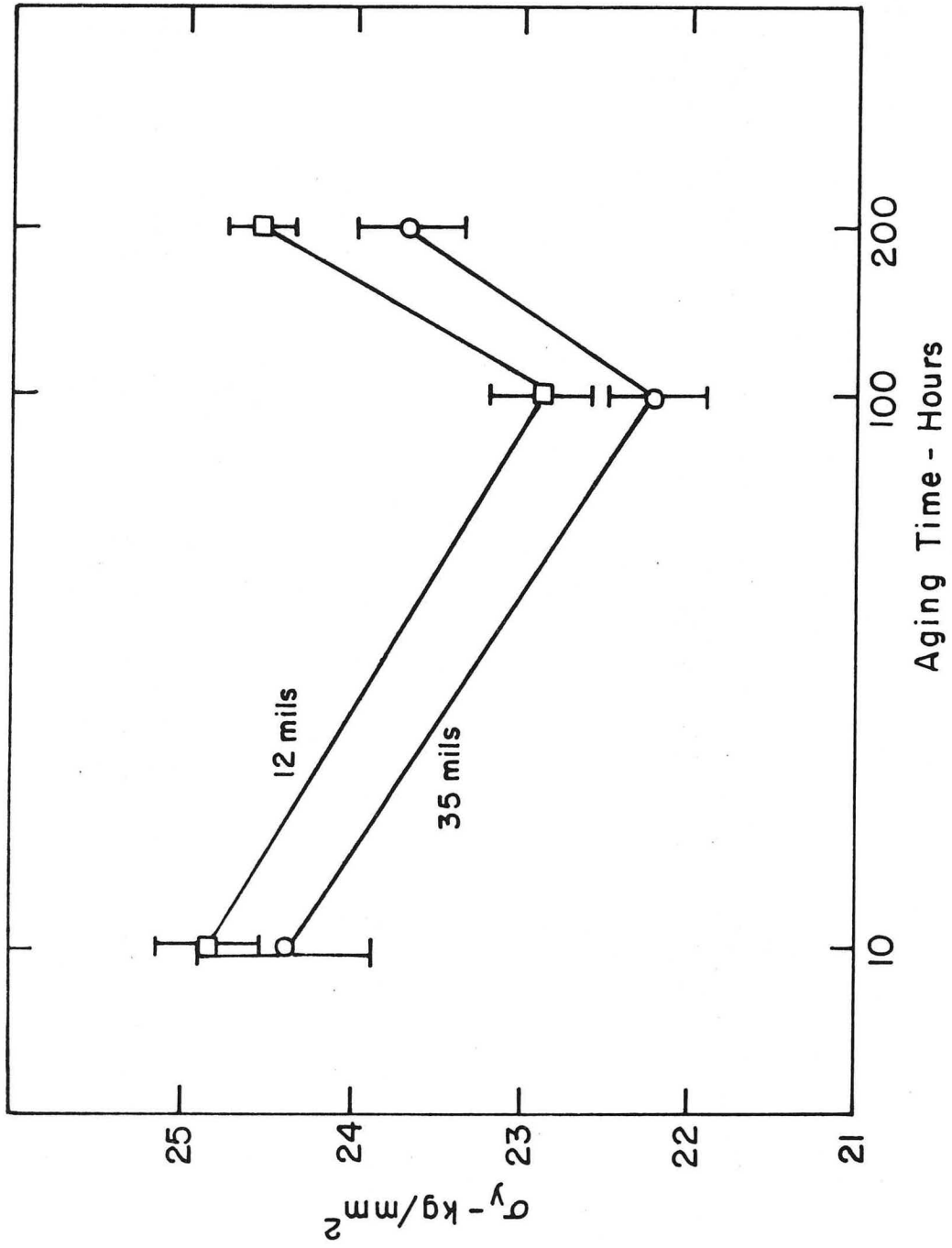
XBL729-6895

Fig. 35
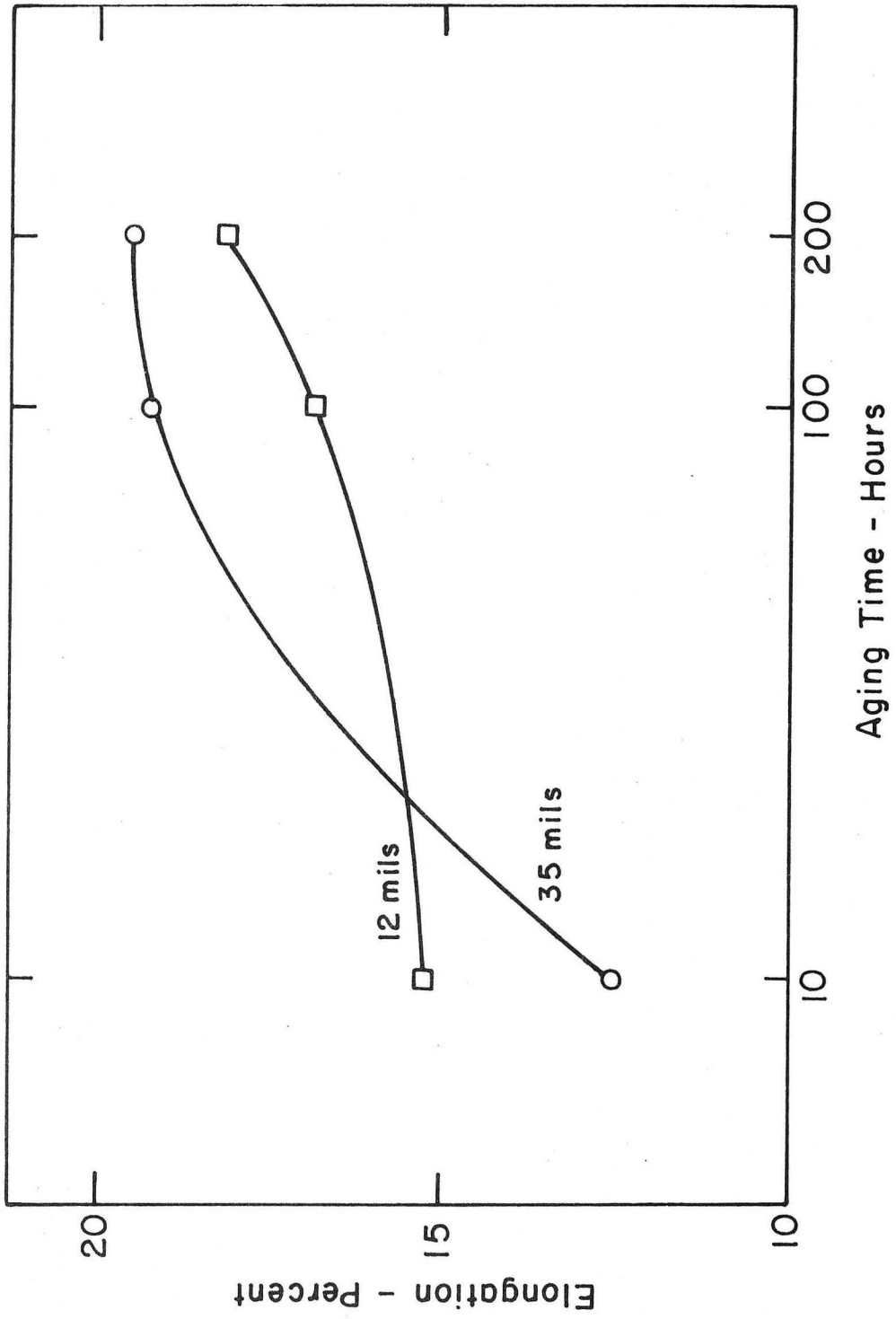
XBL 729-6900

Fig. 36
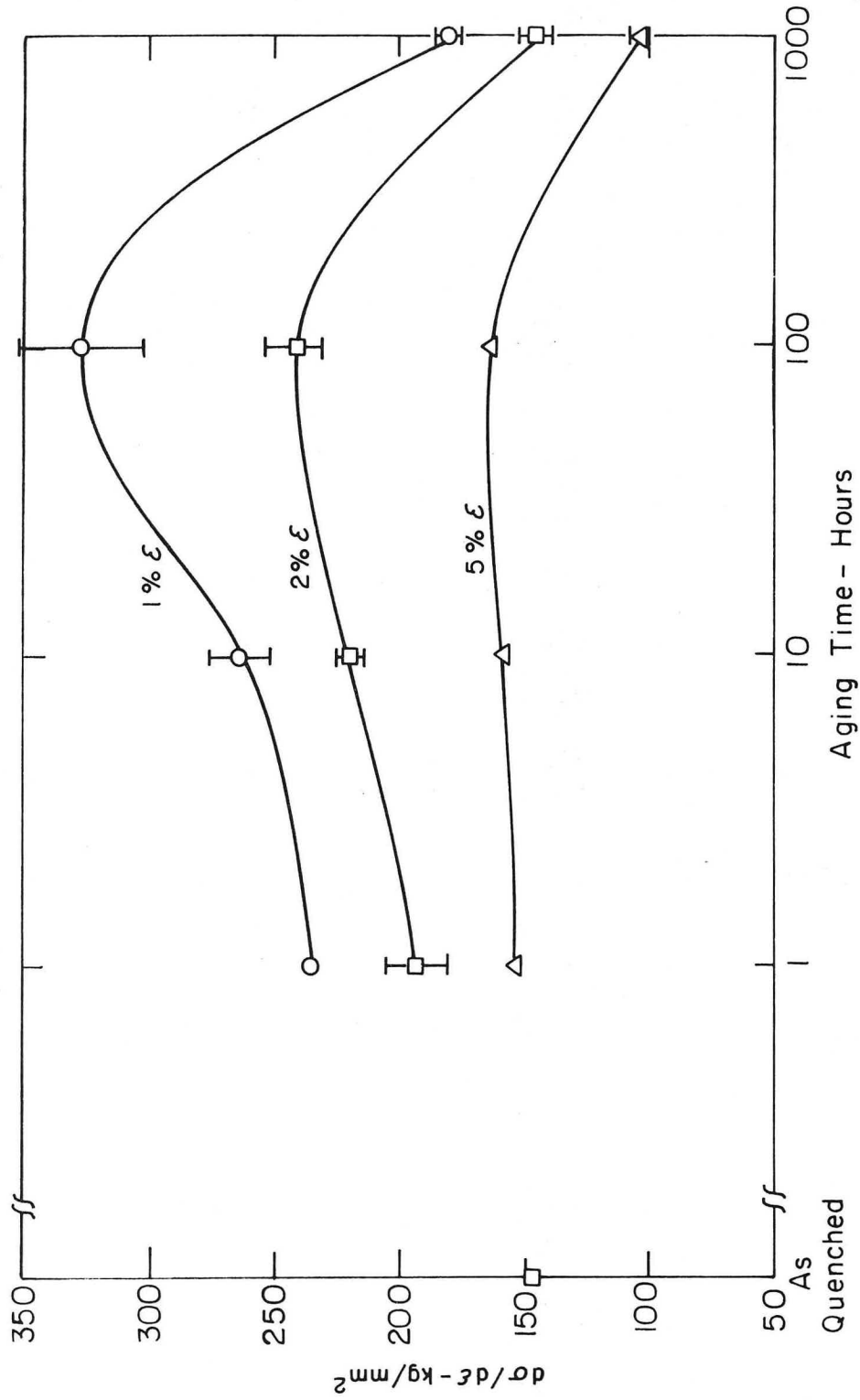
XBL 729 - 6896

Fig. 37
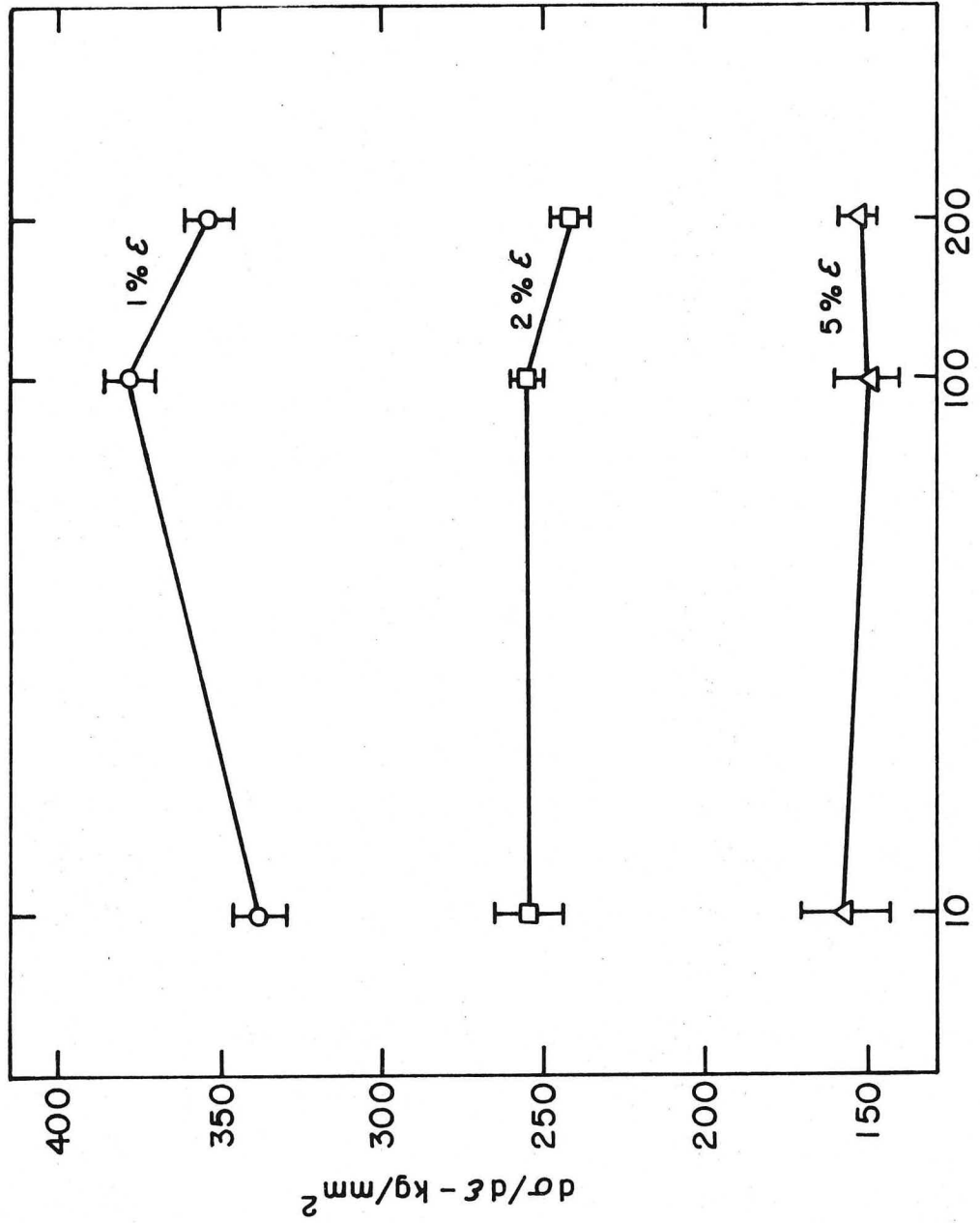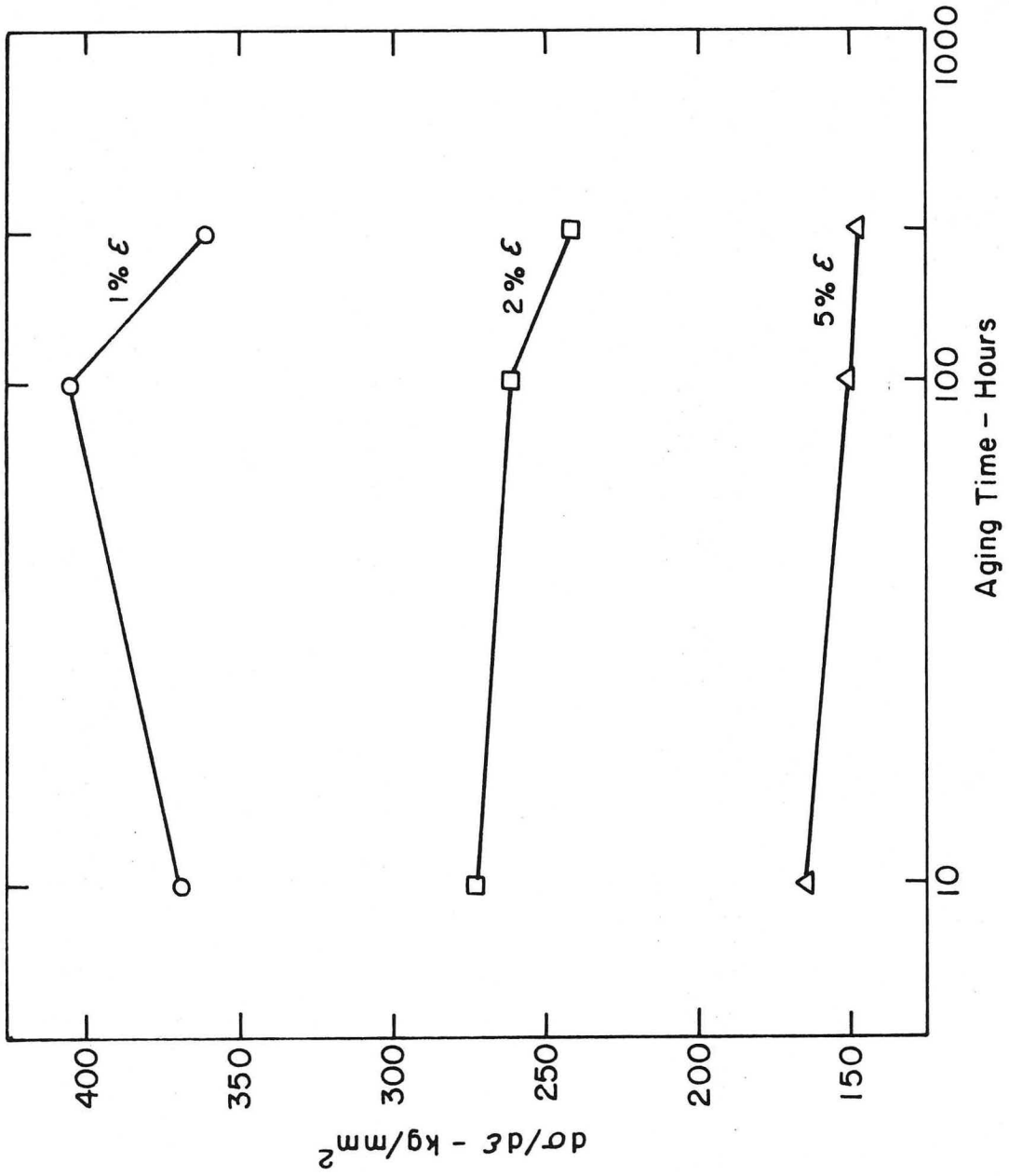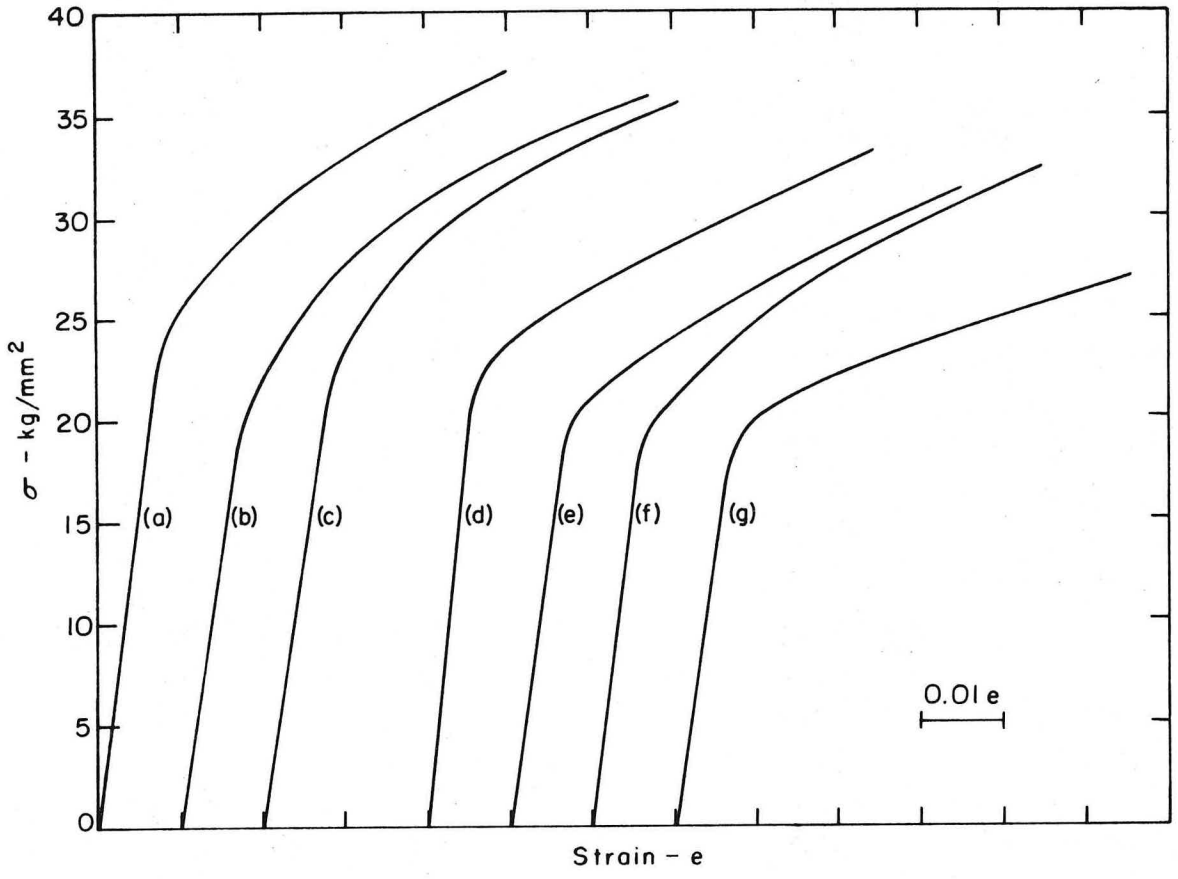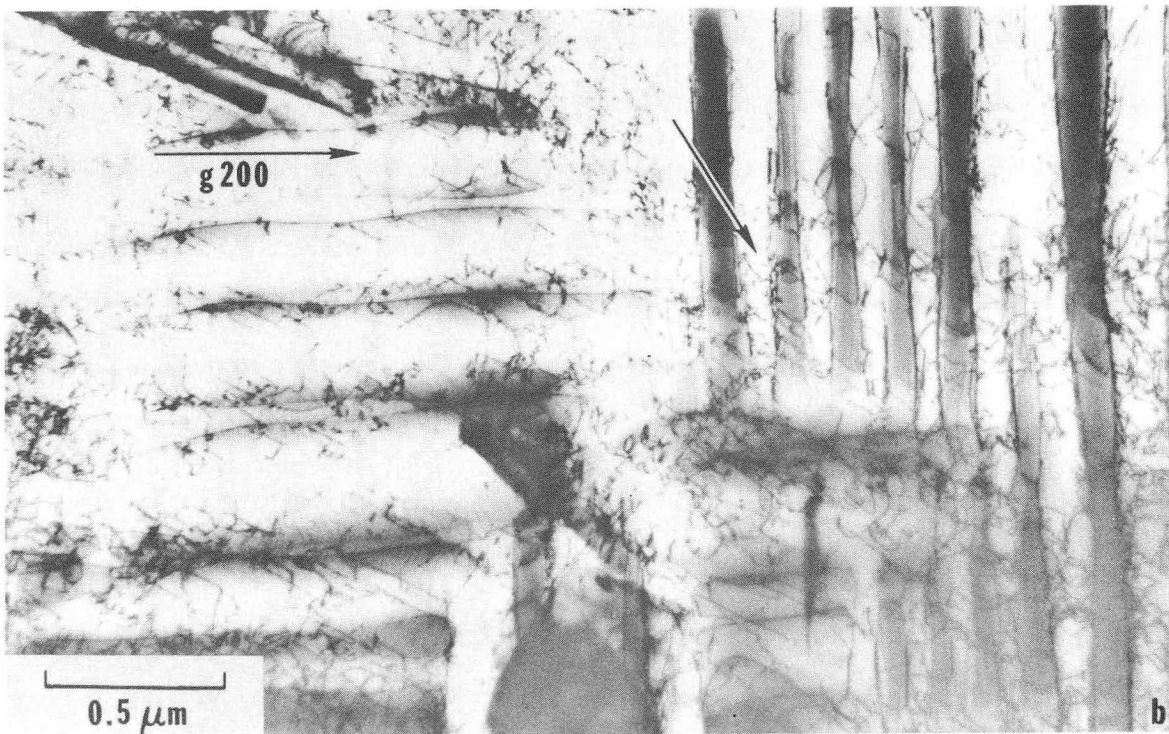
Fig. 38

XBL729-6897

Fig. 39

XBL729-6898

XBL 729-6894

Fig. 40

Fig. 41

XBB 729-4732

XBB 729-4727

Fig. 42

0.5 μm

⟨110⟩

XBB 729-4734

Fig. 43

0.3 μm

XBB 729-4733

Fig. 44

XBL 697-861

Fig. 45

σ_y (ksi)

K_i (ksi - $\sqrt{\text{in}}$)

$d^{-1/2}$ (mm$^{-1/2}$)

K_i and σ_y
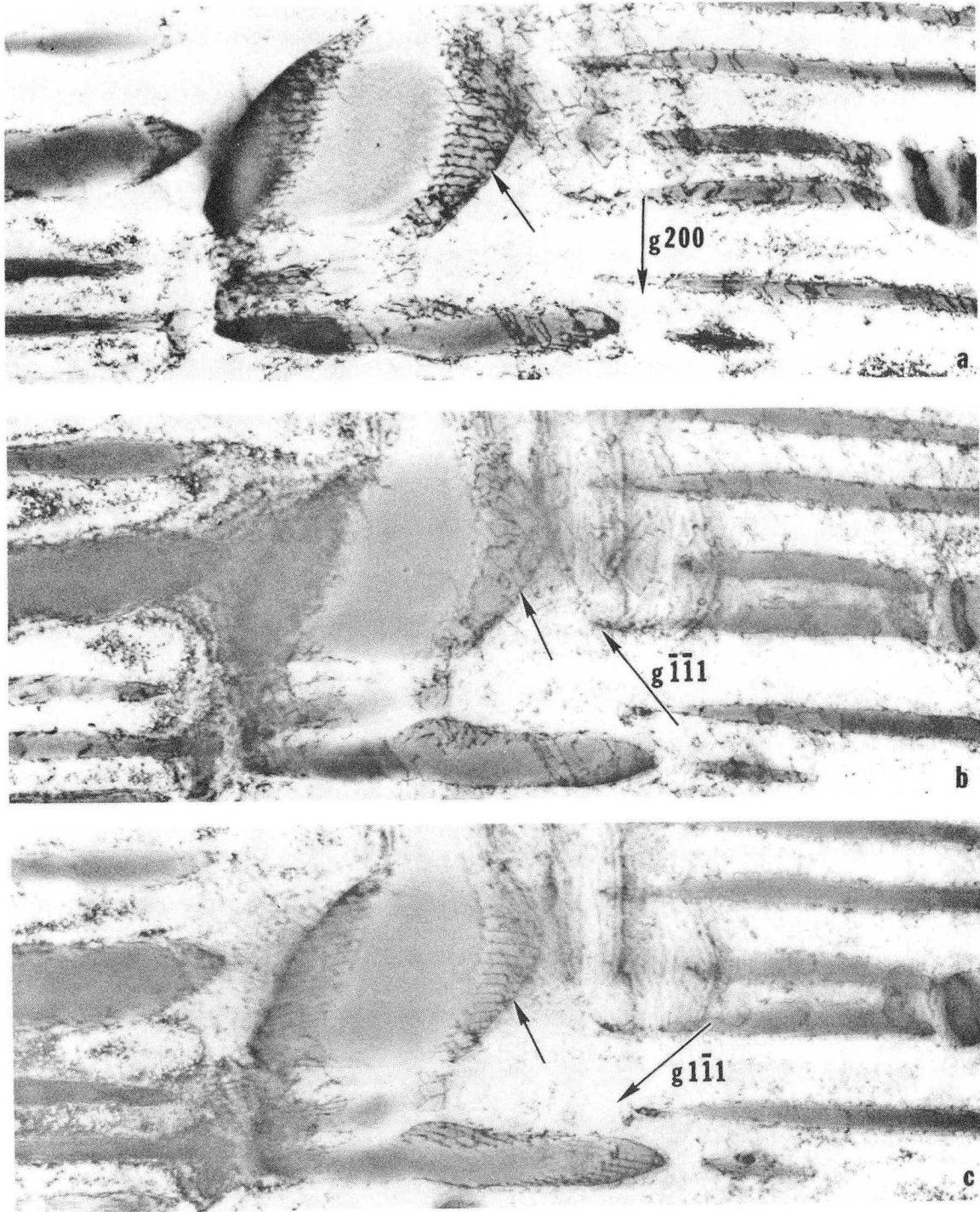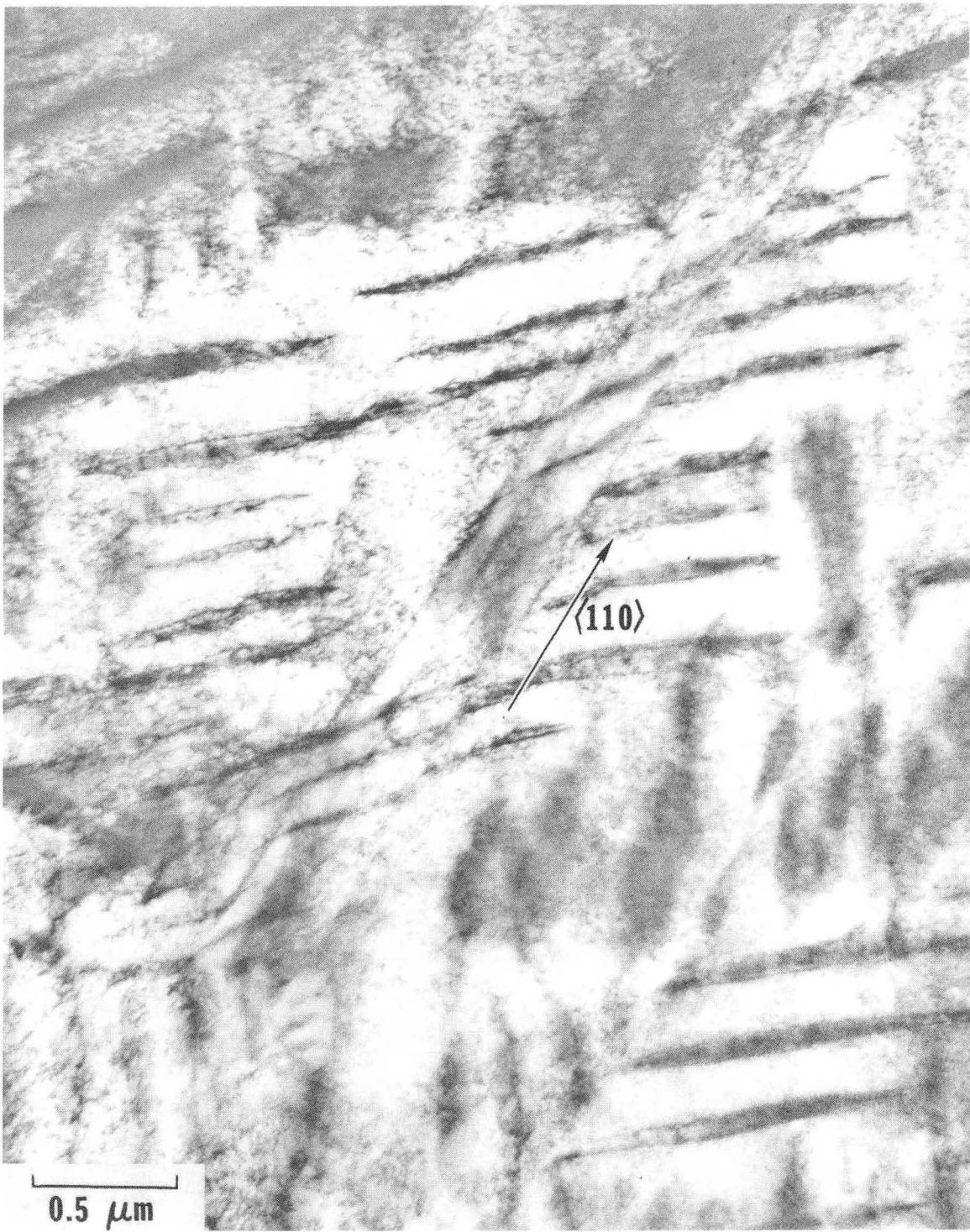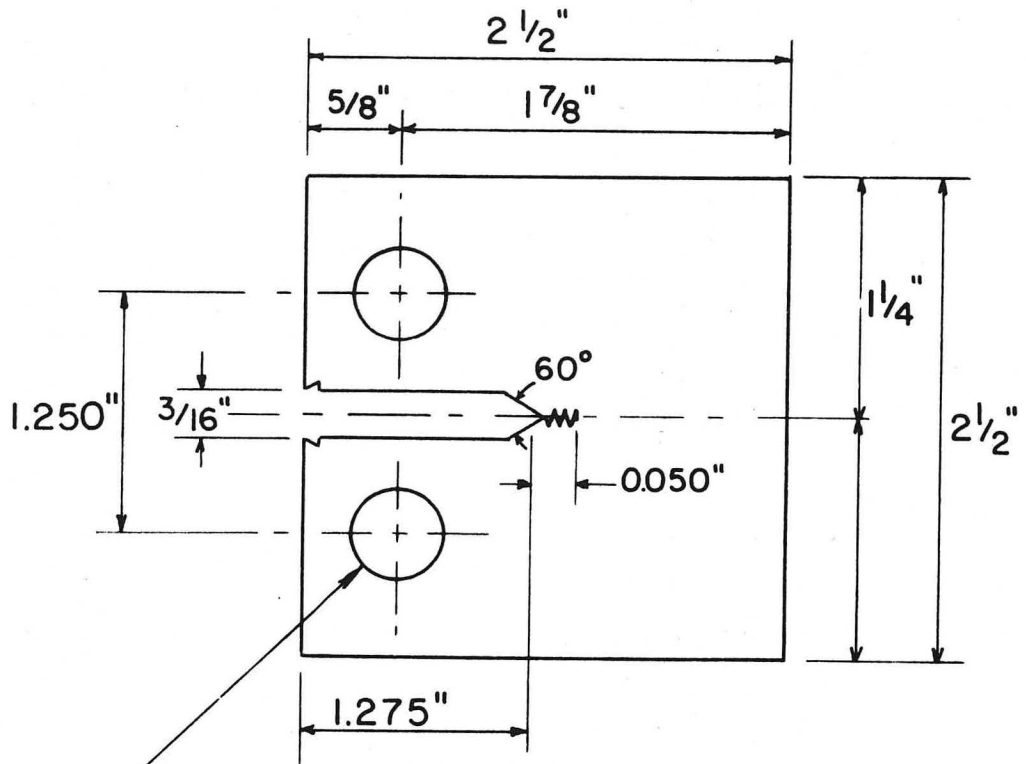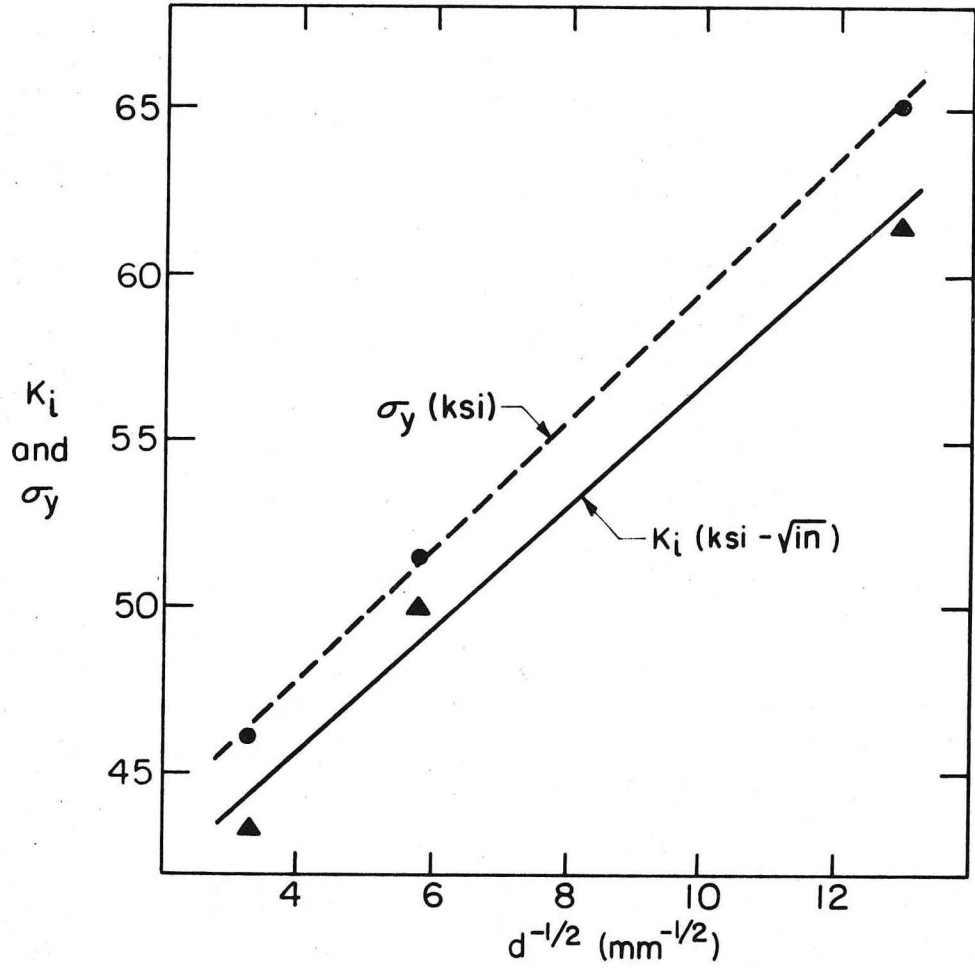
XBL 717-7014

Fig. 46

XBB 717-3240

Fig. 47

XBB 717-3239

Fig. 48

0.5 μ

a

0.5 μ

b
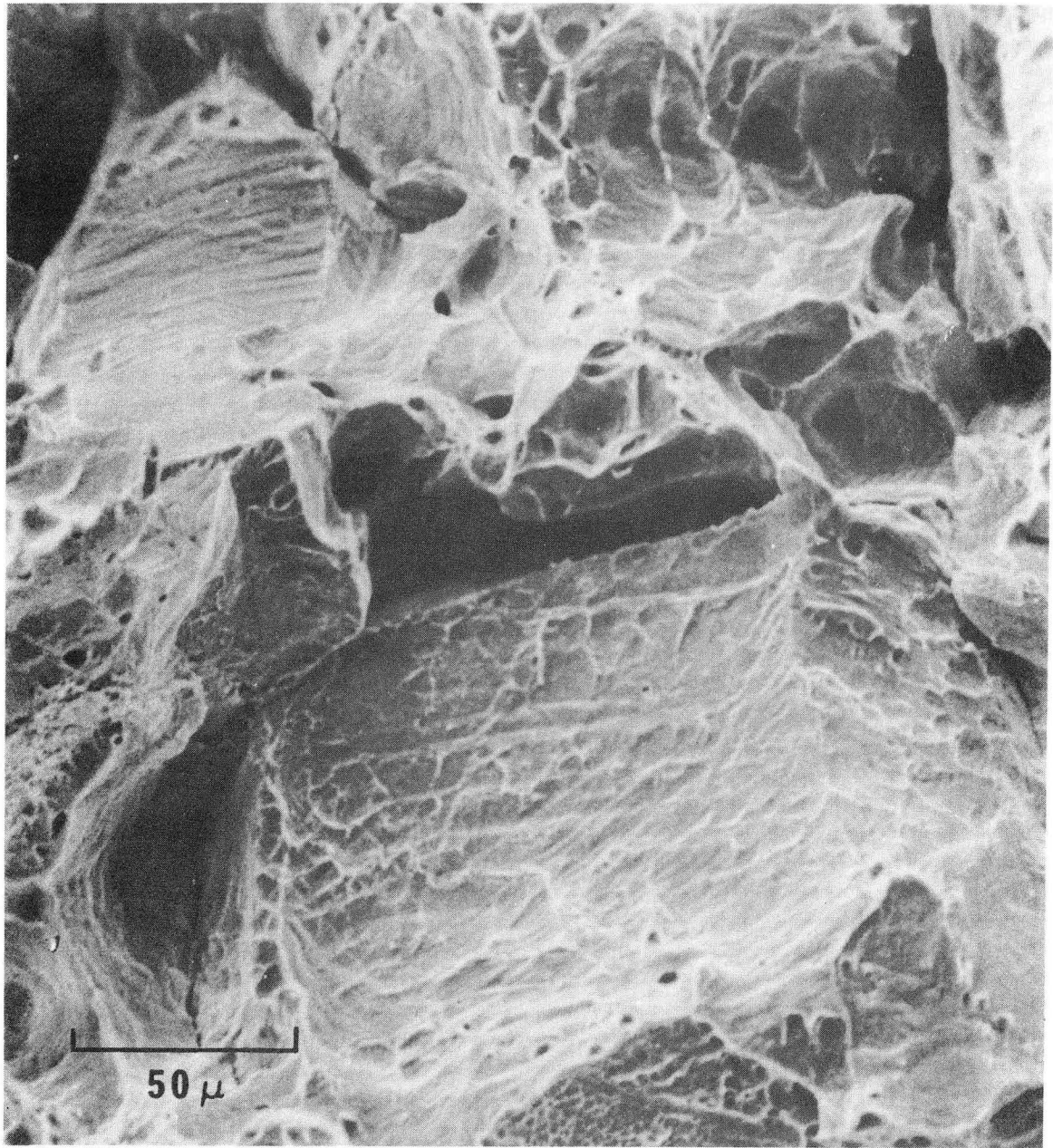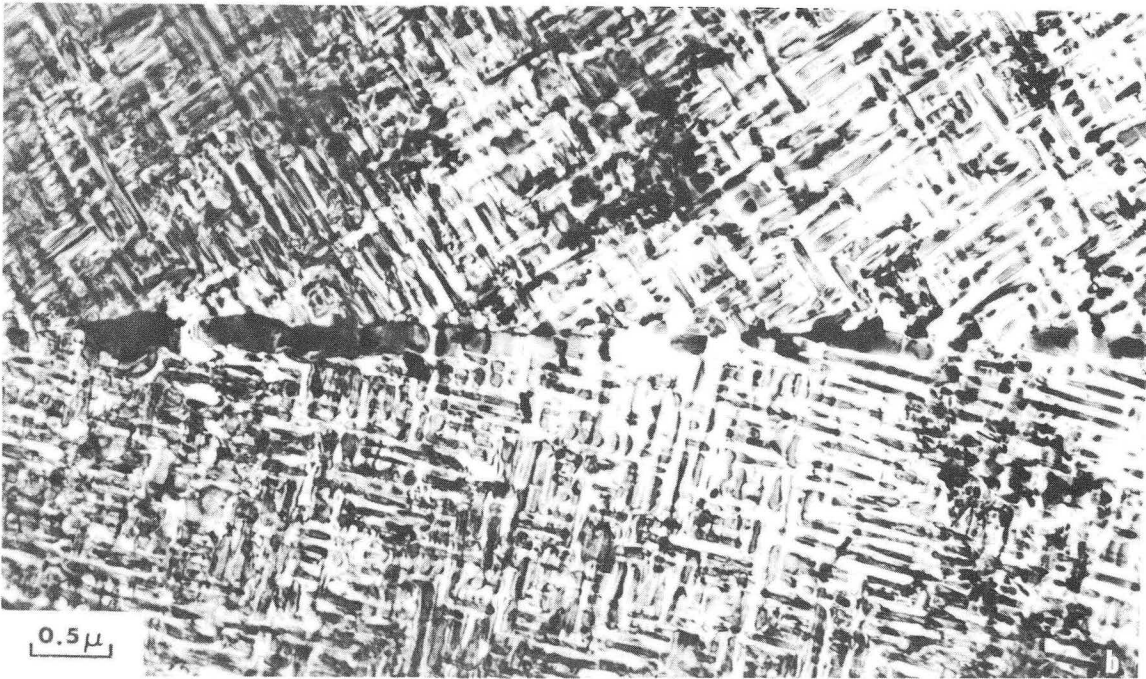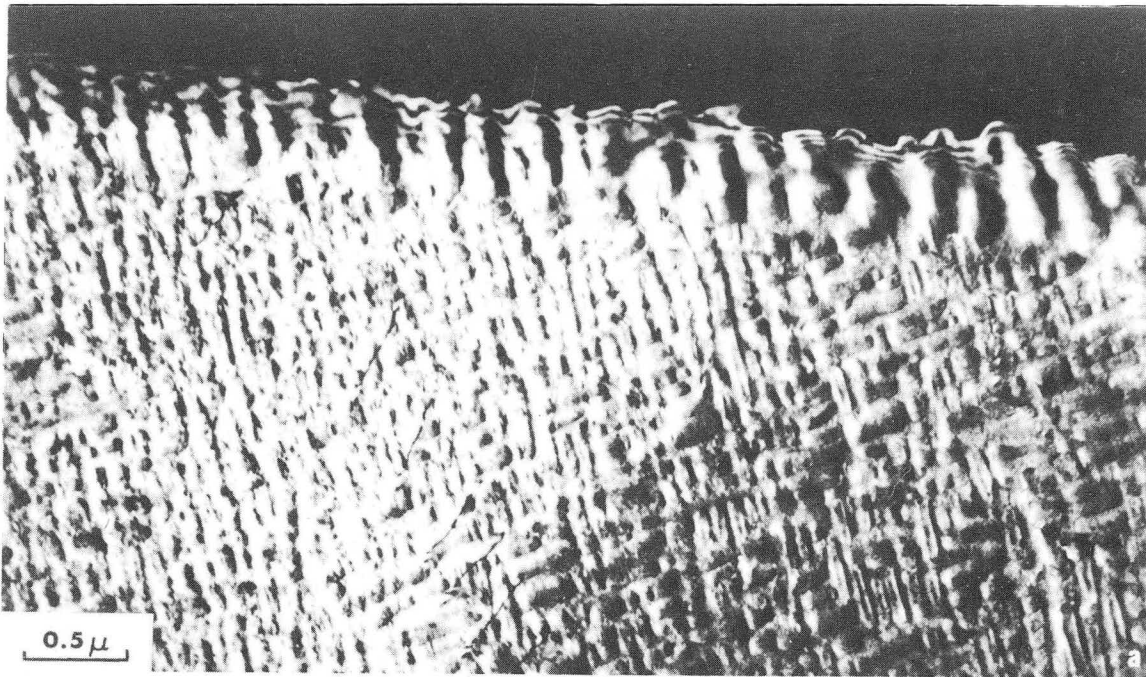
XBB 719-4167

Fig. 49
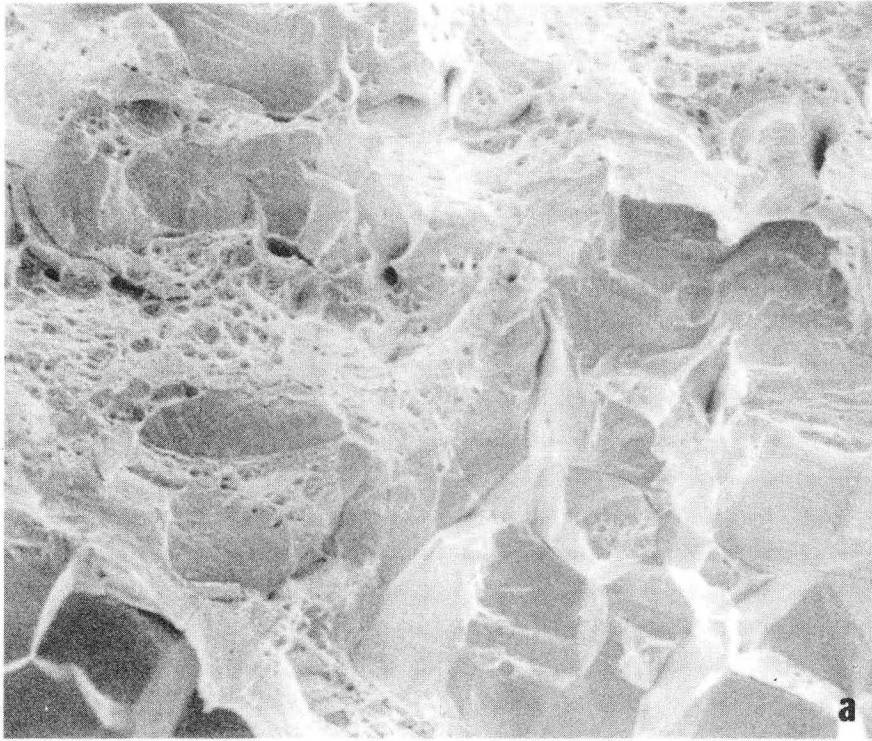
XBB 729-4617

Fig. 50
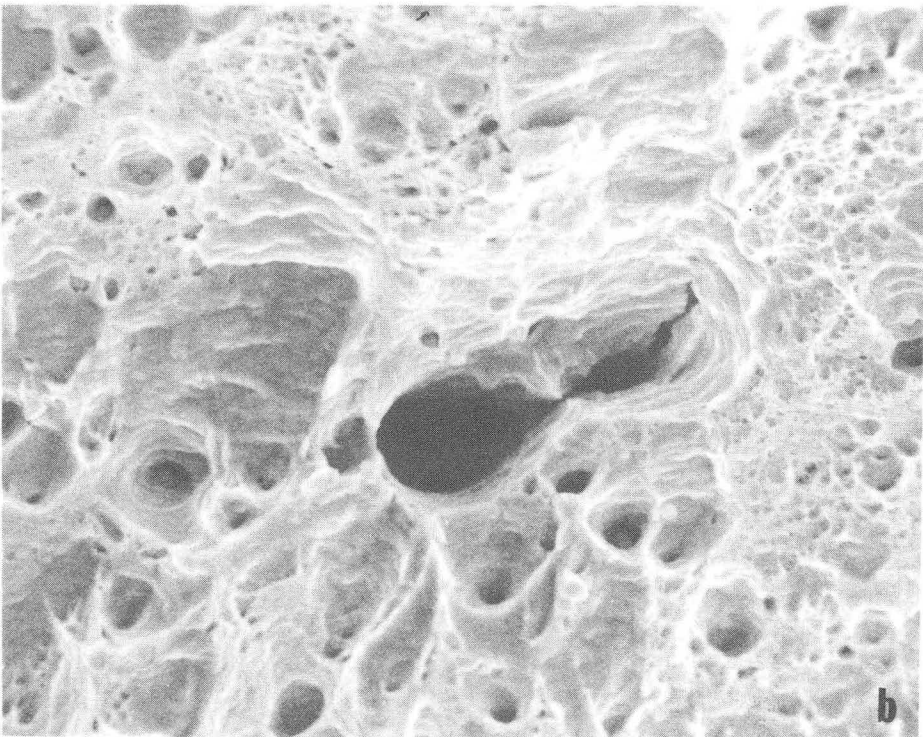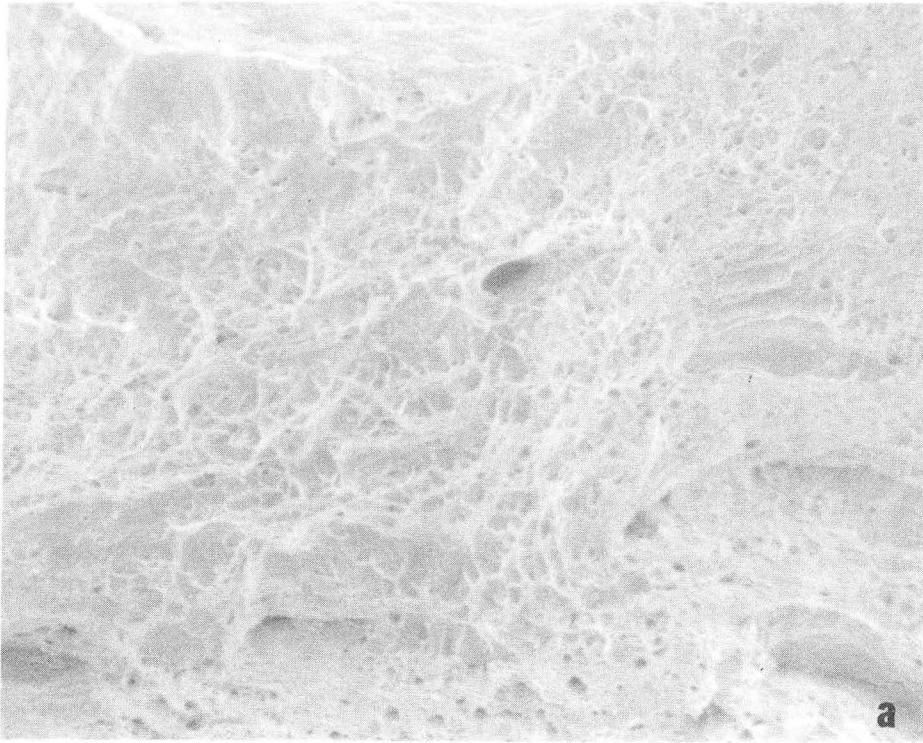
XBB 729-4618

Fig. 51
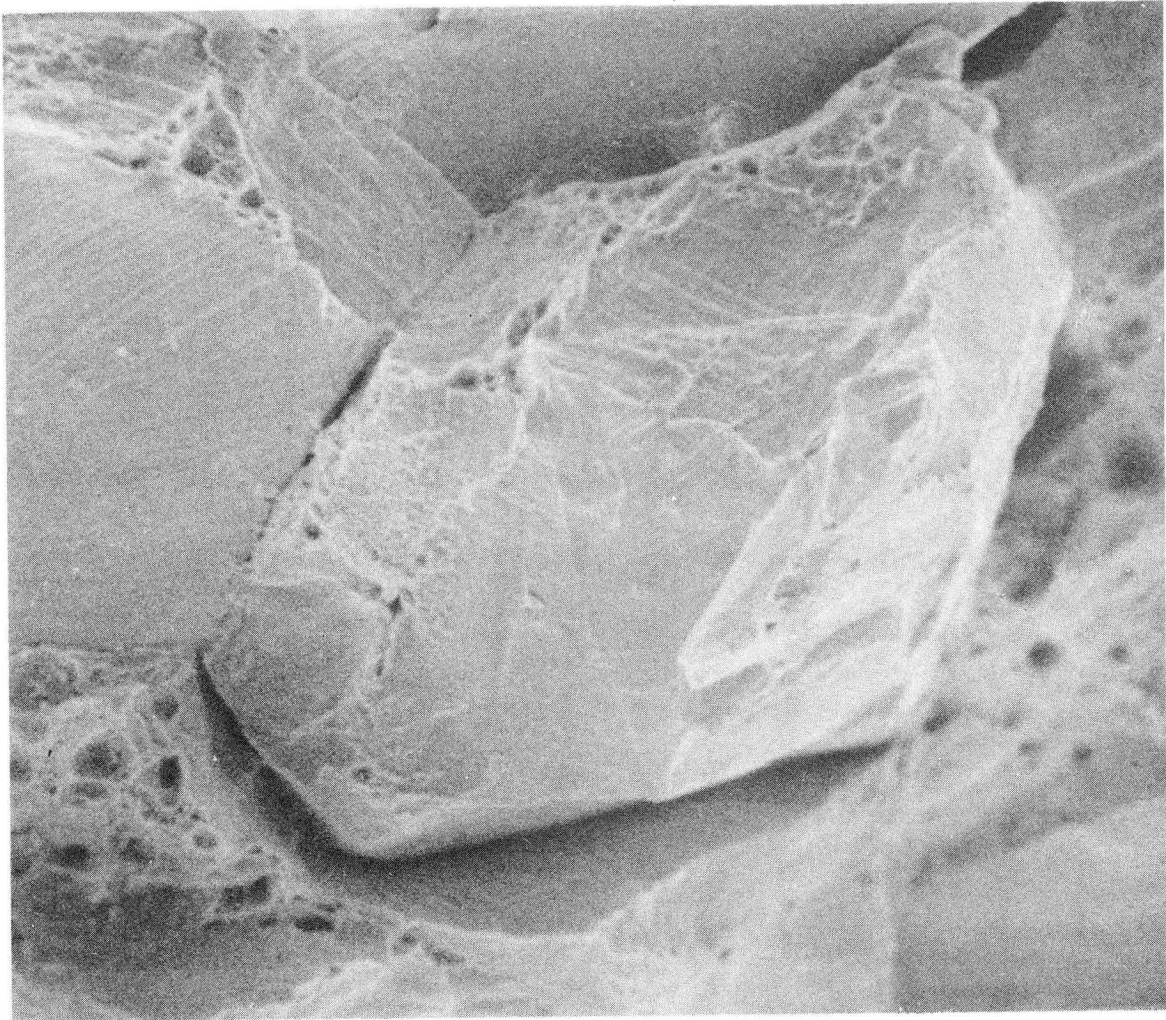
XBB 729-4616

Fig. 52

MICROPROBE ANALYSIS OF 64 CU - 27 NI - 9 FE ALLOY
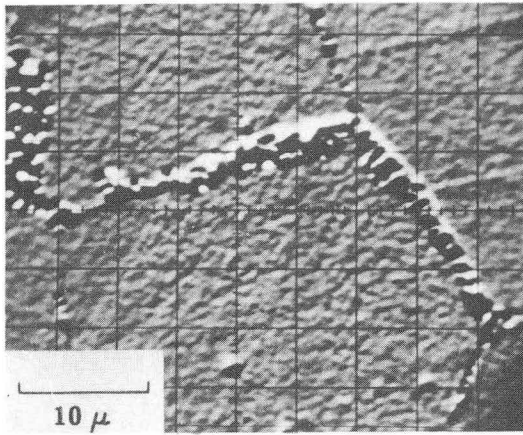
BACK SCATTERED ELECTRON IMAGE
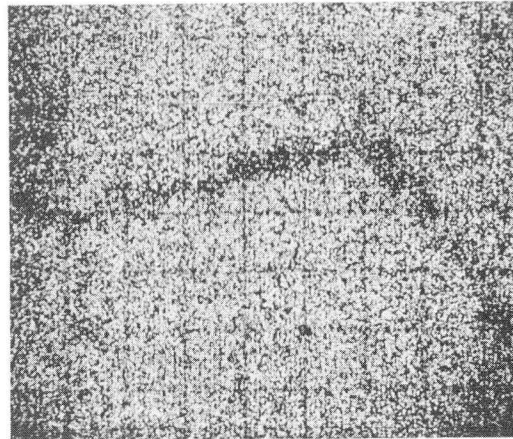
CU K_α RADIATION
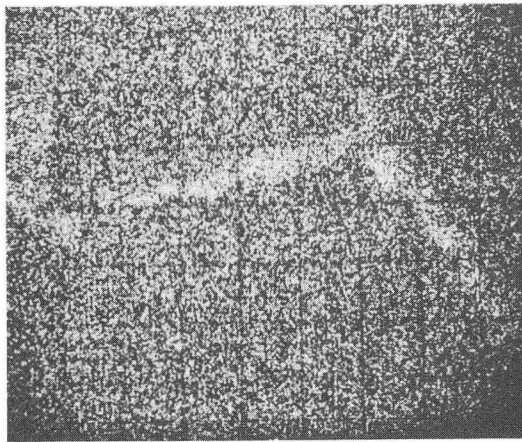
NI K_α RADIATION
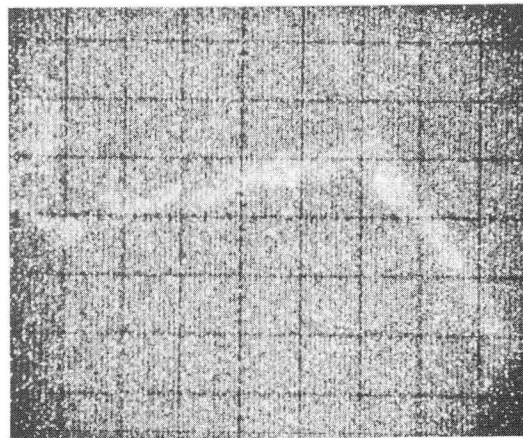
FE K_α RADIATION

XBB 707-3327

Fig. 53